ISBN 978-82-471-1832-0 (printed ver.)
ISBN 978-82-471-1833-7 (electronic ver.)
ISSN 1503-8181

Doctoral theses at NTNU, 2009:215

Halvor Dalaker

Solubility of Carbon and Nitrogen in the Silicon Rich Part of the Si–C–N–B-System

NTNU
Norwegian University of
Science and Technology

Halvor Dalaker

Doctoral Thesis

Doctoral theses at NTNU, 2009:215

NTNU

NTNU
Norwegian University of
Science and Technology
Thesis for the degree of
doctor philosophiae
Faculty of Natural Sciences and Technology
Department of Materials Science and Engineering

NTNU
Norwegian University of
Science and Technology

Halvor Dalaker

Solubility of Carbon and Nitrogen in the Silicon Rich Part of the Si–C–N–B-System

Thesis for the degree of doctor philosophiae

Trondheim, November 2009

Norwegian University of
Science and Technology
Faculty of Natural Sciences and Technology
Department of Materials Science and Engineering

NTNU
Norwegian University of
Science and Technology

NTNU
Norwegian University of Science and Technology

Thesis for the degree of doctor philosophiae

Faculty of Natural Sciences and Technology
Department of Materials Science and Engineering

ISBN 978-82-471-1832-0 (printed ver.)
ISBN 978-82-471-1833-7 (electronic ver.)
ISSN 1503-8181
IMT-Report 2009:117

Doctoral Theses at NTNU, 2009:215

Printed by Tapir Uttrykk

Dedicated to the four great artists of the 20th century:

Carl Barks
Shigeru Miyamoto
J.R.R. Tolkien
Frank Zappa

Preface

This thesis represents part of the requirements for the PhD degree. The work herein described has been carried out at the Norwegian University of Science and Technology, Department of Materials Science and Engineering, between August 2005 and August 2009.

The financial support has been provided through the Solar Grade Silicon Database subproject of the ThermoTech KMB project, the main contributors to which have been the Norwegian Research Council and the Norwegian Ferroalloy Producers Research association.

Trondheim, August 2009

Halvor Dalaker

Acknowledgements

My supervisor professor Merete Tangstad deserve my deepest thanks for her help and contributions to this thesis. I am incredibly grateful for the input she has provided, both in terms of general scientific advice and in the writing and assembly of this thesis. I wish to particularly thank her for taking time out of her holiday to read parts of this thesis and discuss them with me. This sacrifice of personal time is greatly appreciated.

I am also very grateful to professor emeritus Johan Kristian Tuset for sharing his experience and great knowledge of thermodynamics. The input he brought to the thesis and the discussions we had around it are much appreciated.

A special thanks also goes to Elkem for the analyses of samples, and for providing the feedstock for two castings. In particular I wish to thank Ragnar Tronstad at Elkem Research, who pulled the strings of the Elkem system on my behalf.

All employees of SINTEF and NTNU at Alfred Getz vei 2 deserve thanks for their contribution to a very good and inspiring working environment. Some people deserve to be explicitly mentioned however: Dr. Eivind Øvrelid, for inspiring discussions and for the help in performing a casting in the HelioSi laboratory. Dr. Kai Tang, for calculating thermodynamical data from the SINTEF database and for providing feedback on my early results. Dr. Harsharn Singh Tathgar,

for discussions, input and feedback in the early part of my thesis. Dr. Sean Gaal, for the design of the sealing mechanism used in the sample taking in the HelioSi laboratory. Marisa Di Sabatino for GDMS analyses. Jan Arve Baatnes, for his help with many issues regarding the experiments in the small tube furnace. Birgit Ryningen for the help of conducting a casting in the HelioSi laboratory. Torild Krogstad and Birgitte Sofie Karlsen for the etching of samples. Morten Peder Raanes for microprobe imaging.

All past and present members of the SiManTiAl group are thanked for their endless (in a good way) feedback on my presentation technique, and for the fun we have had outside of the office. Merete Tangstad deserves credit for putting this group together and for her (successful) efforts of making its members connect socially, not only professionally. Having friends at work helps making going to work every day that much more rewarding. On this note, I would also like to mention the members of the Materialteknikk football team (Of which I was a member until, in the words of Freddie Flintoff, my body told me *'it's time to stop'*); the participants of the pay-day beer drinking gatherings we have had; and of course all members of the mailing list gutta@material.ntnu.no.

Finally I wish to acknowledge the lifelong, unwavering support of my parents and sister, and of course give a big thank you to my beloved Linda. She has been patient, understanding and helpful throughout my four years as a PhD-student, and is a major contributor to my life being such an incredibly wonderful and fantastic experience.

Abstract

An experimental study of the thermodynamics of the silicon rich portion of the Si–C–N–B-system has been carried out. The main focus has been on the solubility data of the binary and ternary subsystems, while the distribution coefficient of boron has also been studied.

The experimental work has been performed using two different furnaces, a pilot scale directional solidification furnace, and a small scale resistance heated tube furnace. The main method of data gathering has been the direct extraction of liquid samples from the silicon melt using quartz tubes. In addition, samples have been cut from directionally solidified ingots.

The experimental work in the directional solidification furnace was concerned with the distribution coefficient of boron. Samples were cut from finished ingots and analysed using different methods at different laboratories. A critical assessment of the available data set made it possible to estimate the effective distribution coefficient of boron in silicon as $k_e = 0.70$.

In the resistance heated tube furnace, silicon melts were saturated with carbon or nitrogen at various temperatures. Graphite and Si_3N_4 crucibles served as the source of carbon and nitrogen, with a SiC-film forming on the crucible wall in the case of carbon. Experiments were performed in the pure Si–C and Si–N systems, as well as in the Si–C–B and Si–N–B systems in which elemental boron was added to the

silicon feedstock. In addition, some experiments were done in a Si_3N_4 crucible with a graphite slab in the silicon melt in order to investigate how the simultaneous saturation of carbon and nitrogen affected the solubility data.

It was found that both SiC and Si_3N_4 dissolved very rapidly as no time evolution of the carbon and nitrogen contents of the melts could be detected. This effect was so pronounced that it overshadowed any influence of the composition of the atmosphere: no difference was found in the nitrogen content of melts held under Ar and N_2 atmospheres.

The solubility of both carbon and nitrogen was determined as functions of temperature, yielding (in m.%):

$$C_C(T) = 482.84 \cdot \exp\left(-\frac{18897}{T}\right)$$
$$C_N(T) = 1.0484 \cdot 10^5 \exp\left(\frac{-28841}{T}\right)$$

At the melting point of silicon, 1414 °C, these equations predict carbon and nitrogen solubilities of 66 and 39 ppmm respectively. These equations were used to derive equations describing the dissolution energy of carbon and nitrogen (in J/mol):

$$\Delta G_{C(s)\rightleftharpoons\underline{C}(l)} = 4.6 \cdot 10^4 - 11.4T \log T + 23.2T$$
$$\Delta G_{(1/2)N_2(g)\rightleftharpoons\underline{N}(l)} = -1.59 \times 10^4 + 77T$$

When the melt was in contact with both SiC and Si_3N_4 and simultaneously saturated with both carbon and nitrogen, the solubility of both impurities increased. The carbon-nitrogen and nitrogen-carbon interaction coefficients were determined as

$$e_N^C = 110.83 - 207123/T$$
$$e_C^N = 95.01 - 177555/T$$

This allowed for the formulation of equations that showed carbon solubility as a function of temperature and nitrogen content as well as nitrogen solubility as a function of temperature and carbon content (in m.%):

$$C_C(T, C_N) = 7.37 \cdot \exp\left\{\frac{-11731}{T} - \ln(10) \cdot [(95.01 - 177555/T) \cdot C_N]\right\}$$
$$C_N(T, C_C) = 104840 \cdot \exp\left\{\frac{-28841}{T} - \ln(10) \cdot [(110.83 - 207123/T) \cdot C_C]\right\}$$

From these equations, linear approximations were created describing the carbon and nitrogen solubilities as functions of temperature during the simultaneous saturation of both elements (in m.%):

$$C_C^{N_{sat}} = 3.80 \cdot 10^{-5} T - 5.62 \cdot 10^{-2}$$
$$C_N^{C_{sat}} = 7.03 \cdot 10^{-5} T - 0.114$$

The addition of boron to the melt was found to influence the solubility of both carbon and nitrogen. The solubility of carbon was found to increase in a boron-enriched melt compared to a pure silicon melt. The boron-carbon interaction coefficient in silicon was calculated as:

$$e_C^B = -0.15 + 51.6/T$$

leading to the following expression for the solubility of carbon as a function of both temperature and boron level (in m.%):

$$C_C(T, C_B) = 482.84 \cdot \exp\left\{-\frac{18897}{T} - \ln(10) \cdot [(-0.15 + 51.6/T) \cdot C_B]\right\}$$

Two preliminary experiments were done on a boron-enriched melt held in a Si_3N_4 crucible. The nitrogen solubility was found to decrease

relative to the boron-free case, and the boron–nitrogen interaction coefficient was determined as

$$e_N^B = -28 + 52551/T$$

No detectable amounts of BN were found in a melt containing 1.5 m.%B, and it was concluded that the formation of BN is strongly supressed in nitrogen saturated liquid silicon.

Contents

List of Figures

List of Tables

List of symbols and abbreviations

γ	Activity coefficient.
ε_B^A	The A-B interaction coefficient, giving the effect of the content of A on the solubility of B with infinite dilution of B as the standard state.
at.%	Atomic percent.
μ_A	The chemical potential of component A
a_A	The activity of component A.
C_X	Concentration of element X; mass%.
e_B^A	The A-B interaction coefficient, giving the effect of the content of A on the solubility of B with 1 mass% of B as the standard state.
$\Delta G_{a\rightarrow b}$	Change in Gibbs energy for the reaction $a \rightarrow b$, in [J/mol].
k_0	Equilibrium distribution coefficient.
k_e	Effective distribution coefficient.
K	Equilibrium constant of a chemical reaction.
m.%	Mass percent (weight percent).
ppbm	Parts per billion mass.
ppma	Parts per million atoms.
ppmm	Parts per million mass.
M_A	Molecular weight of component A, in [grams/mol].
n_A	Number of moles of component A.
R	The gas constant
T	Temperature. In equations the unit is Kelvin, elsewhere °C is used.
X_A	Mole fraction of element A.
$\varnothing$	Internal/external diameter. Subscripts 'int' and 'ext' indicate 'internal' and 'external', respectively.

Chapter 1

Introduction

1.1 Motivation for photovoltaic power

In 1995, the Intergovernmental Panel on Climate Change (IPCC) released its Second Assessment Report. Among the main conclusions was that over the past century—coincident with an increase in greenhouse gases—our planet had undergone a significant warming, and that while much uncertainty still remained the balance of evidence suggested a human influence on the global climate [1]. By the time the IPCC released its 2007 Fourth Assessment Report, any remaining ambiguity was removed from their wording as they concluded: "From new estimates of the combined anthropogenic forcing due to greenhouse gases, aerosols and land surface changes, it is extremely likely[1] that human activities have exerted a substantial net warming influence on climate since 1750." [2].

While neither of these reports was released without controversy and

[1] In IPCC terminology, *extremely likely* indicates a probability of at least 95 %. This is the second strongest wording in IPCC terminology, with *virtually certain* used to indicate >99 % probability [2]. (Note by the present author.)

criticism, they clearly mirror the growing consensus in the scientific community that human greenhouse emissions are responsible for global warming.

Since a growing global population with increasingly improving standards of living is tied to an ever increasing global energy consumption, energy sources are required that are non-fossil, renewable and greenhouse emission-free or the Earth's climate will suffer great and irreparable harm.

It should also be noted that irrespective of the set of problems, issues and debates related to global warming, the need for non-fossil fuels would nonetheless arise sooner or later with the arrival of peak oil.

Among renewable energies, solar power represents one of the more established industries with a huge potential for continued growth. Wave energy is still in its infancy, and hydro power has limited possibilities for further expansion in addition to concerns about the impact on local ecologies. It also shares the dependence of wind power on favourable natural conditions. Solar power has the advantage that in many cases it can be produced close to the point of consumption, minimizing the installation of expensive cables and transport-related energy loss. Furthermore, many developing nations targeting considerable hikes in their standards of living have plentiful supplies of sunlight, making solar power the prime candidate to sustainably cover these nations' increasing energy demands.

If the global community is to make any sort of progress towards a substantial reduction of greenhouse gas emissions, there is need for expansions into the complete array of current and future renewables; wind, biomass, geothermal, hydro and others will all play an important role, but there are signs that the main stage will be occupied by solar. In a forecast by the German Advisory Council on Global Change illustrated graphically in figure 1.1, solar power was predicted to represent over 60% of global energy production by 2100. This esti-

mate will considerably overshoot its mark however, unless solar power becomes cost-competitive with traditional energy sources. Such competitiveness will most likely be achieved due to a combination of two factors: an increase in the cost of traditional fossil fuels and a decrease in the cost of solar-generated electricity. The price of fossil fuels can be expected to increase due to increased energy demands and a depletion of resources, as well as if individual governments or the global community as a whole imposes taxes and limitations on greenhouse emissions. An increase in the price of conventional energy without a decrease in the cost of alternative energy sources will, however, lead to an overall increase in energy costs that may have a stunting effect on the growth of the global economy. It is therefore important that great efforts are extended into cost reduction of solar power.

Today, the most widespread form of solar power is based on photovoltaic cells, most commonly made from silicon wafers. These cells have an efficiency of approximately 13-18 % and are rather expensive. Electricity drawn from silicon solar cells can be made more affordable through a combination of increased cell efficiency and reduced production costs. While there are gains to be made in both of these areas through technological advances within contacts, anti-reflective coating, up and down conversion etc.; the silicon wafer itself represents a huge potential for improvement. Approximately 50 % of the cost of a silicon based solar cell can be traced to the cost of the silicon wafer, and the potential efficiency of the solar cell is limited by such material qualities as impurity and inclusion content, crystal defects etc.

The production process of silicon wafers is therefore one of many important areas for which there is a need for a sustained research effort in the coming decades. This includes everything from the production and purification of feedstock up to the sawing of silicon ingots into wafers. This thesis aspires to represent one small grain of sand in the wall of knowledge upon which a future based on sustainable energy can be built.

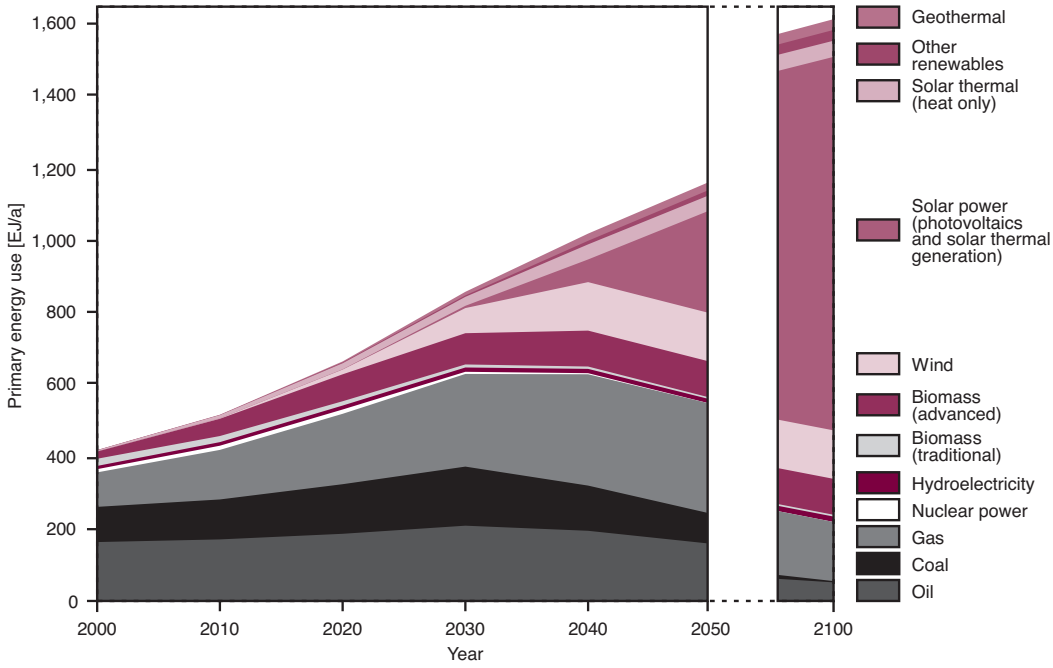

Figure 1.1: Predicted trends in energy market shares. From the German Advisory Council on Global Change [3].

In this opening section, I have aimed to motivate the need for research into photovoltaic energy in general and silicon solar cells in particular. In the remaining sections of the introduction I will give some brief background information on the field of silicon solar cells, and finally, present a motivation for thermodynamic studies of the silicon rich Si–B–C–N-system.

1.2 Silicon for solar cells

Photovoltaics represent the portion of solar energy devices that generate energy by the conversion of light— that is, photons— to electric potential energy, i.e. Volts. This technology is based on the photovoltaic effect, first observed by Alexandre Edmond Becquerel in 1839 and explained by the great Albert Einstein in 1905. A solar cell is a device that performs this light-electricity conversion. This section will try to give a brief overview of the workings of a solar cell. The information given in this section is standard material in most textbooks on semiconductor physics (see for example Streetman and Banerjee [4]; Quirk and Serda [5]; or Hummel [6]).

Semiconductors, band gaps and doping The starting material of a solar cell is a semiconductor such as silicon, gallium-arsenide, germanium etc. A semiconductor can colloquially be said to be an intermediate material state between a conductor and an insulator. For a slightly more rigorous definition, it is necessary to consider the electronic properties of materials.

The outer electrons in an atom can belong to one of two energy-bands: the valence band or the conductance band. Electrons in the valence band are tightly bound to their parent atom, while electrons in the conductance band are free to move away from the atom under the application of an external electric field, thus contributing to the flow of an electric current.

In metals there is an energetic overlap between the valence and conductance bands, meaning that valence electrons can easily redistribute to the conductance band and contribute to the flow of electric current, as evidenced by the fact that all metals are excellent conductors. On the other hand, in insulators and semiconductors there is an energy gap between the top of the valence band and the bottom of the conductance band. This energy gap is termed the band gap

and is an important material property of semiconductors. For insulators, the band gap is very large (e.g. 4.5 eV for diamond), meaning that (for all intents and purposes) no electrons will occupy the conductance band at any given time. For semiconductors, the band gap is considerably smaller (e.g. 1.1 eV for silicon), meaning that even at room temperature a significant number of electrons will possess enough thermal energy to bridge the band gap and potentially conduct electricity. These excited electrons will also leave behind holes in the valence band into which a neighbouring electron can move. This will in turn create a new hole, and new electrons can continually move into the newly created hole near them, creating an effect that can be described as the movement of a hole through the valence band. Since it is in fact the movement of a series of electrons, the movement of this hole also contributes to the conduction of current. Its contribution is equivalent to, and best described as, the hole being a positively charged particle travelling in the direction of the current flow.

The semiconducting nature of the semiconductors is not in itself their most valuable property. Rather, it is the modifiability of their electric properties that have led to their application in a wide variety of fields, most famously in the computer industry, but also in other electronics, sensor appliances and of course solar cells.

The most common way in which a semiconductor is modified is through a process known as doping. This involves implanting the semiconductor with atoms of a different element, referred to as dopants, in concentrations in the range of $\sim 1 \cdot 10^{16}$ atoms/cm^{-3}. Dopants are chosen to increase the number of conducting electrons or holes in the semiconductor. For silicon, this can be done by choosing elements from groups 13 or 15 (III or V in the old notation). Since silicon has four valence electrons, doping with an element from group 13, with three valence electrons, will reduce the number of electrons in the valence band of silicon, thus increasing the number of holes. The dopant element is then an acceptor. Similarly, doping with elements of group 15

will increase the number of conducting electrons, with the doping element being a donor. A semiconductor that is acceptor-doped is called p-type, since the positive holes are the majority charge carriers. In a p-type semiconductor, electrons are minority charge carriers. Completely analogous, a donor-doped semiconductor is called n-type, and the majority charge carriers are electrons. While both electrons and holes contribute to the current in both types of semiconductors, there is a typical difference in concentration of several orders of magnitude between the minority and majority carriers. A semiconductor that is neither p-doped nor n-doped is called an intrinsic semiconductor. In silicon, the most common dopant elements are boron for p-type and phosphorous for n-type.

The pn-junction and the solar cell The basis of a solar cell is a so called pn-junction: an interface between a p-type and an n-type semiconductor. Because of the great concentration gradients of both electrons and holes across such a junction, there will be a diffusion of electrons into the p-type region, with holes diffusing in the opposite directions. This diffusion of electrons will lead to the n- and p-type regions becoming positively and negatively charged, respectively, and an electric field will be established across the junction that prevents further diffusion. This electric field suppresses the migration of majority charge carriers across the pn-junction, but it facilitates minority charge carrier flow. This is the mechanism utilized in solar cells.

A silicon solar cell is typically made from a wafer, approximately 200 μm in thickness, of boron doped, p-type silicon. A pn-junction is then created by heavy in-diffusion of phosphorous from the top of the wafer, creating an excess of phosphorous in the uppermost region of the wafer which will hence be n-type.

As sunlight is incident on the wafer, a photon may excite an electron-hole pair in the p-type region. If the electron migrates into

the vicinity of the pn-junction, it will be swept across it by the electric field and into the n-region. Here it can be collected by the front contacts and led through an electric circuit to the back-contacts and into the p-region of the solar cell. Meanwhile, the hole will face an energy barrier across the pn-junction and remain in the p-region, and can recombine with an electron as it emerges from the back contact. Thus, an electric current is established, and energy can be extracted from the cell by applying an external load to the circuit. Silicon solar cells can also be made from n-type (typically phosphorous doped) silicon and then creating a pn-junction through boron-implantation, but the roles of electrons and holes will be reversed.

Recombination, minority carrier lifetime and impurities Once a minority charge carrier is excited in a solar cell, there is a chance that it will recombine with a majority charge carrier in an electron-hole annihilation process. The minority carrier lifetime of a semiconductor material is the average time a minority charge carrier in the material remains excited before it is annihilated. A proportional quantity is the minority carrier diffusion length, which is the average length a minority carrier migrates before it recombines. For a solar cell to produce electricity, it is necessary that the minority carriers diffuse to the pn-junction. Thus a large minority carrier lifetime and diffusion length will mean that a larger portion of excited electrons reach the pn-junction and are able to contribute to the production of energy. In other words: A material with high minority carrier lifetime and long minority carrier diffusion length will produce more efficient solar cells.

The electron-hole recombination can be facilitated through a variety of means. For example, electrically active impurities in a solar cell can introduce energy levels inside the band gap. These energy levels are termed traps and can seriously deteriorate the minority carrier lifetime, and thus also the performance of the solar cell. This is the

reason why solar cell silicon needs to have a very high purity. Another factor that limits minority carrier lifetime is structural defects, such as grain boundaries and dislocations. For this reason wafers cut from silicon single crystals produce more efficient solar cells than wafers cut from multicrystalline ingots.

In order to create silicon solar cells with the highest possible efficiency then, the wafer should be free from structural defects and electrically active impurities. Since carbon and nitrogen form precipitates detrimental to the crystal structure of silicon, and boron is electrically active, a prerequisite for efficient solar cells is the careful control of all of these elements throughout the cell production process.

1.3 Carbon, nitrogen and boron in silicon

This thesis has been undertaken as part of a Solar Grade Silicon Database subproject within the ThermoTech project. The goal of the subproject was 'to create the world's best thermodynamical database on solar grade silicon and its important trace elements'. The scope of the current work was to generate experimental data to be used in the construction of the database.

The 'important trace elements' of solar grade silicon of course encompasses a large number of different impurities, but the current work could—for obvious reasons—deal with only a fraction of these and carbon, nitrogen and boron were chosen. These three elements are virtually always present in solar grade silicon.

Carbon can be present in silicon from the production of metallurgical grade silicon, in which quartz undergoes carbothermic reduction. In addition, several furnaces employed in the solidification of multicrystalline silicon ingots contain many interior graphite parts. Silicon carbide particles and filaments are frequently observed in finished ingots, implying that carbon is present in quantities above the solid solubility limit.

Exactly what this solubility limit—and the corresponding limit in the liquid phase—is, are not well-established figures in the literature, but remains important quantities in the attempted understanding of the behaviour of carbon during the solidification of silicon.

When it comes to nitrogen in solar grade silicon, the most common contamination source is the crucible coating. Crucibles used for the solidification of multicrystalline silicon ingots are typically coated with silicon nitride in order to avoid sticking. Although nitrogen is a very common impurity it has been even less studied than carbon, and there is an even greater scatter in the available experimental data. Neither nitrogen nor carbon are electrically active in silicon, but they form precipitates that can be problematic. These SiC and Si_3N_4 particles

can function as nucleation sites for dislocations [7], and may also cause problems in the wire sawing of wafers [8].

SiC filaments can also penetrate the pn-junction of a solar cell and cause shunting. Rao et al. [9] first attributed this to the metallic decorations of the particles, but Al Rifai et al. [10] proved that the shunts were created by the electrically conducting SiC. There has been speculation that Si_3N_4 particles can also cause shunting, but this notion was dismissed by Al Rifai et al.

It is also of interest to investigate the interactions between nitrogen and carbon, as they are commonly observed together in solar grade silicon. This is also true of their precipitates formed with silicon, with Si_3N_4 often functioning as a nucleation site for SiC [11, 7, 12, 13, 14].

The difficulties connected with carbon and nitrogen in ingot and cell production mean that these elements should be controlled in feedstock production as well. The removal of SiC and Si_3N_4 particles is a key issue in new production routes for solar grade silicon.

Boron is different from the other two elements not only in that it is electrically active, but it is also a dopant element. Thus it is frequently present in silicon because it has been purposely added to the system. However, in alternative production routes for high purity silicon, boron is a difficult impurity to remove because of its high distribution coefficient. The knowledge of how boron interacts with common impurities is therefore of relevance not only from the perspective of solar cell manufacturing of boron-doped material, but also from the perspective of boron removal during the purification of silicon.

During the production of both multi- and monocrystalline ingots, silicon is kept in a liquid state at temperatures just above the melting point of silicon for long periods of time, in direct contact with the freshly solidified silicon. Thermodynamical data such as solubility levels and distribution coefficients are vital to the understanding of how impurities are incorporated into the liquid at high temperatures and how they behave during solidification with respect to precipitation

and segregation between the liquid and solid phases.

The main goal of this doctoral work has been to expand the existing thermodynamical data available in the silicon rich Si–C–B–N-system in the temperature range from the melting point of silicon and ∼100 °C upwards. The focus has been set on solubility data, distribution and interaction coefficients. The lower-temperature regions of the same system are also very interesting, but have not been investigated in this project due to the limited timeframe. This would represent a natural continuation of the current work in future projects.

This thesis will describe and discuss the experimental results obtained during a four-year period of doctoral work. First, the current status of knowledge on the Si–B–C–N-system will be established in the next chapter entitled 'Theoretical background'. This chapter will also define some key thermodynamical concepts and give an overview of directional solidification and segregation.

The experimental work in this thesis has been performed using two different apparatus, a small tube furnace and a pilot scale directional solidification furnace. The tube furnace has been used for the determination of solubility data, while the ability to perform directional solidification in the pilot scale furnace has allowed for the determination of distribution coefficients. The thesis will adopt a two-part structure over the next two chapters, and deal with one furnace at the time. Thus, Chapter 3 will first give an overview of the experimental set-up and procedures employed in the experiments on directional solidification before moving on to the small tube furnace. Likewise, in Chapter 4 the results of the directional solidification furnace will be given first. The second part of Chapter 4 will present the results from the small tube furnace, categorised by the elements present in the system. The results presented here will be solubility data and other results directly derived from the experimental observations.

Moving away from the categorisation and segmentation, Chapter 5 discusses the results from the different experiments and furnaces as

different parts of a whole. Here, the various results are tied together and the findings are compared with existing literature. Finally, the main conclusions of the thesis are summed up in Chapter 6.

Chapter 2

Theoretical background

2.1 The Si–C–N–B-system and its subsystems

The following section will give an overview of the available literature on the different subsystems of the Si–C–N–B-system. Where possible, the focus has been on the silicon rich parts of the systems with carbon, boron and nitrogen being trace elements. However, for some systems this data is severely limited, so this review also includes information from other areas of the included subsystems.

The binary phase diagrams included in this section are modelled by Tang as part of his work on the SINTEF database for solar grade silicon and its most important trace elements [15, 16, 17].

2.1.1 The Si–C binary system and carbon in silicon

The Si–C system consists of three solid phases: Silicon with dilute carbon, carbon with dilute silicon and silicon carbide. Silicon car-

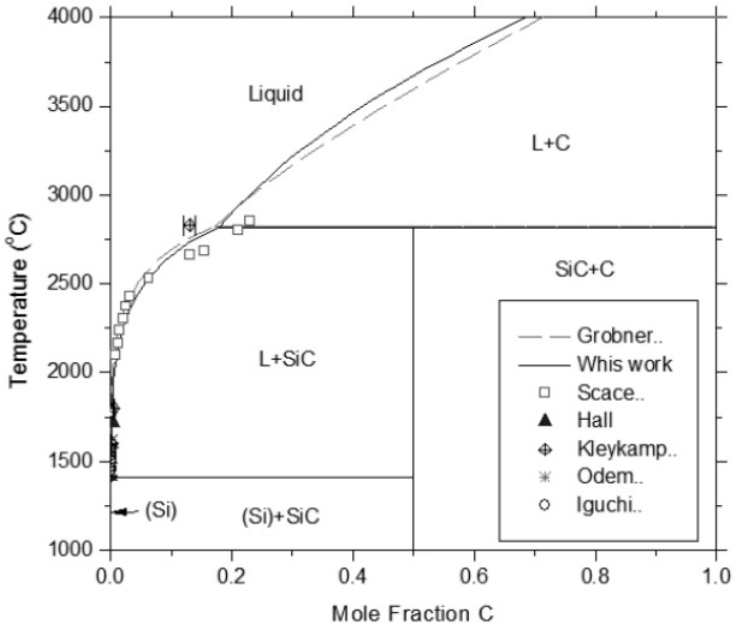

Figure 2.1: Si-C phase diagram [15]

bide exists in two modifications: hexagonal α-SiC and cubic β-SiC. Of these, β-SiC is the stable polymorph at low temperatures which will transform into α-SiC at temperatures above $\sim$2000 °C. The two modifications have very small energetical differences, and the β/α-transformation temperature is not accurately established in the literature. Since its discovery in the late nineteenth century, silicon carbide has seen a wealth of applications in a vast amount of different fields. It is a remarkable compound, its wide range of properties including semiconductivity, good thermal conductance and extreme hardness. This versatility has also seen it applied in the solar cell industry, par-

ticularly as an abrasive used for the wire cutting of silicon wafers.

Carbon as a trace element in silicon Carbon dissolves substitutionally in silicon and is not electrically active [18]. At supersaturated concentrations silicon carbide will form, and it is chiefly in this form that carbon is a concern for cell and wafer producers. SiC is observed in two forms in silicon ingots: as small sphere-like particles or as threaded filaments appearing to have grown in the direction of solidification [10].

One of the earliest and most cited works on the Si-C system was performed by Scace and Slack [19] in 1959. The principal method of their experiments was to saturate silicon with carbon at high temperatures and then quench the sample. The SiC residue of the sample was isolated and weighed, and the solubility computed from the ratio of the SiC mass to the total mass of the sample. They performed experiments between 1578 °C and 2830 °C. In addition, they used a result by Dash who reported a solubility of $3.0\pm0.3\cdot10^{18}$A/cm^3($\approx$ 26 ppmm) at or near the melting point of silicon. From this they obtained an equation for the solubility as a function of temperature, given as the mole fraction of carbon.

$$X_C = exp\left(\frac{\Delta H}{R}\left[\frac{1}{T} - \frac{1}{T_m}\right]\right) \tag{2.1}$$

T_m is the sublimation temperature of carbon and ΔH is the enthalpy of solution which Scace and Slack estimated to 59$\pm$3 kcal/mol (=247$\pm$13 kJ/mol) through linear regression of their solubility data. The values given by Scace and Slack for the melting point of silicon and the sublimation temperature of carbon, 1408 and 3730 °C, indicate a solubility of 15 ppmm at the melting point. However, they have used the near melting point value of Dash as the starting point of their regression.

The year before, Hall [20] had also determined an equation for the solubility of carbon in liquid silicon based on gravimetric measure-

ments. He equilibrated liquid silicon with SiC crystals in the temperature range between 1520–1725 °C, quenched the samples and measured the weight loss of the SiC crystals to determine the solubility. He also supplemented his results with near melting point data from Dash, although interestingly this value (63±33 ppmm) is different from that supplied to Scace and Slack. At the melting point his published equation yields a solubility of 61 ppmm, more than three times that of Scace and Slack. Scace and Slack argue that this can be caused by oxygen entering the melt from the quartz crucibles employed by Hall, and that carbon could have left the melt as CO or CO_2 gas. This would lead to Hall overestimating the solubility, as more carbon would dissolve from the SiC crystals than what was incorporated in the melt. If such a gas-phase transport took place, it would be expected that there was a detectable difference between results obtained at different holding times as more SiC is dissolved into the melt. Hall reports no significant variance in the weight loss of the SiC-crystals when the holding time is varied by a factor of two. Scace and Slack however, make reference to the work of their colleague Racette [19] who observed an apparent increase in solubility with holding time, using fused quartz crucibles and a set-up similar to that of Hall.

As pointed out by Olesinski and Abbaschian in their 1984 review [21], Scace and Slack might themselves be in error. The major uncertainty of their work stems from the SiC layer that formed on the surface of the sample. Scace and Slack assumed that the entire carbide layer had formed at high temperatures, and that no SiC formed in this layer during quenching. This assumption is possibly erroneous, as the carbide layer will likely have functioned as a nucleating substrate for the growth of SiC during quenching. If this is the case, then the solubility will have been underestimated. Durand and Duby agree with this assessment in their 1999 review [22]. The supposed precipitation of SiC during quenching is not in agreement with what has been observed during the current work, as will become clear in

later chapters. However, in the experiment of Scace and Slack, SiC can grow on an already existing SiC substrate, while in the current work it has to nucleate in the melt or on the SiO_2. It is to be expected that the nucleation kinetics differ between these two cases.

In 1960 Dolloff and his team at Wright Air Development Division published a thorough analysis of the Si-C system and constructed a phase-diagram [23]. They examined the cooling curves of silicon melts with 5 to 50 at.% carbon and determined the eutectic temperature to 1402 ± 5°C. Metallographic and X-ray investigations confirmed SiC platelets in a silicon matrix, as would be expected for a eutectic reaction. Work was also performed on the liquidus line, in which silicon and SiC were heated to temperatures between 1500 and 2600 °C in graphite crucibles and the quenched samples were chemically analysed for carbon content. An extrapolation of their liquidus data gave the eutectic composition as 0.75±0.5 at.% (∼3200±2000 ppmm). Olesinski and Abbaschian argued in favour of the validity of the work of Dolloff [21]. However, when comparing the compositional value of their eutectic point with that of other publications, it seems unnaturally high. Durand and Duby [22] dismiss Dolloff's liquidus data, guessing that graphite particles could have been incorporated in the analysed samples.

After these early publications, despite there being a considerable spread in the limited set of available data, not much was done with respect to the liquid solubility of carbon for several decades. Some work was done on the solid phase however, presenting solid solubility data and/or distribution coefficients.

The fact that carbon is substitutionally dissolved in solid silicon was established in 1965 by Newman and Willis using IR-spectroscopy to investigate solid samples of silicon doped with ^{12}C, ^{13}C and/or ^{14}C [24]. They also published an early estimate of the distribution coefficient, estimating $k = 0.005$ based on the concentration profile of ^{14}C found by measurement of β-radiation compared with a ^{14}C-

standard.

This was followed by a publication in 1969 by Haas et al. [25] who also used C^{14}-radioisotopic tracing to investigate the distribution coefficient of carbon. They performed zone melting techniques and determined the concentration gradient of carbon in the direction of pulling. From their observations, they estimated the distribution coefficient of carbon in silicon to be in the region of 0.1, in poor agreement with the number provided by Newman and Willis.

This discrepancy was commented upon in 1971 by Bean and Newman [26], who used infrared measurements on annealed single crystal samples to find the solid solubility of carbon as a function of temperature. Extrapolating to the melting point, they reported a solid solubility of 4.5×10^{17}Atoms/cm^3 (=3.8 ppmm). Because of the inconsistency in the two distribution coefficients available in the literature at the time, the authors only made a conservative estimate on the solubility in the liquid phase, demonstrating the divergence between their own results and those of Scace and Slack [19].

Another value for the distribution coefficient was made available that same year by Nozaki et al. [27]. Through charge particle analysis of a series of samples prepared by the zone melting of carbon-painted silicon rods, they determined the equilibrium distribution coefficient of carbon to $k_0 = 0.07 \pm 0.01$, more in agreement with Haas et al. than with Newman and Willis. Nozaki et al. also investigated the solubility of carbon in solid silicon. They found that the formation of SiC on the surface of solidifying silicon was only observed for carbon concentrations greater than $3.5 \pm 0.4 \times 10^{17}$Atoms/cm^3(= 3 ± 0.3 ppmm), and they took this to be the solubility limit of carbon in solid silicon at the melting point of silicon. Using this value with their found distribution coefficient the solubility in the liquid phase can be calculated to 43±4 ppmm.

In 1972, Endo et al. [28] used infrared spectrometry calibrated with charged particle activation to create an equation describing the solubil-

ity of carbon in solid silicon as a function of temperature. Using their found value for the enthalpy of solution, $\Delta H = 55$ kcal/mol (=230 kJ/mol), the solubility at the melting point can be calculated as 2.5 ppmm.

A year later Voltmer and Padovani [29] used double-beam infrared spectroscopy with a carbon-free silicon sample as reference. Assuming that dislocations formed as a result of SiC precipitation, they determined the carbon concentration at which point the crystalline perfection of Czochralski grown silicon broke down, and took this to be the solubility limit of carbon in solid silicon. The value found was $9 \times 10^{17} A/cm^3$ (=8 ppmm). Using the partition coefficient of k_0=0.07 as reported by Nozaki et al. [27], they also calculated a liquid solubility of $1.3 \times 10^{19} A/cm^3$ (=110 ppmm.)

As part of a study on the behaviour and effects of carbon in silicon in 1982, Kolbesen and Mühlbauer [30] performed a float zone experiment similar to that of Nozaki et al. but using IR-methods for the chemical analysis. They determined the effective distribution coefficient at varying growth rates and through an extrapolation to zero growth rate the equilibrium distribution coefficient was determined to 0.058±0.005. Their extrapolation was performed in a semilog-plot, unlike Nozaki et al. who used a linearly axed plot. Performing an extrapolation of the experimental data of Nozaki using the semilogarithmic scheme, they obtained $k_0 = 0.057 \pm 0.004$, very close to their own result.

In 1987, Oden and McCune [31] published an article on phase equilibria in the Al-Si-C ternary system, a part of which was an investigation on the liquidus of the binary Si-C-subsystem in the 1700–2150 °C temperature range. They saturated samples with carbon in graphite crucibles at high temperatures and quenched them at ∼23 °C/s. The crucibles and the outer 0.065 cm of the samples were removed by diamond grinding before the samples were analysed in a Leco instrument. An extrapolation of their results to the melting point of silicon gives a liquid solubility limit of only 6 ppmm. As pointed out by Søiland [32],

this would imply that either the solid solubilities or distribution coefficients reported in the literature are wrong by a factor ∼10. Durand and Duby [22] suggest that SiC particles had nucleated near the outer surface of the samples and been lost in sample preparation.

Both Yanaba et al. [33] and Seifert and Aldinger [34] make reference to a work by Suhara et al. [35] from 1989 which is only available in Japanese. It is reported [33] that three solubility data points are published in this work: 60, 70 and 90 ppmm at temperatures of 1430 °C, 1460 °C and 1510 °C, respectively. An extrapolation to 1414 °C gives 55 ppmm as the solubility limit at the melting point.

In 1993, Ottem [36] investigated the solubility of carbon in both liquid silicon and high silicon ferrosilicon alloys between 1420 °C and 1640 °C. Like Oden and McCune, he used a Leco analyser on rapidly quenched samples, but no material was lost in sample preparation. His results indicate a solubility limit of 59 ppmm carbon in liquid silicon at the melting point.

In the same year, Kleykamp and Schumacher published a Si-C phase diagram [37]. They used data from Voltmer and Padovani [29] as well as their own analyses of samples prepared in an arc-melting furnace. Among their own results were four points on the liquidus line between 1420 °C and 2830 °C. The extrapolated value from these data points to 1414 °C is 229 ppmm, but it is perhaps more relevant to consider their reported value at 1420 °C: 85±43 ppmm.

Yanaba et al. [33] determined an equation for the solubility limit as a function of temperature in 1997. Their quenched samples were prepared in the region between 1450–1600 °C and analysed using an IR-absorption method. Their published equation gives 79 ppmm as the solubility at the melting temperature when an extrapolation is performed.

In 1998 Durand and Duby wrote a review [22], critically assessing the available literature for direct measurements of the solubility of carbon in solid and liquid silicon. In their assessment of the liquid

solubility from a set of available data [19, 20, 23, 31, 37] they chose the results of Hall [20], Kleykamp [37] and the near melting point data of Dash [19, 20]. They created the following model for the solubility (in mole fraction) of carbon in liquid silicon as a function of temperature:

$$log(X_C) = 2.714 - \frac{10623}{T} \tag{2.2}$$

This model gives the solubility at the melting point as 112 ppmm, which is higher than all the values obtained by the three publications on which they based their study. This may be caused by the influence of the higher temperature measurements which will influence regression. It could also be noted that the results of Yanaba [33], Ottem [36] and Suhara [35], all reporting lower solubilities, were not considered in this review.

Narushima and Iguchi, two co-authors from the work of Yanaba on liquid solubility, published a paper on the solid case together with Yamashita and Ouchi in 2002 [38]. Equilibrating solid samples with silicon carbide at 1400 °C for 4860 ks (∼56 days), they then measured the carbon content using a combustion-IR absorption method. They determined the solubility limit of carbon in solid silicon at 1400 °C to 24 ± 13 ppmm. Using their own previous results from the liquid phase, they calculated an equilibrium distribution coefficient of $k_0 = 0.30 \pm 0.16$. Both their solubility data and distribution coefficient are greater than previously reported numbers.

The thermodynamical results discussed in this section are summarised in Tables 2.1-2.3 and Figure 2.2. Table 2.1 summarises the values for liquid solubility obtained at the melting point of silicon, through extrapolation where appropriate, while Table 2.2 presents the same information in the solid phase. Figure 2.2 illustrates the results from the liquid phase graphically, while the available distribution coefficients are listed in Table 2.3.

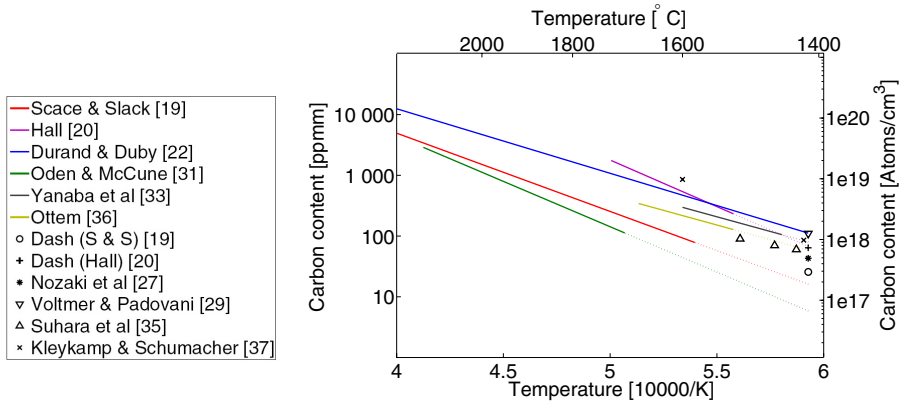

Figure 2.2: Graphical representation of literature data on the solubility of carbon in liquid silicon. Dashed lines represent extrapolations outside the investigated temperature range.

Table 2.1: Solubility of carbon in liquid silicon at the melting point of silicon (1414 °C). Results marked with an asterisk(*) represent extrapolations outside the area of experimentation.

Author(s)	Solubility [ppmm]	Reference
Hall	61[1]	[20]
Scace and Slack	11[1]	
Dash	26	[19]
Dash	63±33	[20]
Dolloff	3200	[23]
Nozaki et al.	43±4	[27] (Calculated from solid solubility using reported partition coefficient.)
Voltmer and Padovani	110	[29] (Calculated from solid solubility using partition coefficient from Nozaki et al. [27].)
Oden and McCune	6*	[31]
Suhara et al.	55*	[35] ([33, 34])
Ottem	59*	[36]
Kleykamp and Schumacher	85	[37] (at 1420 °C)
Kleykamp and Schumacher	229*	[37] (extrapolated)
Yanaba et al.	79*	[33]
Durand and Duby	112	[22] Review based on the results of Hall [20], Dash [19, 20] and Kleykamp [37].

[1]Even though these results represent an extrapolation outside the work of the authors, they do incorporate the data of Dash at the melting point of silicon. I have therefore not defined these results as extrapolations.

Table 2.2: Solubility of carbon in solid silicon at the melting point of silicon (1414 °C). Results marked with an asterisk (*) represent extrapolations outside the area of experimentation.

Author(s)	Solubility [ppmm]	Reference
Bean and Newman	3.8	[26]
Nozaki et al.	3±0.3	[27]
Endo et al.	2.5*	[28]
Voltmer and Padovani	8	[29]
Narushima et al.	24 ± 13[2]	[38]

[2]At 1400 °C.

Table 2.3: Distribution coefficients of carbon in silicon as reported in the literature

Author(s)	Distribution coefficient	Reference
Newman and Willis	0.005	[24]
Haas et al.	∼0.1	[25]
Nozaki et al.	0.07±0.01	[27]
Kolbesen and Mühlbauer	0.058±0.005	[30]

2.1.2 The Si–B binary system and boron in silicon

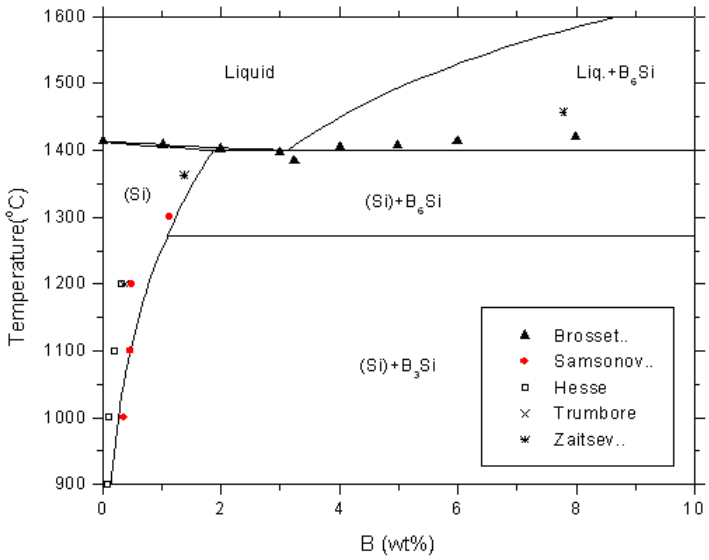

Figure 2.3: Phase diagram for the silicon rich part of the Si–B system, modelled by Tang [16].

In addition to the solid solutions, the Si–B system displays three different solid phases: The regular intermediate phases SiB_3 and SiB_6, as well as the boron-rich intermediate phase SiB_n, with $14 < n < 40$.

The interest in boron as a trace element in silicon is mainly from a doping-perspective. Boron is the most common dopant used in the production of p-type silicon. The doping is typically done by the addition to the feedstock of a silicon alloy nearly saturated with boron.

The good doping properties of boron are tied to its solubility in silicon as well as to its distribution coefficient being high enough to obtain a sufficiently high and uniform dopant concentration.

Some authors have reported the SiB_3 phase as SiB_4. One reason behind this confusion is that SiB_3 has a homogeneity range [34]. In 1960, Brosset and Magnusson [39] reported a silicon content of up to 48 m.% in what they labeled SiB_4, corresponding to $SiB_{2.81}$. Two years later, the same authors determined the crystal structure of the compound through X-ray investigations. They reported that their crystallographic results suggested a $SiB_{2.89}$ composition, and that their chemical analyses and density measurements supported this result [40]. Ettmayer et al. [41] identified and determined the composition of three distinct phases, $SiB_{3.65}$, SiB_6 and $SiB_{19.4}$. Arabei [42] reported a homogeneity range of 72.6–77.1 at.% boron ($SiB_{2.6}$–$SiB_{3.4}$) for the SiB_3-phase. In their 1984 review [43], Olesinski and Abbaschian recommended the homogeneity range to be defined from the results of Brosset and Magnusson [40] and Ettmayer [41], and proposed a homogeneity range from $SiB_{2.89}$ to $SiB_{3.65}$.

The SiB_6 phase has also been reported to display a homogeneity range, although narrower than SiB_3. In fact, Olesinski and Abbaschian accepted it as a stoichiometric phase in their review [43]. However, in 1979 Arabei [42] had already reported the existence of a homogeneity range, and in 1986 Vlasse et al. [44] quantified the homogeneity range as $SiB_{5.7}$–$SiB_{6.1}$.

Considering the Si-rich part of the phase diagram, silicon will be in equilibrium with different intermediate phases at different temperatures. At low temperatures, solid silicon with substitutionally dissolved boron will be in equilibrium with SiB_3. Between 1270 °C and 1850 °C, silicon—in liquid or solid form—is in equilibrium with SiB_6. This temperature range incorporates the Si–SiB_6 eutectic temperature at 1385 °C. At temperatures above 2396 °C, the liquid phase is equilibrated with SiB_n which decomposes at 2073 °C. Between this

temperature and the melting point of boron, silicon will be in equilibrium with a boron–silicon solid solution.

The determination of the temperatures just quoted has been the subject of a few publications. Brosett and Magnusson [39] noted that SiB_3 slowly decomposed into SiB_6 and silicon at temperatures between 1200 °C and 1380 °C. Lugscheider et al. [45] investigated the Si–B system between 20 °C and 1500 °C using DTA. They reported that an $Si_{11}B_{31}$-phase was formed in a peritectoid reaction at 1340 °C. Although $Si_{11}B_{31}$ corresponds to a $SiB_{2.82}$-phase that lies outside the homogeneity range recommended by Olesinski and Abbashcian, there can be no doubt that the investigated phase is the SiB_3 phase, and 1340 °C can be understood as the measured decomposition temperature of this phase.

Lugscheider et al. [45] also reported on the SiB_6-phase, observing that it formed in a peritectic reaction at 1864 °C and that it shared a eutecticum with Si at 1363 °C and 19 at.% boron (=7.3 m.%).

Arabei [42] determined the peritectic SiB_6 decomposition temperature to 1850 °C and the results of Armas et al. [46] are in good agreement with Arabei. They reported that the peritectic SiB_6 decomposition took place at 1850±15 °C and the decomposition of SiB_n at 2020±15 °C.

In their review, Olesinski and Abbaschian calculated a Si–B phase diagram in which different important temperatures can be read as follows: The SiB_3 peritectoid reaction takes place at ∼1270 °C, the eutectic point is at 3.2 m.%B and 1385 °C while the SiB_6 and SiB_n peritectic reactions take place at 1850 °C and 2020 °C respectively. Seifert and Aldinger also calculated a Si–B phase diagram based on a literature review [34]. In contrast to Olesinski and Abbaschian, they accepted a homogeniety range for SiB_6, although the two phase diagrams nonetheless look very similar. The temperatures for the eutectic point and all decomposition reactions are identical except for the decomposition of SiB_n, which Seifert and Aldinger reports to take

place at 2037 °C. The eutectic compositions are also in agreement, given as approximately 8 at.%B (∼3 m.%) by Seifert and Aldinger.

The mutual solubilities in liquid and solid phases have been investigated by several authors, but here as well there have been conflicting results reported.

In 1963 Samsonov and Sleptsov [47] investigated the solubility of boron in solid silicon through an analysis of the silicon lattice parameter. Based on their results from temperatures between 25°C and 1300°C, they estimated the solubility at the eutectic temperature to 3.6 at.% (=1.4 m.%).

Olesinski and Abbaschian [43] compares the results of Samsonov and Sleptsov with those found by Hesse [48], who used electrical conductivity and Hall effect techniques. The data of Hesse generally point to lower solubility levels than those of Samsonov and Sleptsov, and taking both data sets into account, Olesinski and Abbaschian estimated the solid solubility to be $\sim$ 1.2 m.%B at the eutectic temperature.

A few papers not considered by Olesinski and Abbaschian [43] reported a significantly lower solubility. In 1969 Vick and Whittle [49] reported a solid solubility ranging from 1.6×10^{19} atoms/cm^3(=0.012wt%) at 700 °C to 2.4×10^{20}atoms/cm^3 (=0.18 m.%) at 1151 °C. Extrapolating these results to the eutectic point yields 0.51 m.%. Five years later, Schwettmann found even lower solubility levels, ranging from 0.03–0.09 m.% between 800 °C and 1000 °C which extrapolates to 0.4 m.% at the eutectic. However in 1980, Ryssel et al. [50] reported values in better agreement with Olesinski and Abbaschian. They reported a solubility limit ranging from 0.01 to 0.1 m.% boron between 800 °C and 1000 °C, indicating a maximum solubility of 1.25 m.% at the eutectic temperature.

As opposed to Olesinski and Abbaschian, Seifert and Aldinger did include the low solubility results in their review. From their phase diagram the maximum solubility can be read as 0.4 m.%B [34].

The only publication found on the solubility of silicon in solid boron

is a 1981 publication by Armas et al [46]. They reported a maximum solubility of 3 ± 0.4 at.%($= 8 \pm 1$m.%) at 2020±15 °C. Up to this temperature, they reported an increasing solubility with temperature.

On the subject of liquid solubility, an early work was performed by Brosset and Magnusson [39] in 1960, in which they reported ten points on the liquidus curve. From these data, they concluded that there was a eutectic point "at about 3 m.%B", for which they reported a melting temperature of 1403 °C. However, they reported the melting point for pure silicon as 1420 °C, so their temperature measurements are probably in error. Olesinski and Abbaschian downscaled all temperatures reported by Brosset and Magnusson with 6 °C and used this data together with data from Malé and Salanoubat [51] to calculate the liquidus line. They used a eutectic temperature of 1385 °C, accepting the work of Malé and Salanoubat [51] and Armas et al. [46], and the eutectic composition of 3 m.%B as suggested by Brosset and Magnusson [39]. Their calculation gave a maximum boron solubility in liquid silicon as 3.2 m.%B.

Much of the work on the distribution coefficient of boron in silicon has been done through resistivity measurements on high-purity silicon doped with boron. In such a material, there is a clear link between the resistivity and the boron level as shown by Thurber et al. [52].

Huff et al. determined the distribution coefficient of boron in Czochralski grown silicon to $k_e = 0.7$ [53]. Sim et al. reported $k_e = 0.738 \pm 0.006$ [54], also in Czochralski silicon . Working with both single and polycrystalline silicon, Ravishankar et al. [55] reported a slightly higher value for the polycrystalline case: $k_e = 0.786 \pm 0.036$ in Czochralski single crystals and $k_e = 0.803 \pm 0.036$ in Bridgman polycrystals [55]. Table 2.4 summarises experimental data on the Si–B system.

Table 2.4: Overview of available thermodynamic data on the Si–B system from the literature. Extrapolated results are marked with an asterisk (*).

Property	Result	Author(s)	Ref.
SiB_3 decomposition	1200 °C–1370 °C	Brosset and Magnusson	[39]
temperature	1340 °C	Lugscheider et al.	[45]
	∼1270 °C	Olesinski and Abbaschian	[43]
	1270 °C	Seifert and Aldinger	[34]
SiB_6 decomposition	1864 °C	Lugscheider et al.	[45]
temperature	1850 °C	Arabei	[42]
	1850±15 °C	Armas et al.	[46]
	1850 °C	Olesinski and Abbaschian	[43]
	1850 °C	Seifert and Aldinger	[34]
SiB_6-Si eutecticum	3wt.%B, 1403 °C	Brosset and Magnusson	[39]
	3.2wt.%B, 1385 °C	Olesinski and Abbaschian	[43]
	7.3wt.%B,1363 °C	Lugscheider et al.	[45]
	∼3 m.%B, 1385 °C	Seifert and Aldinger	[34]
Solubility of B in	1.39wt.%	Samsonov and Sleptsov	[47]
solid Si at	0.51wt.%*	Vick and Whittle	[49]
eutectic point.	0.4 m..%*	Schwettmann	[56]
	1.25 m.%*	Ryssel et al.	[50]
	1.15 m.%	Olesinski and Abbaschian	[43]
	0.4 m.%	Seifert and Aldinger	[34]
Distribution coefficient	0.7	Hall	[57]
of boron in silicon	0.7	Huff et al.	[53]
	0.786±0.036	Ravishankar et al. (Czochralski)	[55]
	0.803±0.036	Ravishankar et al. (Bridgman)	[55]
	0.738±0.006	Sim et al.	[54]

2.1.3 The Si-N binary system and nitrogen in silicon.

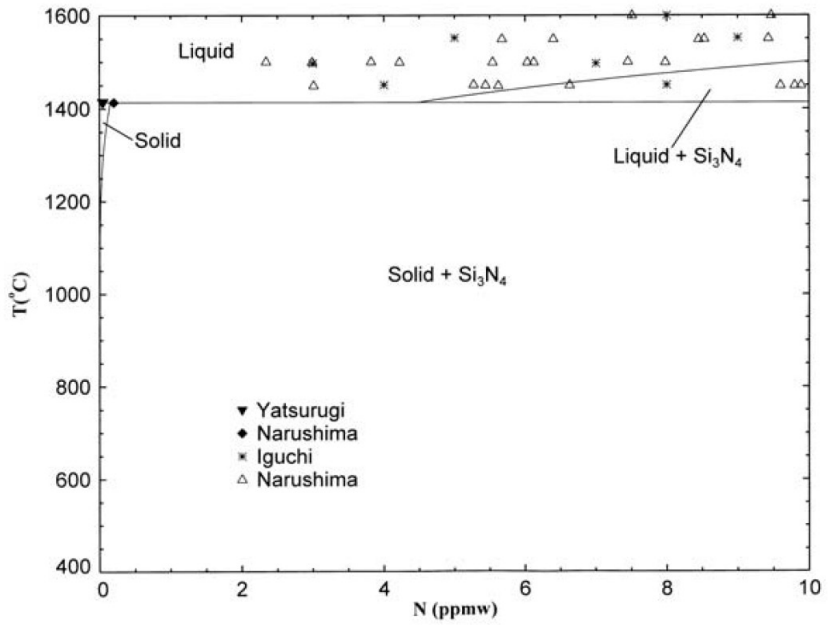

Figure 2.4: Phase diagram for the nitrogen-rich portion of the Si-N system. From [17].

The only stable compound in the Si-N system is silicon nitride, Si_3N_4. It appears in two modifications[1], α-Si_3N_4 and β-Si_3N_4, with similar crystal structures and densities. α-Si_3N_4 is a metastable configuration and will transform into β-Si_3N_4 at elevated temperatures.

[1] A third polymorph is reported at high temperatures (>2000K) and pressures(>15GPa)[58].

The fact that a β-α transition is not observed on either heating or cooling demonstrates the metastability of α-Si_3N_4.

The solubility of nitrogen in silicon is small, and has been the subject of several publications. However, the spread in the available data is unfortunately rather large. Using zone melting experiments in which they saturated the liquid silicon with nitrogen from N_2 and NH_3 in 1959, Kaiser and Thurmond [59] estimated the solubility of nitrogen in liquid silicon as 200 ppma (99.7 ppmm) at the melting point of silicon. The quantification of the nitrogen levels was achieved through vacuum fusion gas analysis.

In 1973, Yatsurugi et al. [60], using charged particle activation analysis of rapidly quenched samples, found a liquid solubility of $6{\cdot}10^{18}$ atoms/cm^3 (60 ppmm) for temperatures at, or slightly above, the melting point. They also reported a solid solubility limit of $4.5{\pm}1.0{\cdot}10^{15}$ at/cm^3 (0.045 ppmm), also at the melting point. From these data, they calculated the equilibrium distribution coefficient to be $7{\cdot}10^{-4}$.

In 1994, Narushima et al. [61] examined the temperature dependence of nitrogen solubility in liquid silicon equilibrated with Si_3N_4. Their quenched samples were analysed using the Kjeldahl method, a photo-absorption method. Their results imply a solubility limit of 4 ppmm at the melting point of silicon, differing from the earlier results of Kaiser and Thurmond and Yatsurugi et al. with an order of magnitude. From their results, they calculated an equation for the dissolution energy of nitrogen presented in Table 2.5 together with other similar results.

Tanahashi et al. [62] published an article in Japanese in 1998 that has unfortunately not been translated into English. However, the figure and table texts as well as the abstract were given in English, and it can be understood that they did two solubility investigations at each 1450 °C and 1500 °C, reporting values around 40 and 61 ppmm respectively. Extrapolated to the melting point of silicon, their results

Table 2.5: Equations from literature describing the temperature dependence of the dissolution energy of nitrogen [J/mol]

$\Delta G_{1/2N_2 \rightleftharpoons \underline{N}}(T)$	ΔG at m.p. of Si	Temperature-range [°C]	Authors [reference]
$-44500 + 66.4T$	68000	1450–1600	Narushima et al. [61]
$207000(\pm 3000) - 79.4(\pm 17.8)T$	73000	1450–1650	Noguchi et al. [64]
$-36200(\pm 23500) + 39.8(\pm 13.6)T$	31000	1420–1650	Yoshikawa & Morita [63]

point to a solubility of 28 ppmm.

An investigation into the Si-Al-B-N system was published by Yoshikawa and Morita [63] in 2005. They prepared various Si-B alloys and equilibrated them with Si_3N_4 and BN before quenching. The nitrogen content was analysed by use of an unspecified Leco instrument.

Among their results were three points from the pure Si-N system on the solubility of nitrogen in liquid silicon equilibrated with Si_3N_4 under a 90% N_2-atmosphere. They reported nitrogen levels of 77 and 86 ppma (38 and 43 ppmm) at 1420 °C and 147 ppma (73.3 ppmm) at 1500 °C which extrapolates to 39 ppmm at the melting point. They also presented an equation for the dissolution energy of nitrogen. Table 2.5 compares their equation with that of Narushima et al. and also includes a result from Noguchi et al. [64], obtained from a work on the $Si_{(l)}$-$BN_{(s)}$ equilibrium (see Section 2.1.6). Yoshikawa and Morita comment on the discrepancies between their own results and those of Narushima et al., and point out the large scatter in the data of Narushima et al. The solubility data presented in this section is summarised in Table 2.6.

While the big scatter in the published results makes it difficult to draw any clear conclusions about the real solubility levels, the results of Kaiser and Thurmond [59] and Narushima et al. [61] represent the extremes of the spectrum and can be addressed. Kaiser and Thurmond indicated the appearance of glow discharges in their experiments and reported an increased reactivity following these discharges. They explain this increased reactivity by the presence of "active nitrogen" [59]—an excited species of nitrogen with increased activity in chemical reactions associated with glow discharges through a nitrogen atmosphere [65]. As pointed out by Narushima et al. [61], this high reactivity of the active nitrogen could be the reason behind the high levels of solubility.

The results of Narushima et al. are at great variance with all other published results that have been found. In their publication, they argue the reliability of their results from an enthalpy consideration. The argument is put forward that the ratio between their found enthalpy of dissolution of nitrogen in silicon at the melting point of silicon, and the enthalpy of formation of Si_3N_4 at room temperature, follows the general trend for enthalpies of nitrogen dissolution and nitride formation for other metals such as Fe, Co and Li. They cite a previous work by the same authors [66] that demonstrated that such a trend exists for oxygen dissolution and oxide formation. They do concede that the available data does not allow for a quantitative examination of the correlation, but point to a qualitative trend that the ΔH° of nitrogen dissolution decreases with decreasing $\Delta H^\circ_{298}(Me_aN_b)$ of nitride formation. The relevance of this argument however can be cast in doubt: When calculating the Gibbs free energy and the enthalpy of dissolution from solubility data, the absolute values of the solubility levels do not influence the enthalpy of dissolution. Rather, it is the slope of the solubility versus temperature that needs to be considered. This means that the solubility levels could be several orders of magnitude greater or smaller, and from the enthalpy argument of Narushima et

al., the results would still be considered reliable.

As part of her doctoral work [32], Søiland extracted samples from the liquid phase of silicon during directional solidification and had them analysed with Leco. In 2004, together with Øvrelid et al., she published an investigation of the evolution of the total nitrogen content during the solidification process [13]. She found that the nitrogen levels decreased over time during the solidification process. Having found small β-Si_3N_4-precipitates near the bottom of the crucible, she concluded that the melt had been saturated at the beginning of solidification and that the decrease in nitrogen was due to continuous precipitation from a saturated melt throughout the solidification. The melt temperature naturally also decreased over time during the solidification, and the authors conclude that their observations are consistent with the expected qualitative temperature dependency of the solubility. Assuming that the measured nitrogen levels represented the solubility limit at the temperature indicated by the surface temperature of the melt, they tentatively indicated a solubility of 8 ppmm at the melting point of silicon. This observation is in agreement with Narushima et al. [61].

Since these observations were done during directional solidification, it is possible that the degree of mixing in the liquid may have influenced their results. Silicon nitride particles typically grow at the liquid-solid interface, and therefore the boundary region will come into play. The nitrogen content in the boundary region will be higher than in the rest of the melt, possibly leading to a scenario in which this region is saturated while the rest of the melt is not. This would lead to an underestimate of the solubility limit, as the assumption of a saturated melt is erroneous.

Table 2.6: Solubility of nitrogen in liquid silicon at the melting point of silicon (1414 °C). Results marked with an asterisk (*) represent extrapolations outside the area of experimentation.

Author(s)	Solubility [ppm mass]	Reference
Kaiser and Thurmond	99.7	[59]
Yatsurugi et al.	60	[60]
Narushima et al.	4*	[61]
Tanahashi et al.	28*	[62]
Yoshikawa and Morita	39*	[63]
Søiland et al.	8	[13]

2.1.4 The B-C-N ternary system and its binary subsystems

The scope of this work has been the study of the roles of carbon, nitrogen and boron as impurities in silicon. The most relevant systems to this discussion are the ones containing silicon with one or more impurities. While the different impurity-impurity systems have not been directly examined, the impurity-impurity interactions are important to the understanding of the different ternary and quaternary systems. Therefore in the following, I will give brief overviews of the B-C, C-N and B-N binary systems as well as the B-C-N ternary system.

The B-C binary system There exists only one intermediate compound: boron carbide. According to Seifert and Aldinger [34], early works by Samsonov et al. [67] and Zhuravlev et al. [68] reported several boron rich carbides. However, Dolloff [23] reported only one carbide and others have since ascertained this result.

In its pure stoichiometric form, B_4C, it is a very hard ceramic with applications in tank armour and bulletproof vests. In the B-C phase diagram it exists in a broad homogeneity range, and several notations are applied in order to distinguish it from its stoichiometric form such as (B_4C), $B_{13}C_{\pm x}$, B_{12}(B, C)$_3$ or $B_{4+\delta}C$ [34].

According to Seifert and Aldinger [34], an early work on the system was performed by Elliot and van Thyne in 1961 [69] in which they reported a single boron carbide phase with a homogeneity range of 9-20 at.% carbon. They also determined a eutectic point at 29% carbon and 2648K. With small deviations, this work was confirmed by Kieffer et al. in 1971 [70]. According to Seifert and Aldinger [34], this data remain valid.

The B-N binary system The only stable solid compound in the B-N system is boron nitride, BN. It exists in four crystallographic modi-

fications: Hexagonal (α-BN), cubic (β-BN), rhombohedral (r-BN) and wurtzitic (γ-BN) [34]. Using CVD, high boron compounds have been observed, including B_4N [71] and $B_{25-53}N$ [72]. The hexagonal α-BN, sometimes written as h-BN, has a structure similar to graphite. It is the thermodynamically stable compound at low pressure and high temperature. At higher pressures and/or lower temperatures, it transforms into the cubic β-BN, which is a material of hardness comparable to diamond. The exact p-T stability regions of the two modifications are not well established. The rhombohedral and wurtzitic modifications are both metastable modifications.

The C-N binary system No intermediate compounds exist at normal pressures, where graphite is the only stable solid. In 1989 Liu and Cohen [73] proposed the existence of a covalent C-N solid with structure similar to that of β-Si_3N_4, i.e. C_3N_4. It has since been observed at high pressures [74].

In an isolated system with graphite and N_2 gas, CN and $(CN)_2$ will be present in the gas phase at equilibrium. HSC calculations suggest equilibrium partial pressures at 1400°C of $5 \cdot 10^{-7}$ and $2 \cdot 10^{-6}$ for CN and $(CN)_2$ respectively.

The B-C-N ternary system With the combination of B, C and N into a ternary system, no new stable solid compounds are introduced; all solid compounds are bi-elemental. Metastable solid solutions of the form $B_xC_yN_z$ have been observed [34]. Ruh et al. [75] investigated the mutual solubility of B_4C and α-BN at T=2523 K. They reported a slight solubility of B_4C in α-BN, but no solubility of α-BN in B_4C.

While no stable tri-elemental compounds are observed, some trielemental equilibrium reactions have been proposed. These are listed in the table 2.7.

Table 2.7: Trielemental equilibrium reactions in the B-C-N system

1	$gas + liquid$	$\rightleftharpoons$	B_4C
2	$gas + liquid$	$\rightleftharpoons$	$BN + B_4C$
3	$gas + B_4C$	$\rightleftharpoons$	$C + BN$
4	$liquid + B_4C$	$\rightleftharpoons$	$B + BN$

2.1.5 The Si-B-C ternary system and carbon-boron interactions in silicon.

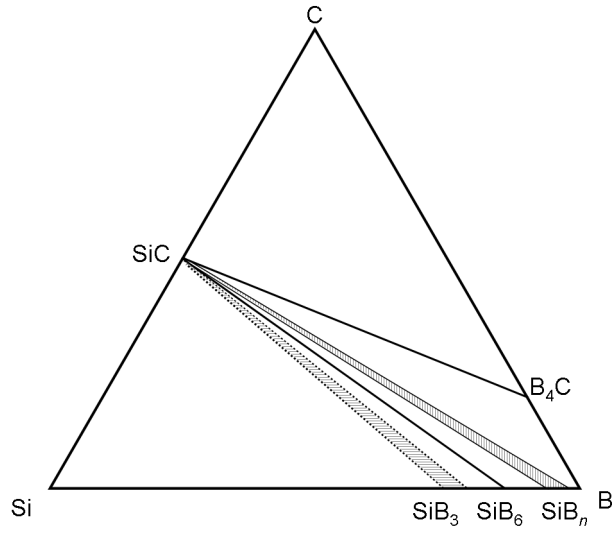

Figure 2.5: Schematic phase diagram of the Si-B-C system.

The stable intermediate compounds in this system are silicon carbide, SiC; boron carbide, $B_{4+\delta}C$; and the silicon borides: SiB_3, SiB_6 and SiB_n. No ternary compounds exist. A number of tri-elemental equilibrium reactions are observed in the Si-B-C system, and these are summarised in table 2.8. Of particular interest for solar applications are the reactions

$$liquid \rightleftharpoons Si + SiB_6, B_4C \tag{2.3}$$

which represents the quasi-eutectic solidification of a silicon rich melt

Table 2.8: List of equilibrium equations in the Si-B-C system. Data from Seifert and Aldinger [34].

Temperature [°C]	
2385	*liquid*+C⇌ B_4C+SiC
2005	*liquid*+B⇌ B_4C+SiB_n
1850	*liquid*+SiB_n ⇌ SiB_6, B_4C
1396	*liquid*+SiC ⇌ B_4C+Si
1384	*liquid* ⇌ Si + SiB_6, B_4C
1198	Si+SiB_6 ⇌ SiB_3, B_4C

at 1384 °C. The product in addition to solidified silicon can be SiB_6 or B_4C depending on the carbon concentration. If sufficient carbon is present, this will precipitate as SiC at 1414 °C but this will react again with boron in the melt forming B_4C and Si at 1396 °C.

The Si-B-C system has been studied mainly with respect to the sintering of ceramics, in particular, the understanding of the mechanisms behind the sintering of SiC with boron and the sintering of boron carbide with silicon [34]. Work has typically been performed on pseudo-binary systems such as B_4C-SiC, B-SiC or B_4C-Si.

In an early investigation of the B_4C-SiC system from 1960, Dolloff et al. [23] reported a ternary eutecticum at 15 at% Si, 30 at% C and 55 at% B (corresponding to 24 m.% SiC-76 m.% B_4C) and 2250 °C.

In the same year microscopic, X-ray, microhardness and chemical studies were performed on the B_4C-Si and SiC-B sections by Portnoi et al [76]. They reported the existence of two ternary phases with an empirical composition of $B_5Si_2C_2$ and $B_3Si_2C_2$. This result was dismissed by later authors [77, 78].

In 1964 Secrist performed an investigation into the B_4C-SiC system using X-ray analyses. He found a quasi-binary eutectic at 70±2 m.% B_4C

and 30±2 m.% SiC and 2300 °C, and furthermore concluded that the solid solubilities of B_4C in SiC and SiC in B_4C were less than 2 m.% at the eutectic temperature. Considering the structure of the SiC, he reported that the α-modification is stable for compositions of more than 50 m.% SiC, whereas the β-modification is stabilised in compositions of less than 50 m.% SiC.

Half a decade later, Schaffer [77] commented on the lack of correlation between this delimiting composition and the eutectic composition. He himself was not able to address this problem, and reported observing both SiC modifications on the SiC-rich side of the eutectic, while only β-SiC was observed on the B_4C-rich side. The eutectic point he determined at 70 mol% B_4C (76 m.%) and 2245±5 °C in reasonable agreement with Secrist. He also reported 0.2 m.% as the upper boundary for the solubility limit of boron in solid α-SiC (equivalent to B_4C in α-SiC) while he reported the solubility of silicon (SiC) in B_4C as "extensive".

In 1972, Gugel et al. [78] found a composition for the B_4C-SiC-eutectic point intermediate of those reported by Secrist and Schaffer, reporting 65 mol% (72 m.%) B_4C while their reported temperature of 2240 °C is closer to the results of Schaffer. They also reported a solubility limit of boron in solid β-SiC at 1800 °C between 4.9 and 5.2 m.%. This is of course much larger than the 0.2 m.% limit proposed by Schaffer, although the comparability of these results is not obvious since they are done with different structural modifications of SiC.

Carbon-boron interactions in silicon

Yanaba et al. [79] investigated the effect of different alloying elements on the solubility of carbon in liquid silicon. They found that the carbon solubility increased with increasing amounts of boron present in the system. From their results they also calculated the carbon-boron interaction parameter in liquid silicon, and found its temperature de-

pendence to follow

$$e_C^B = 0.267 - 602/T \tag{2.4}$$

This expression gives an interaction coefficient of -0.09 at the melting point of silicon, indicating an exponential increase of carbon solubility with boron content. As temperature increases the absolute value of the interaction coefficient decreases, and the effect of boron addition becomes less pronounced. At temperatures of 1982 °C and above, the interaction coefficient becomes positive, and the effect of boron additions is an exponential decrease of carbon solubility. This reduction in solubility will increase with temperature.

Liu et al. [80] performed ab initio calculations on the C-B interactions in silicon. They explained a lowered boron diffusion in the presence of carbon by the formation of boron-carbon-interstitials.

2.1.6 The Si-B-N ternary system and nitrogen-boron interactions in silicon.

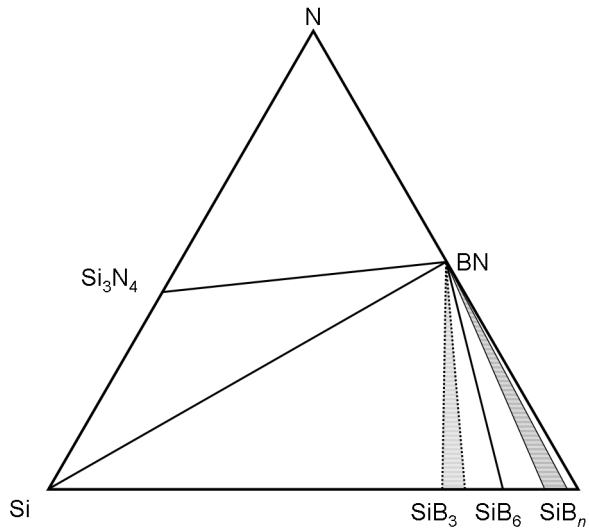

Figure 2.6: Schematic phase diagram of the Si-B-N system.

There is little data available in the literature on this system, both on the system as a whole and on the silicon rich corner of the phase diagram. According to the 2002 review by Seifert and Aldinger [34], no ternary phases have been reported. A silicon rich liquid solution around the melting point of silicon will be in equilibrium with silicon nitride, silicon boride and/or boron nitride.

Since boron and nitrogen form a strong bond in BN, it can be expected that there will also be significant interactions between them in silicon. The results of Noguchi et al. [64], who investigated the simultaneous solubility of boron and nitrogen in liquid silicon, strengthen

this supposition. Equilibrating a silicon melt with a BN crucible at varying p_{N2} and constant temperatures, they observed that a tenfold increase in p_{N2} gave an increased nitrogen content in the melt of almost one order of magnitude and a reduction in the boron content to less than one half. For a constant p_{N2} and varying temperature, they found that both boron and nitrogen solubility increased with temperature. From their results they also computed the boron-nitrogen and nitrogen-boron interaction parameters as $e_N^B = 2.70$ and $e_B^N = 2.07$, respectively.

As will be seen in later sections, the great dependence of nitrogen solubility on p_{N2} is in discordance with the results found in the current work. It is possible that this is because the kinetics of BN dissolution is much slower than that of Si_3N_4. It should be noted however, that Noguchi et al. did not concider Si_3N_4 in their discussion, even though it could perhaps be expected to have formed under the p_{N2}-pressures used in their experiments. Their experiments were performed at p_{N2} between $1.01{\cdot}10^4$ and $1.01{\cdot}10^5$ Pa, while according to Yoshikawa and Morita [63] the dissociation pressure of Si_3N_4 at 1500 °C is only $3.98{\cdot}10^{-3}$ atm ($\approx 4 \cdot 10^2$ Pa).

As mentioned in section 2.1.3, Yoshikawa and Morita published an investigation into the Si-Al-B-N system [63]. Part of their work centred on the Si-Si_3N_4-BN equilibrium, in which they—like Noguchi et al.—observed that both boron and nitrogen content increased with temperature. They reported lower nitrogen contents at a given temperature in the Si-Si_3N_4-BN equilibrium than in the boron free Si-Si_3N_4 system, and calculated estimates of the boron-nitrogen interacion parameter at three different temperatures: $e_N^B = 7.1$ (1425°C), $e_N^B = 5.5$ (1450°C) and $e_N^B = 5.5$ (1500°C). They also computed an expression for the activity coefficient of boron in molten silicon, valid between 1420 and 1650 °C:

$$ln\gamma^0_{B(l)\text{inmoltenSi}} = 1.19(\pm 0.25) + \frac{289(\pm 450)}{T} \qquad (2.5)$$

Yang et al. found a new, thermally stable defect in nitrogen-doped silicon [81]. The defect was only observed in the two samples with the highest boron content of eight samples in total. Since these samples contained virtually no oxygen, and the carbon content was more or less constant for all their nitrogen-rich samples, the defect was suspected to be caused by a boron-nitrogen interaction. The authors were of the opinion that this new defect would not significantly affect the efficiency of solar cells.

2.1.7 The Si-C-N ternary system and carbon-nitrogen interactions in silicon.

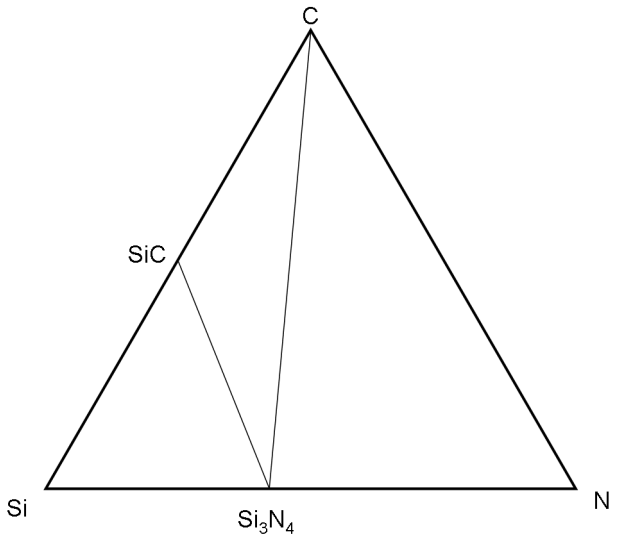

Figure 2.7: Schematic phase diagram of the Si-C-N system.

The merging of the Si-N and Si-C binary systems introduces two new intermediate solid compounds, Si_2CN_4 and β-SiC_2N_4. These compounds were first confirmed synthesised by Riedel et al. in 1997 [82], but are not stable above ∼1000 °C.

Gugel et al. [83] performed an X-ray investigation into the 1400 °C isoterm of the Si-SiC-Si_3N_4 system. They reported that no mutual solubilities or ternary compounds were observed.

In 1975, Kandori et al. [84] investigated the solid solubility of SiC in β-Si_3N_4 through a series of X-ray diffraction experiments. At 1780°C

they reported a solubility limit of 2 m.%.

At elevated temperatures silicon nitride and graphite will react to form silicon carbide and nitrogen gas:

$$Si_3N_4(s) + 3C(s) \rightleftharpoons 3SiC(s) + 2N_2(g) \tag{2.6}$$

The temperature above which this reaction takes place at has been calculated by several authors, who have come up with varying results. The only experimental investigation found was performed by Bill et al. [85], who exposed Si-C-N ceramics to an extended heat treatment at different temperatures in a nitrogen atmosphere. At temperatures above 1438 °C they reported a complete conversion which is taken to be the upper stability limit of a mixture of silicon nitride and graphite.

The solidification of a carbon and nitrogen enriched silicon melt will proceed after the following reaction, where any products in addition to a silicon solid solution depends on the carbon and nitrogen contents:

$$liquid \rightleftharpoons Si, SiC, Si_3N_4 \tag{2.7}$$

Carbon-nitrogen interactions in silicon

Considering that both nitrogen and carbon are common non-doping impurities in silicon, there has been done surprisingly little work on the interactions between the two.

A 1988 photoluminescence study by Dörnen et al. [86] identified five optical defects in silicon attributed to a nitrogen-carbon pairing. While all five defects were observed in Czochralski pulled crystals, only two of them were observed in the almost oxygen-free samples made from float zone silicon. The authors therefore theorised that an oxygen-interaction was necessary for the formation of three of the defects.

Another oxygen-related interaction was reported in 1991 by Hara and Ohsawa when they found that carbon will interact with nitrogen

to suppress the formation of N-O thermal donors [87].

As already mentioned in the introduction, an important aspect of the N-C interactions in high-purity silicon is the nucleation mechanisms of SiC and Si_3N_4 precipitates. These particles have often been observed together, and it has been theorised that Si_3N_4 can serve as nucleation sites for SiC particles [11, 7, 12, 13, 14].

Rakotoniaina et al. [12] reported that SiC filaments very often grew from SiC clusters around Si_3N_4-particles.

2.1.8 The Si-B-C-N quaternary system

No papers were found discussing carbon, nitrogen and boron as mutually interacting trace elements in silicon. A few articles describe thermodynamical equilibria in the Si-B-C-N system from the point of view of high temperature behaviour of ceramics (see for example Seifert and Aldinger [34]; Weinmann et al. [88]). No quaternary compounds have been observed.

From the previous sections on binary and ternary systems, the following conclusions can be drawn about the silicon rich portion of the Si-C-N-B-system, and about what observations to expect in this system at temperatures just above the melting point of silicon:

- In the binary subsystems, a liquid silicon solution will be in equilibrium with SiC, Si_3N_4 or SiB_6.
- In ternary and quaternary systems, it can also be expected that silicon is in equilibrium with a combination of SiC, Si_3N_4 and SiB_6, with the addition of BN in systems containing both boron and nitrogen.
- No ternary compounds will be observed, as the only reported ternary compounds in the system are the silicon carbo-nitrides that are unstable above ∼1000 °C.
- In all three binary subsystems of the trace elements, intermediate compounds are observed, suggesting potential interactions between them in silicon.
- It has been observed that carbon solubility increases with boron content.
- It has been observed that boron solubility decreases with nitrogen content and that nitrogen content decreases with boron content.

2.2 Thermodynamics of solutions

As this is a thesis concerned with the experimental acquisition of thermodynamical data, a brief summary of a few thermodynamical topics central to the discussions is in order. The paragraphs of this section are intended only as a quick review of already familiar topics. A more thorough discussion can be found in any one of the vast number of available textbooks on thermodynamics, with Stølen and Grande's 'Chemical thermodynamics of materials' [89] as one example.

2.2.1 Chemical potential, equilibrium and ideal solutions

In thermodynamics, the most commonly employed measure of a system's total energy is the Gibbs energy, G. It is defined as the maximum amount of non-expansion work that can be extracted from the system. Mathematically, it is defined as:

$$G = H - TS \tag{2.8}$$

When a system moves from one state to another, for example via a phase transition or a chemical reaction, there is a change in the Gibbs energy of the system. Only transitions that represent a negative change in the Gibbs energy can occur. The partial Gibbs energy, i.e. the partial derivative of the Gibbs energy with respect to the number of moles of component a, is the chemical potential of that component:

$$\frac{\partial G}{\partial n_a} = \mu_a \tag{2.9}$$

This expresses how much the Gibbs energy of the system changes by a change in the number of moles of component a. The total, or integral, Gibbs energy of the system is equal to the sum of the chemical potentials of all components. A system of multiple components $a, b, c \ldots$,

and phases $\alpha, \beta, \gamma \ldots$, is in equilibrium if the chemical potential of each component is the same in all phases, that is:

$$\mu_a^\alpha = \mu_a^\beta = \mu_a^\gamma = \ldots \tag{2.10}$$

for all components. A solution represents a homogeneous mixture of a solvent and one or more solutes. The chemical potential of each component is given as

$$\mu_a = \mu_a^0 + RTln(a_a), \tag{2.11}$$

where μ_a^0 represents the chemical potential of component a in some standard state, and a_a is the activity of component a relative to the same standard state. From this relation it is easy to show that the change in Gibbs energy for a system as the result of a chemical reaction is given by the equilibrium constant of that reaction:

$$\Delta G^0 = -RTln(K) \tag{2.12}$$

In the ideal case, the activity of each component is taken as equal to the mole fraction of that component, and the total Gibbs energy of the solution becomes:

$$G_{id} = G^0 + RT(x_a lnx_a + x_b lnx_b + \ldots) \tag{2.13}$$

2.2.2 Deviation from ideality

For non-ideal solutions, the activity of each component is not equal to its mole fraction. The activity coefficient $\gamma_a = a_a/x_a$ is a measure of the deviation from ideality. For a non-ideal solution, by substituting $\gamma_a x_a$ for a_a in equation 2.11 and summing over all components, the expression for the total Gibbs energy becomes:

$$\Delta G = \Delta G_{id} + RT(x_a ln\gamma_a + x_b ln\gamma_b + ...) \tag{2.14}$$

Thus the Gibbs energy can be divided into an ideal term G_{id}, and the deviation from ideality, commonly collected in an excess term G_{ex}. One of the simplest approximations to the excess Gibbs energy term is by approximating the activity coefficients by polynomial expansions. For a solution of a single solute a:

$$ln\gamma_a = \sum_j J_j x_a^j \tag{2.15}$$

Here, the J_j's are known as interaction coefficients. The zeroth order coefficient is the limiting value of the activity coefficient at infinite dilution, represented symbolically by ε_0. The first order coefficient represents how $ln\gamma_a$ changes with variations in x_a. It is therefore known as the self-interaction coefficient and represented symbolically by ε_a^a.

For a solution of several solutes the expansion is done over a multivariate polynomial. For example, for three solutes a, b and c:

$$ln\gamma_a = \sum_i \sum_j \sum_k J_{ijk} x_a^i x_b^j x_c^k \tag{2.16}$$

Commonly, for low concentrations of the solute only the linear terms are included. Again, the low order J's are represented symbolicaly by ε's:

$$ln\gamma_a = \varepsilon_0 + \varepsilon_a^a x_a + \varepsilon_a^b x_b + \varepsilon_a^c x_c \tag{2.17}$$

The first two terms are the same as described above for a one-solute solution. The ε_a^b and ε_a^c terms are known as the a-b and a-c interaction coefficients, and represent how the activity of component a depends on the concentration of component b or c, respectively. Higher order interaction terms are not discussed in the current work.

The interaction coefficients defined above are described using natural logarithms and mole fractions. For some applications, it is more suitable to define the concentrations in m.% and to use the Briggs'

logarithm rather than the natural logarithm. Interaction coefficients defined in this way are commonly represented symbolically with the Latin e to differentiate them from the ε's. There is a simple relationship between the two definitions, here exemplified for the case of an a-b interaction in a solvent s:

$$e_a^b = \frac{M_s}{M_b} \frac{1}{ln(10) \cdot 100\%} \varepsilon_a^b \tag{2.18}$$

M_b and M_s are the molecular weights of the solute b and the solvent s, respectively.

For the definition in natural logarithms and mole fractions, the interaction coefficients can be shown to be equal to their conjugates. This is because ε_a^b can be defined as a partial derivative of the excess Gibbs energy of the ternary system, and becauce the order of partial differentiation of a homogeneous function with respect to two variables does not affect the result:

$$\varepsilon_a^b = \frac{\partial^2 \Delta G/RT}{\partial N_a \partial N_b} = \frac{\partial^2 \Delta G/RT}{\partial N_b \partial N_a} = \varepsilon_b^a \tag{2.19}$$

Under the Briggs' logarithm/m.%-definition, the relation $e_a^b = e_b^a$ does not hold. However, by combining equations 2.18 and 2.19, one finds that

$$e_a^b = \frac{M_a}{M_b} e_b^a \tag{2.20}$$

As seen from the example of interaction coefficients, the choice of standard state is important. Two of the most commonly employed standard states are the Henrian and Raoultian standard states, which are defined from Henry's and Raoult's laws describing the behaviour of dilute solutions. Henry's law states that the activity of a dilute solute is proportional to its mole fraction, while Raoult's law states that in the dilute case, the activity of the solvent is equal to that of the pure substance multiplied by the mole fraction of the solvent.

The Raoultian standard state of a component is defined as the pure component with the same structure as in the solution. In dilute solutions, it makes sense to use the Raoultian standard state for the solvent. More appropriate for the solutes is the Henrian standard state, defined as the hypothetical extrapolation of the Henry's law behaviour at infinite dilution to the pure component. In terms of activity coefficients, the activity coefficient of a component relative to the Raoultian standard state will approach one as its mole fraction approaches unity, whereas in the Henrian case the activity coefficient approaches one as the component approaches infinite dilution, i.e. the mole fraction approaches zero. In other words, in a dilute solution, the solvent shows near-ideal behaviour with a Raoultian standard state, while for the solute, the same is true for the Henrian standard state.

2.2.3 Solubility limit as a function of temperature

The Gibbs energy change of a solute A relative to its pure state is given by:

$$\Delta G = RT\ln(a_A) \tag{2.21}$$

Assuming that the enthalpy and entropy changes ΔH and ΔS are temperature independent, then the familiar relation between Gibbs energy, enthalpy and entropy (Equation 2.8) can be rearranged to obtain:

$$\Delta H = R\frac{\partial(G/T)}{\partial(1/T)} \tag{2.22}$$

which means that:

$$\Delta H = R\frac{\partial \ln(a_A)}{\partial(1/T)}. \tag{2.23}$$

If we assume temperature independence of the activity coefficient γ_A so that $\partial \ln a_A = (1/x_A)\partial x_A$, this rearranges to:

$$\frac{\Delta H}{R}\partial(1/T) = \frac{1}{x}\partial x_A \tag{2.24}$$

Integration along the liquidus from the pure solute with melting point T_m gives

$$\int_{1/T_m}^{1/T} \frac{\Delta H}{R} \partial(1/T^*) = \int_1^x \frac{1}{x} \partial x^* \tag{2.25}$$

It thus follows that

$$\ln x_A = \frac{\Delta H}{R} \left(\frac{1}{T} - \frac{1}{T_m} \right) \tag{2.26}$$

and

$$x_A = \exp\left(\frac{-\Delta H}{R T_m} \right) \cdot \exp\left(\frac{\Delta H}{R T} \right) \tag{2.27}$$

Under the present assumptions, the first exponential function can be collected in a single temperature independent constant, as can the ΔH and R within the second exponential. The solubility limit of a solute as a function of temperature can therefore be described by an Arrhenius equation:

$$x_A = A \cdot \exp\left(\frac{B}{T} \right) \tag{2.28}$$

In the current work, Henry's law behaviour is assumed for the solutes. This implies a non-dependence of the activity coefficient with temperature, and hence an Arrhenius equation is employed in all curve-fittings of solubility data vs. temperature.

2.2.4 Calculation of the dissolution energy

In solution thermodynamics, an important property is the Gibbs energy of dissolution, i.e. the ΔG of the reaction:

$$A(s) \leftrightharpoons \underline{A}(l) \tag{2.29}$$

where A is the solute, and $\underline{\mathrm{A}}(l)$ means liquid A dissolved in the solvent B. This reaction can be difficult to observe directly through experiments. In such cases the solute can be equilibrated with an intermediate solid phase $\mathrm{A}_n\mathrm{B}_m$, and the dissolution reaction be seen as a two-step process. If the equation describing the equilibrium reaction with the intermediate phase is subtracted from the reaction of formation of the intermediate phase from solid A and liquid B, equation 2.29 is the result:

$$\begin{aligned} nA(s) + mB(l) &\leftrightharpoons A_nB_m(s) && (2.30)\\ -\left(n\underline{A}(l) + mB(l) &\leftrightharpoons A_nB_m(s)\right) && (2.31)\\ \hline A(s) &\leftrightharpoons \underline{A}(l) && (2.29) \end{aligned}$$

If the solid phases are virtually pure, so that $a_{A_nB_m}$ and a_B both equal one, the equilibrium constant for equation 2.31 can be written as

$$K_{2.31} = 1/a_A^n \tag{2.32}$$

If in addition the solute A follows Henry's law, so that $\gamma_A = 1$ and $a_A = x_A$, the change in Gibbs energy can be calculated as:

$$\Delta G^0_{2.31} = -RTln(K_{2.31}) = -RTln(1/x_A^n) \tag{2.33}$$

From this consideration it is clear that $\Delta G_{2.29}$ can be calculated as

$$\Delta G_{2.29} = \Delta G_{2.30} - \Delta G_{2.31} = \Delta G_{2.30} + RTln(1/x_A^n) \tag{2.34}$$

Thus, it is possible to obtain information on the Gibbs energy of equation 2.29 through solubility experiments on reaction 2.31.

2.2.5 Derivation of interaction parameters

If multiple solutes are present, solubility investigations can determine the interaction coefficients between them. The solubility level of solute

A will now be a function not only of temperature, but also of the concentration of other solutes, D, E etc.

As justified above, the equilibrium constant describing the dissolution of a virtually pure compound in a virtually pure solvent can be approximated by a negative power of the activity of the solute A, as seen in Equation 2.32. With 1 m.% as the standard state and the activity of A equal to the product of the activity coefficient and the concentration of A, the logarithm of the equilibrium coefficient becomes:

$$log(K) = -log(\gamma_A) - log(C_A) \tag{2.35}$$

where the activity coefficient of A can be expressed using interaction coefficients as:

$$log(\gamma_A) = e_A^A \cdot C_A + e_A^D \cdot C_D + e_A^E \cdot C_E + e_A^F \cdot C_F + ... \tag{2.36}$$

Here, e_A^A, e_A^D etc. are the interaction coefficients describing the A-A, A-D etc. interactions, respectively.

If the activity of A follows Henry's law in the one-solute system, it follows that the A-A interactions are insignificant, and e_A^A is equal to zero. With these assumptions, equation 2.35 can be rearranged to:

$$C_A = \frac{1}{K} \cdot 10^{-\left(\sum_i e_A^i \cdot C_i\right)} \tag{2.37}$$

The sum is over all additional solutes, $i = D, E, F \ldots$ As the solubility must follow a standard Arrhenius dependency on temperature for the one-solute case, the above equation must approach an Arrhenius equation as the amounts of additional solutes approach zero:

$$\frac{1}{K} \cdot 10^{-\left(\sum_i e_A^i \cdot C_i\right)} \xrightarrow[C_i \to 0]{} A \cdot e^{-B/T} \tag{2.38}$$

This means that the first factor in the equation must be equal to the Arrhenius equation describing the one-solute situation.

In order for the Gibbs energy to have a temperature dependence on the form $G = H - TS$, the temperature dependency of the interaction parameter must follow $\varepsilon = \alpha + \beta/T$:

$$G = RT\ln(a) = RT\ln(x) + RT\varepsilon = \underbrace{R\beta}_{H} + \underbrace{[R(\alpha + \ln(x))]}_{-S}T \quad (2.39)$$

Thus the equations describing the solubility will be

$$A \cdot e^{-B/T} \cdot 10^{-[(\alpha+\beta/T)\cdot C_D]} \quad (2.40)$$

for the two-solute case, and

$$A \cdot e^{-B/T} \cdot 10^{-[(\alpha+\beta/T)\cdot C_D + (\gamma+\delta/T)\cdot C_E]} \quad (2.41)$$

for the three-solute case. Fitting experimental solubility data obtained at varying levels of impurity additions and temperatures to these equations, the temperature dependencies of the varying interaction coefficients can be simply read out of the exponents.

2.3 Directional solidification and segregation

The three most important methods of ingot production for silicon wafers are directional solidification of multicrystalline ingots, or the use of Czochralski pulling or float zone techniques for the production of single-crystal-ingots. The current work was undertaken with more of a focus on the multicrystalline process, although the fundamental nature of its results will make them relevant for all processes.

Segregation is a key concept regardless of the solidification technique, although here it will be discussed in the context of directional solidification. For more information on Czochralski and float zone, the reader is referred to a textbook on semiconductor physics, which commonly includes a section on the subject (see for example the already mentioned Streetman and Banerjee [4]; Quirk and Serda [5]; Hummel [6]).

Directional solidification is, as the name implies, a process wherein a liquid is solidified along a single direction. Ideally, all heat flow is through the solid and along the direction of solidification and the liquid-solid interface is planar. To achieve this, the furnace must be designed to have no temperature gradients along any axes other than the one parallel to the direction of solidification, along which it must be monotonous. This could theoretically be achieved through perfect insulation of the edges and top of the furnace, but in practice it is more feasible to control the temperature gradient via the heat sources. The heat is extracted from the bottom of the ingot either through a movement of the ingot relative to the hot zone of the furnace, or by an active cooling at the bottom of the ingot. This will cause most—but not all—of the heat transport to take place through the bottom of the ingot. In real processes there will always be some heat transport through the crucible side walls. This will affect the liquid-solid

interface, which will then not be perfectly planar. If there is a net heat transport into the ingot from the crucible walls, the solid-liquid interface will be slightly convex, and if there is a net outward flow of heat through the crucible walls, the interface will be slightly concave.

Because silicon has a lower density in its solid rather than liquid state, allowing a silicon ingot to solidify without some sort of control would be problematic. Great thermal stresses would be produced by liquid silicon solidifying after being encapsulated by solid material, potentially causing cracks in the ingot and even the crucible. A crucible failure could lead to liquid silicon flowing into the furnace chamber. Even if the ingot did solidify without serious problems, the thermal strains would create a very brittle material ripe with crystal defects, and such a material would be a very poor choice for wafer and solar cell production. In addition to addressing these problems, the main benefits of using directional solidification are twofold: It produces columnar grains, and most impurities will segregate to the top of the ingot.

The grain structure of multicrystalline ingots is very important, since grain boundaries can reduce the performance of the finished solar cells. In the columnar structure produced during directional solidification, grain boundaries run more or less parallel to the growth direction. This means that grain boundaries in wafers cut perpendicular from the ingot will run along the top-bottom direction of the solar cell. This does not only mean that minority carriers are less likely to intersect a grain boundary while migrating towards the pn-junction of the cell, but also that the number of grain boundaries on a specific wafer will be more or less constant throughout the ingot. This last point is of great importance for commercial wafer producers, to whom a small variance in the quality of their product is often more important than an improved maximum performance.

The other major benefit of directional solidification is the segregation of impurities. Because most impurities have a greater solubility

in liquid than in solid silicon, these impurities will not be distributed evenly throughout the ingot but concentrate near the top, leading to a purification in most of the ingot.

An important parameter in the description of impurity segregation is the equilibrium distribution coefficient, k_0. It is defined as the ratio between the concentrations of an impurity in the solid and liquid phases at equilibrium conditions. It is also called the equilibrium segregation coefficient, and is unique to every impurity and material. For example, the segregation coefficient of boron in silicon is defined as:

$$k_0^{Boron} = \frac{C_{solid}^{Boron}}{C_{liquid}^{Boron}} \tag{2.42}$$

This parameter is generally a function of composition, but if the solidus and liquidus are straight lines it will be a constant that is independent of composition. This approximation is generally made for impurities in silicon. Using the equilibrium distribution coefficient, the Scheil equation for the concentration of a certain impurity in the melt can be derived as:

$$C_{liquid}(f) = C_0 \cdot (1 - f)^{k_0 - 1} \tag{2.43}$$

where C_0 is the impurity concentration in the melt at the start of solidification and f is the fraction of the melt that has solidified. From this expression, the impurity profile in the solid can easily be obtained simply by a multiplication by k_0:

$$C_{solid}(f) = k_0 C_0 \cdot (1 - f)^{k_0 - 1} \tag{2.44}$$

These equations are valid when the solid-liquid interface is flat, when there is sufficient mixing in the liquid to maintain uniformity and when the solid-state diffusion is negligible. In real situations, the most erroneous of these is the assumption about complete mixing in the liquid

phase. In reality, there will be a thin boundary layer near the solid-liquid interface in which the concentration of impurities is higher than in the rest of the melt. The equilibrium distribution coefficient will still give the ratio between the solid and liquid concentrations, but it will hold only for this heightened liquid concentration of the boundary layer. It is therefore customary to define an effective distribution coefficient, k_{eff} as the ratio between the concentrations at the interface of the solid phase and in the bulk of the liquid phase. It can be shown that this k_{eff} is tied to k_0 through the following relation as first derived by Burton, Prim and Slichter:

$$k_{eff} = \frac{k_0}{k_0 + (1 - k_0)e^{-v\delta/D}} \tag{2.45}$$

Here δ is the thickness of the boundary layer, D is the diffusion constant in the liquid, and v is the rate of solidification. Thus, k_{eff} depends on the dimensionless group $v\delta/D$ for small values of which it approaches k_0. This means that equilibrium conditions are obtained for the following cases: δ is low, i.e. no boundary layer; v is low, i.e. the solidification is slow enough that complete mixing in the liquid is achieved; or D is large in which case complete mixing will be achieved even for $v > 0$.

For ingots produced under near-equilibrium conditions in standard directional solidification processes, impurities will show a distribution through the ingot given by the Scheil equation with k_{eff} substituted for k_0. Figure 2.8 shows a sketch of the segregation obtained for two impurities with different k_0. For an impurity with a low distribution coefficient, such as most metals, there is a significant refining effect through most of the ingot, with an accumulation near the top. This means that the feedstock material for multicrystalline ingots need not fulfil the same purity demands as the finished wafers. For an impurity with a distribution coefficient $0.1 < k_0 < 1$ such as boron or phosphorous, there is a much less pronounced segregation. It is therefore more

important to control the levels of these kinds of impurities in the feedstock. It should also be noted that a large segregation coefficient is a necessity in dopants, as otherwise the electrical properties of the wafers would vary too much throughout the ingot.

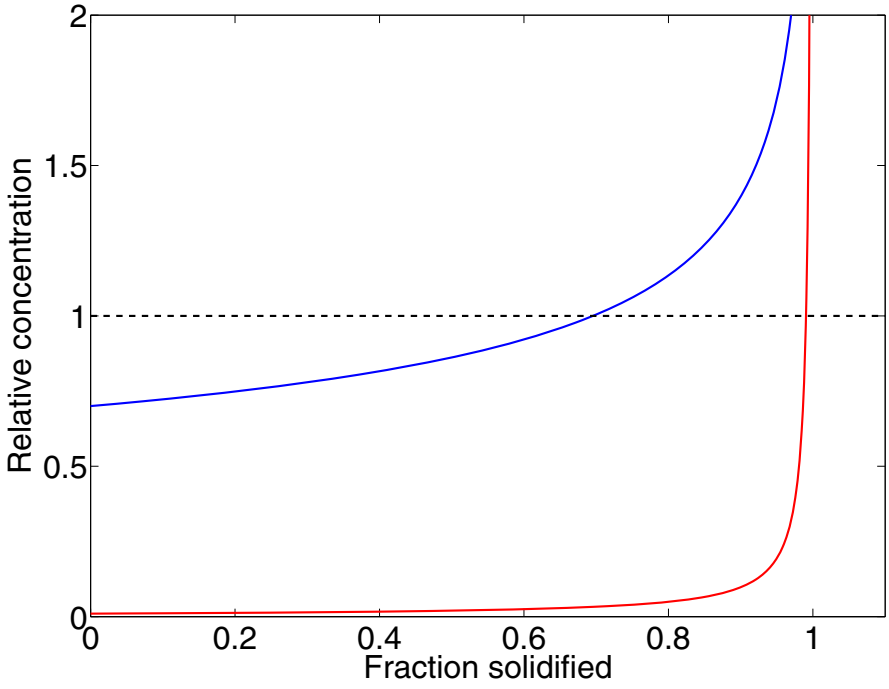

Figure 2.8: Illustration of segregation as described by Scheil's equation. The blue curve shows an impurity with k_0=0.7, while the red curve shows an impurity with k_0=10^{-2}.

Deviations from the Scheil distribution will occur if all of its prerequisites are not fulfilled. Since the solidified silicon ingots are commonly

cooled very slowly, there might be significant solid diffusion. This process is known as back-diffusion, which means that a larger portion of the top of the ingot will have to be scrapped than what is predicted by the Scheil equation. The Scheil equation will also not be fulfilled if the total impurity amount does not remain constant throughout the solidification. This can be the case for impurities entering the melt continuously during the solidification, either via the gas phase or through in-diffusion from the crucible walls.

2.3.1 Segregation during solidification of silicon in a quartz tube

Segregation will come into play in all solidification processes, and may influence how dissolved elements are distributed in the solid. In the present work, quartz tubes are employed to extract samples of liquid silicon. How the solidification of the samples proceeds inside the quartz tubes may influence the homogeneity of the analysed samples.

Three possible segregation mechanisms may come into play: Segregation caused by lateral solidification, segregation caused by vertical segregation, and segregation caused by enrichment and flow of the liquid phase during solidification. These mechanisms are illustrated in figure 2.9, and discussed below.

As heat is transferred through the quartz tube walls, the silicon will start to solidify from the tube walls and inwards, as illustrated in figure 2.9(a). This will create a situation where solutes are expelled into the liquid phase in the center of the tube.

There will also be heat transfer along the length of the tube, meaning that the silicon solidifies from the bottom and the top towards the vertical centre of the sample. This situation is described in figure 2.9(b). Again impurities will be expelled into the molten phase, causing an impurity profile that varies from low at the top and bottom

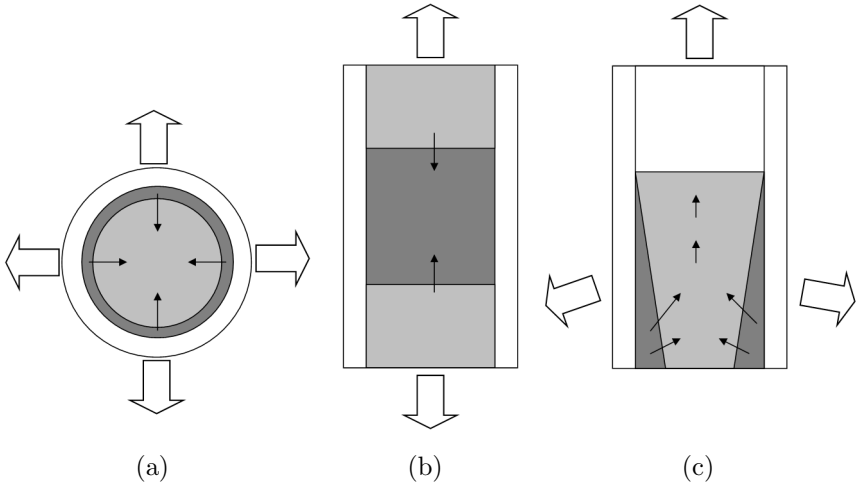

Figure 2.9: Principle sketches of varying segregation effects during solidification in a quartz tube. Light grey symbolises liquid silicon, dark grey is solid silicon, white arrows signify heat flow, and black arrows represent impurity transport. a: Lateral segregation caused by heat transport through the quartz tube walls. b: Vertical segregation caused by vertical heat transport through the silicon. c: Impurity flow in a sample that solidifies during sampling.

of the sample, with a maximum somewhere in between. The location of this maximum will be determined by the relationship between the vertical heat flows in the upwards and downwards directions. If these two heat flows were identical, solidification would proceed with equal speed from the top and the bottom, the central portion of the sample would be the last to solidify, and the impurity concentration would be largest in this area. However in reality, the heat flow upwards—towards the ambient laboratory—will be greater than the heat flow down towards the furnace. This means that solidification will proceed

more rapidly from the top and an impurity maximum could be expected to be located at some point below the vertical centrepoint of the sample.

A third concern is that solidification will start immediately after the sample is sucked into the quartz tube. If this is the case, a situation similar to what is illustrated in Figure 2.9(c) could be the result. Here, silicon will solidify as soon as it comes into contact with the quartz tube, creating a layer of solid silicon through which the rest of the sample flows. In such a case, impurities will be expelled from the solidifying layer into the still flowing liquid, and can be expected to accumulate near the top of the sample.

The real situation is difficult to predict, but is likely a combination of the three mechanisms described. The main point is that the extracted samples can be expected to display a heterogeneous distribution of impurities. The entire sample should therefore be analysed to get an accurate value of the impurity content of the melt.

Chapter 3

Experimental apparatus and procedure

The experimental work in this thesis has been performed in two different furnaces: a pilot-scale induction furnace for directional solidification producing ingots of 10-12 kg, and a small resistance heated tube-furnace that takes charges of approximately 75 g silicon. In this chapter, the two furnaces will be described in detail and the experimental procedures outlined. For simplicity, each furnace will be dealt with in turn, with all details on the apparatus and experimental set-up in the directional solidification furnace being described in this section. A similar summary will then be given for the small tube furnace in the next section, and the final section of this chapter will describe the methods and equipment used for chemical analysis.

3.1 Experimental setup and apparatus in the directional solidification experiments.

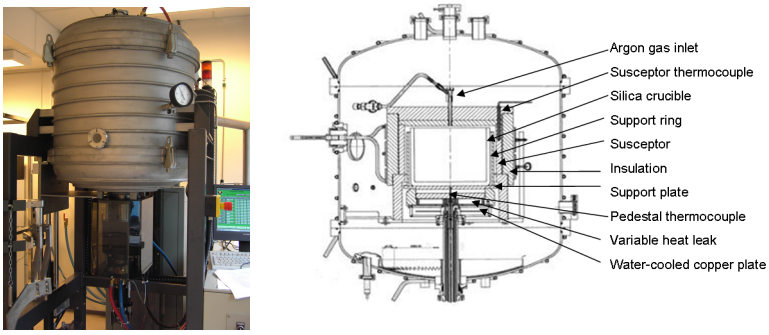

(a) (b)

Figure 3.1: The Crystalox DS 250 furnace. a: Photography of the furnace. b: Technical drawing from [90].

3.1.1 Apparatus

Furnace

The furnace used in the present work is a Crystalox DS 250 pilot scale induction-type furnace, as seen in Figure 3.1. It has been in operation at NTNU since 2001 and takes payloads of up to 12 kg of feedstock. The furnace is designed to achieve directional solidification. The walls and top of the furnace chamber are insulated, while a water-cooled copper plate serves as a heat-sink at the bottom. For ideal conditions,

the heat flux should be constant across the solid-liquid interface which would then be planar. Previous work [91] in the same furnace reports the solid-liquid interface to be slightly convex, with ∼5 mm height variations between the centre of the ingot and a point halfway to the edge.

The top of the furnace has six flanges for access to the furnace interior as illustrated in Figure 3.2. The central one (3) is typically used as an argon gas inlet and another inlet is reserved for a thermocouple.

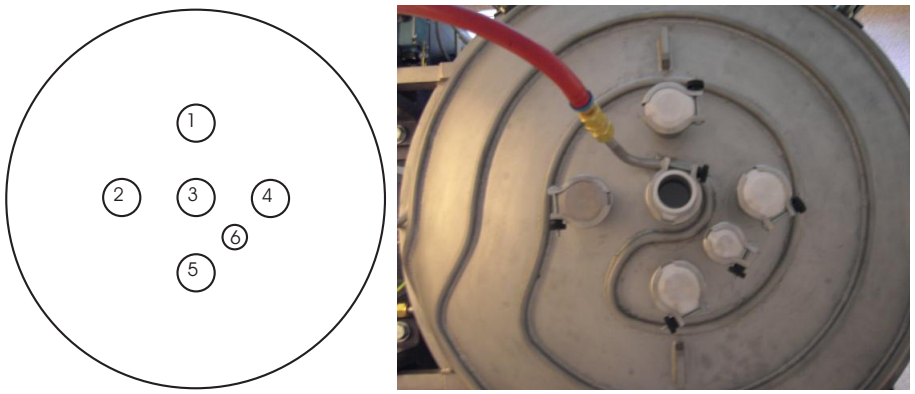

(a) (b)

Figure 3.2: The furnace top. a: Simple sketch showing the positions of the flanges. Flanges 1-5 are QF40, while flange 6 is QF25. b: Photography of the furnace top.

The furnace is computer operated and allows for meticulous programming of the process cycle. The temperature profile at the susceptor can be described in detail: at any time during the process cycle, both the absolute temperature and its gradient will follow a predefined path. The temperature control is maintained by three factors: the susceptor temperature, the crucible position, and a variable heat

leak mechanism. The variable heat leak device consists of two graphite disks located between the bottom of the crucible and the water-cooled copper plate. Both disks have four identical holes, and can be rotated relative to each other. Maximum heat leak is obtained when the holes of the two disks completely overlap, and a 45° rotation from this position will result in complete shutting. In the current work the crucible position is constant during each run, so the temperature is controlled by the susceptor and the heat leak.

Sample taking method and equipment

Quartz tubes with an inner diameter of 4 mm and a syringe were used to extract the samples. Ideally, one of the furnace flanges should have been fitted with a device which allowed the extraction and cooling of samples without disturbing the furnace atmosphere (Similar to what was used in the small tube furnace, see section 3.2.1). However, an elaborate set up was not feasible due to space restrictions in the laboratory.

The distance from the top of the flange to the bottom of the crucible is 615 mm, while the distance from the same flange to the ceiling of the laboratory is 910 mm. Since it must be possible to handle and retract the sampling tubes at all times, the sampling tubes should be able to extend at least ∼3 cm above the sealing mechanism when sampling from the bottom of the crucible. Taking this into consideration, the total height of any equipment mounted on top of the furnace could not extend 130 mm or the sampling tubes would not fit below the ceiling. With no cooling section possible, the challenge became one of limiting the leak, as any seal formed by an o-ring on the silica tube would be destroyed by the heat from the molten silicon burning the o-ring.

The set-up decided upon is described in Figure 3.3. A Q40 flange is threaded into a 3/4" ball valve, on top of which is the 'sealing

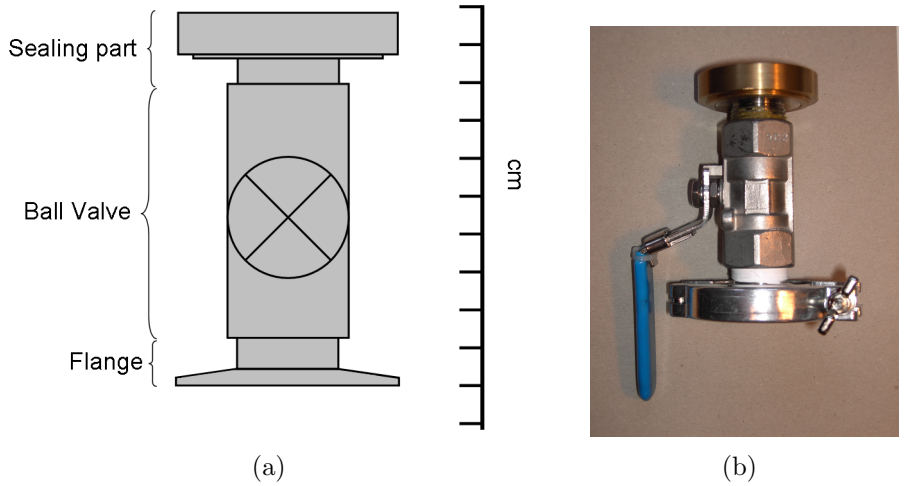

(a) (b)

Figure 3.3: a) Principal sketch of the sealing mechanism: A ball valve with a Q40 flange and sealing part threaded into it. The sealing part is described in figure 3.4. b) Photograph of the sealing mechanism.

part' detailed in Figure 3.4. The total height of this setup is 105 mm. When no samples are being taken, the seal is maintained by the ball valve[1]. During sample taking the seal is maintained by an o-ring sealing against the silica tube. When the sample is extracted past the o-ring it will burn and the seal is destroyed. Below the o-ring some graphite wool is packed against the silica tube to limit the leak.

The distance between the top of the valve and the o-ring seal is only about 4 cm, so careful operation of the ball valve is important so that it is closed as soon as the bottom of the silica tube is clear of the

[1] A leak test performed on the sealing setup determined the leak to be less than $6 \cdot 10^{-6}$ mBar l/s when the valve is closed [92].

valve, but before it clears the o-ring seal.

Because no cooling section was possible in these experiments, the silicon sample had to be pulled through the seal while hot, and leakage became an inevitability. The chosen setup is seen as the best way of limiting the leak when a complete avoidance was not possible. As a further measure, the furnace is operated at excess pressure, so that any gas flow will be of Ar-gas out of the furnace, and not of air into the furnace.

Crucibles and coating

The crucibles used were electronic grade SiO_2 crucibles, 25 cm in diameter and 15 cm in height with a curved bottom. The wall thickness of the crucible is approximately 5 mm.

If the SiO_2 crucible is in direct contact with liquid silicon for extended periods of time, the melt can fuse with the wall as it solidifies, a process known as sticking. In the worst case scenario, this can lead to crucible failure and leakage of silicon into the furnace chamber. It will also induce thermal tension in the ingot as it contracts on solidification, which can cause the ingot to crack. In addition, a direct contact between the silicon melt and the SiO_2 will of course also lead to increased oxygen content in the silicon.

To remedy this problem, the inside of the crucibles are coated with a Si_3N_4 coating. This coating is prepared from Si_3N_4-powder, deionised water and a binder: Optapix PAF 2. In the present work the coating is applied manually using a spray gun on a crucible heated to 100 °C. The hot crucible walls significantly speed up the dehydration of the coating and thus prevent dripping. The coating procedure is operator-sensitive, which is why it has been automated in industry. After the application of the coating, it is sintered in a 12-hr. cycle that reaches temperatures of 1100 °C.

3.1.2 Experimental procedure

The coated crucible is placed inside the graphite susceptor—which has been removed from the furnace—and then stacked with silicon. Care must be exercised during the stacking process to make sure that no sharp edges scratch the coating. It is also important, at least for 12 kg castings, that the feedstock has a good size distribution in order to get a sufficient amount inside the crucible. This is of less concern with 10 kg castings.

The charged crucible and the susceptor are then placed inside the furnace, and the furnace program is started. The furnace program has several different segments of varying length. It is possible to manually enter the next segment prematurely and this is sometimes planned for, e.g. to ensure that the solidification process is not started in the middle of the night.

As the program cycle starts, the furnace evacuates to 0.08 mbar and then heats the susceptor to 900 °C at a rate of 200 °C/hr. During this heating period, any volatile species on the feedstock surface will evaporate and be removed from the furnace. Once at 900 °C, the furnace is filled with argon to 1 atm. From this point, there is a continuous flow of argon through the furnace. Next, the furnace is heated until the susceptor temperature is 1535 °C, and the melting starts. The completion of the melting can be detected by an increase in the pedestal temperature. The transition to the next segment can thus be set to be automatically triggered, or can be triggered manually if a holding period (e.g. for sample taking before solidification) is desired. In the next segment the temperature is lowered slowly, and the silicon starts to solidify from the bottom of the crucible.

The completion of the solidification is detected by a spike in the power output as the furnace compensates for the interruption of the release of heat of fusion from the solidifying silicon. After complete solidification, the temperature is reduced slowly and normally given

a one hour annealing at 1100 °C. The complete program cycle lasts approximately 40 hrs. A typical temperature profile is seen in Figure 3.5.

In the present work, two different castings have been performed in the directional solidification furnace. During the solidification process of the second experiment, samples were extracted by use of the set-up described above. The quartz tube was rapidly fed into the furnace and into the melt, and liquid silicon extracted by use of the syringe. The extraction of one sample typically took about a minute or less, and samples were extracted 1-2 times per hour throughout the solidification process. In addition, samples were cut from the finished ingots in both experiments. The details of the experiments are summarised in Table 3.1.

Table 3.1: Overview over experiments performed in the Crystalox furnace.

Experiment	Samples analysed	
	Solid	Liquid
DS-Si-B-1	8	-
DS-Si-B-2	2x6	12

Feedstock

The feedstock used were upgraded metallurgical grade silicon provided by Elkem Solar from their pilot scale production. It had a boron content of approximately 0.5 ppmm and a phosphorous content of approximately 1.0 ppmm. The content of metallic impurities was given as being below the detection limits. The feedstock used in the two castings came from different lots.

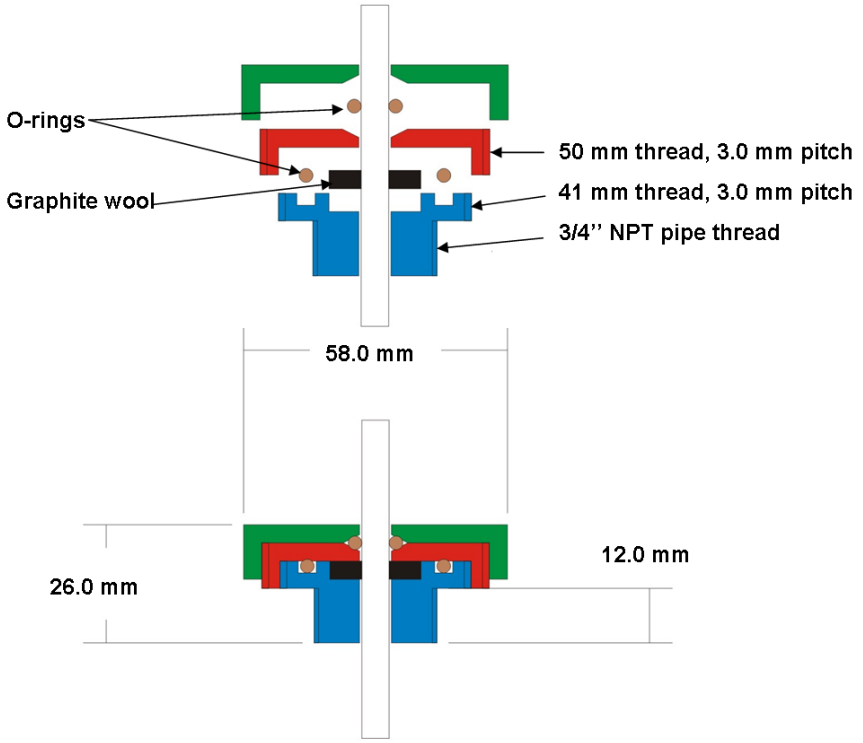

Figure 3.4: The sealing part. An o-ring provides the principal seal against the silica tube, while graphite wool will limit the leak when the o-ring fails due to extensive heat. Drawing by S. Gaal [92].

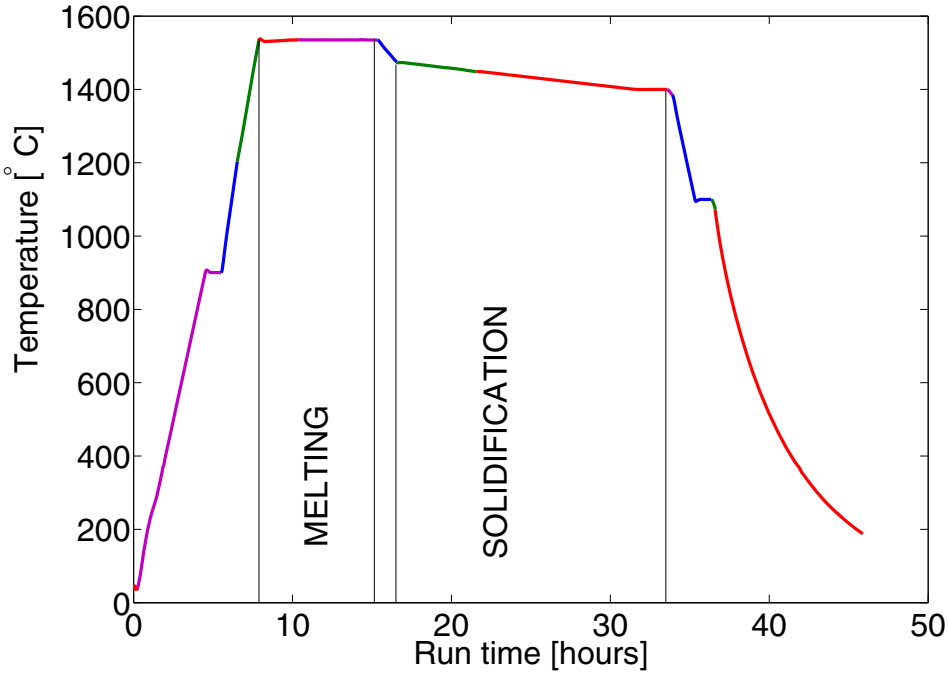

Figure 3.5: Typical temperature profile in the Crystalox DS 250 pilot scale furnace. The changing colours of the graph indicates the different program segments. The regions in which melting and solidification takes place are indicated.

3.2 Experimental set-up and apparatus in the tube furnace experiments.

3.2.1 The tube furnace apparatus

Furnace

The furnace used is a resistance heated tube furnace. The furnace chamber consists of a 50 mm $\varnothing_{\text{int}}$ x 60 mm $\varnothing_{\text{ext}}$ x 630 mm dense alumina tube closed with water cooled brass plates at the top and the bottom. Around this is a 200 mm long $MoSi_2$ resistance coil of inner diameter 76 mm ("Superthal" from Kanthal AB Hallstahammar, Sweden). The heating spiral is insulated by an 80 mm $\varnothing_{\text{int}}$ x 290 mm $\varnothing_{\text{ext}}$ x 350 mm cylinder of porous alumina, outside of which is a water cooled shell of brass and aluminium. The heating element has a recommended maximum operating temperature of 1550° C, but has previously been used continuously at 1660 °C without problems [93]. In the present work, the goal was to investigate the temperature range from the melting point of silicon and ∼100 °C upwards. Consequently, there was no need to exceed the recommended operating maximum temperature. A sketch of the furnace and its interior can be seen in Figure 3.7.

Temperature control and measurement

The furnace is controlled by a Eurotherm 903P temperature controller connected to a type S Pt-Pt10%Rh thermocouple placed near the hottest point on the heating spiral. The temperature in the melt is measured by a second type S Pt-Pt10%Rh thermocouple in a 3 mm twin bore tube, resting inside a 5 mm alumina sheath. The positions of the two thermocouples are indicated in Figure 3.7. All temperature measurements in this thesis refer to the melt temperature. The fur-

nace can be given a set point temperature or the output power can be adjusted manually.

The temperature gradient, shown in Figure 3.6, was measured by taking temperature readings at different heights above the crucible bottom throughout the melt and furnace atmosphere. A different equation was used for the fitting of the temperature data above and below the melt interface, marked with a dotted line in Figure 3.6. As can be seen, there is approximately a 6 °C variation in temperature throughout the melt. The melt temperatures in the current work were measured at the crucible bottom.

Furnace interior

The crucible support is an 8 mm $\varnothing_{\text{int}}$ x 12 mm $\varnothing_{\text{ext}}$ x 300 mm alumina tube, onto the end of which is cast a 44 mm $\varnothing$ x 20 mm disk of alumina cement. Below the crucible support is a series of radiation shields, 48 mm $\varnothing$ disks with a 24 mm $\varnothing$ hole in the center. Around the crucible support tube is another 20 mm $\varnothing_{\text{int}}$ x 26 mm $\varnothing_{\text{ext}}$ alumina tube, on top of which rests the bottommost of these radiation shields. On top of this is a 20 mm section of 20 mm $\varnothing_{\text{int}}$ x 26 mm $\varnothing_{\text{ext}}$ alumina tube and on top of this is the second radiation shield. The subsequent shields are interspaced with 20 mm sections of alumina tubes. In the current work, three radiation shields were used below the crucible. In addition, from the top of the furnace tube a series of five 48 mm $\varnothing$ radiation shields are suspended from two thin alumina tubes. These shields are spaced by small segments of 4 mm $\varnothing_{\text{ext}}$ alumina tubes of varying length threaded onto the thinner tubes. The spacing between radiation shields can be adjusted by changing the number of alumina tube segments between two radiation shields. In the present work, the spacing has been approximately 1 cm. The shields have two 8 mm and 11 mm diameter holes designed to align with the inlets in the top flange (see below), to allow thermocouples and sample tubes access

to the crucible interior. The radiation shields also reduce convection, and hence, improve insulation and reduce the thermal gradient in the furnace chamber.

Gas system

In the present work, the furnace has been run under one of three atmospheric conditions: Near vacuum, flowing gas at close to ambient pressure, or gas atmosphere at slightly above ambient pressures. The composition of the atmosphere has been either 100% argon or 100% nitrogen.

To achieve vacuum, the furnace is connected to a standard double stage vacuum pump. It has a capacity of 3 m^3/h at $1.0{\cdot}10^{-3}$ mbar, and is capable of maintaining a vacuum of $< 1.0 \cdot 10^{-4}$ mbar.

Argon or nitrogen is supplied from a gas flask via a series of pressure reducing valves and a PVC tube attached to the top flange. The gas outlet valve is located at the bottom of the furnace which means that gas will be flowing through the furnace, so any evolving gases should be quickly removed from the system. The gas is released through double bubble flasks; the first is empty, the other is water filled. The bubble flasks facilitates observation of gas flow, and the addition of the empty flask reduces the likelihood of back-suction of water into the furnace. The presence of the bubble flask also means that the pressure in the furnace chamber will be a few mbar above the atmospheric pressure.

The purity of the gases used was 4N. This was found to be adequate, as no SiO_2 precipitates were observed in the current work.

When the furnace is operated in vacuum, the vacuum pump is on, the vacuum valve is open, the gas inflow valves are closed and the gas outlet valve is closed. In these conditions, the manometer displays its minimum reading.

When operated in gas flow with pressure close to the atmospheric pressure, the vacuum pump is off, the vacuum valve is closed, and the

gas outlet valve is completely open. The valves on the inflow-side of the gas system are adjusted so that there is a gentle bubbling in the bubble flasks. In these conditions, the vacuum gauge fluctuates with a ∼1 mbar amplitude around a pressure slightly (∼1 mbar) above the laboratory ambient pressure.

The final mode of operation is gas flow at higher than ambient pressure, used in connection with sampling. This is achieved by partly closing the gas outlet valve for a short period of time to allow pressure to build up inside the furnace. Then the inlet and outlet valves are tuned until the inflow and outflow of gas are equal and the pressure is constant. Typically, the chamber pressure is kept at 30-50 mbar above the ambient laboratory pressure during sampling. This causes any leakage during sampling to be of gas flowing out rather than in. After sampling, the gas outlet valve is reopened, and the furnace atmosphere is restored to ambient pressure.

Sample taking equipment

The top flange of the furnace has four inlets, two of which are designed for gas. In the present work, one of these inlets has been sealed off, while the other is used for gas flow into the furnace as described above. Of the other two inlets, one is used for a thermocouple while the final inlet is used for sample taking. It is fitted with a ball valve, a 115 mm steel tube and a sealing mechanism with two o-rings.

2 mm $\varnothing_{\text{int}}$ x 4 mm $\varnothing_{\text{ext}}$ quartz tubes were employed for the extraction of liquid samples. A syringe was connected to the top of the quartz tube with a short length of silicone tube. If about 0.5 mL (∼1 g) of melt is sucked into the tube, this corresponds to approximately 137 mm of the tube being filled with silicon, while the total internal distance between the ball valve and the bottom o-ring is 155 mm. Thus, the valve can be closed under the quartz tube after sampling with the hot silicon cooling inside the metal tube still below the bot-

tom o-ring. This means that the o-rings are not damaged by heat from the silicon, and that the atmosphere of the furnace is preserved if the sample size is limited to about 0.5 mL (∼1 g). The o-ring sealing mechanism can be unscrewed and removed from the furnace whilst still attached to the quartz tube, allowing the portion of the quartz tube containing the hot silicon to be cut off underneath the sealing mechanism. In this manner, the silicon never has to pass through the o-rings. The quartz tube can be reused until it is too short to reach down to the melt surface (approx. 650 mm). Figure 3.8 shows a sketch of the sample taking inlet illustrating the mechanisms just outlined.

Crucibles

High purity graphite or Si_3N_4 were chosen as crucible materials. In this way the crucibles themselves would act as the carbon/nitrogen source. A crucible of a different material would necessitate the introduction of carbon or nitrogen from a different source, e.g. a SiC slab. In addition, a crucible of a different material would introduce other impurities to the melt besides carbon or nitrogen. By choosing high purity materials, this concern is further reduced. The crucibles also need to have high density in order to reduce the penetration of silicon into the crucible.

Reaction bonded silicon nitride crucibles were chosen for the nitrogen experiments. These crucibles were produced at Morgan Ceramics, and typically contained 75 % α-Si_3N_4 and 25 % β-Si_3N_4 [94].

High purity, high density graphite crucibles were chosen for the carbon experiments. The crucibles used in the present work are produced at Tanso AB, Sweden, from their IG-610 material. The penetration depth of silicon in this material was measured to 1229 μm by Ciftja [95].

The crucibles have external measurements 44 mm ⌀ x 95 mm and internal measurements 38 ⌀ x 90 mm, i.e. they have a 3 mm wall thick-

ness and a 5 mm bottom. The relatively large height of the crucibles was chosen because of wetting problems experienced in preliminary experiments in graphite crucibles. It also allows for sufficient amounts of silicon to be loaded with less concern about stacking.

Feedstock

The feedstock material was high purity polycrystalline silicon from REC. Two samples were analysed in three parallels in order to establish the carbon and nitrogen content. An average value of 9 $\pm$3 ppmm carbon was found. For nitrogen, of the six parallels, three showed a nitrogen content less than the detection limit of 2 ppmm, while the remaining three showed 2 ppmm.

The boron used was Alfa Aesar boron powder, crystalline, 99.9%, product number 44257. The manufacturer did not have any information about the composition of the remaining 0.1% of their product, so it too was analysed for carbon and nitrogen content. An analysis of five parallels showed a carbon content of 290 ppmm with a standard deviation of 30 ppmm and a nitrogen content of 42 ppm with a standard deviation of 8 ppmm. Assuming a worst case scenario, an addition of 2 wt% boron powder to the feedstock would equal an addition of 6.4 ppmm carbon and 1 ppmm nitrogen.

3.2.2 Experimental procedure in the tube furnace experiments.

Overview of experiments

The experiments can be categorised by the elements present in the melt. In the Si-C and Si-N experiments, pure silicon was melted in a graphite or nitride crucible with no further additions. In the Si-C-N experiments, a slab of graphite was placed leaning against the wall

inside a Si_3N_4 crucible before silicon was added, while in the Si-B-C and Si-B-N experiments, crystalline boron was added to the graphite or nitride crucible before charging the silicon. Table 3.2 shows an overview of all experiments.

Experimental method

In each experiment, a fresh crucible was charged with approximately 75 g of high purity polycrystalline silicon feedstock and loaded into the furnace. In the Si-B-C and Si-B-N experiments, 0.10-2.00 wt% crystalline boron was added to the crucibles before loading the silicon.

The furnace was then evacuated and gradually heated to 1000 °C in vacuum over a period of approximately 150 min. Once the temperature reached 1000 °C, the valve to the vacuum pump was shut, and the furnace filled with either 100 % Ar or 100 %N_2 to ambient pressure. Once ambient pressure was established, the gas was allowed to flow continuously through the furnace, and the bubble flasks were used to monitor the gas flow. Typically, a slow gas flow was employed with bubbles gently trickling out of the bubble flasks.

Next, the temperature was gradually taken to 1414 °C over a period of approximately 120 min and the silicon melted. For the experiments with boron additions, a holding period of four hours was included after the silicon was melted in order to facilitate boron dissolution. At this point the set point function of the temperature control was employed, and the temperature was taken to the point at which samples were to be taken and kept there.

It was assumed that once the silicon was melted, it would react with the crucible and an equilibrium be established. In the case of graphite, the molten silicon would react with the graphite and form a layer of silicon carbide on the internal walls of the crucible:

$$Si(l) + C(s) \rightarrow SiC(s) \tag{3.1}$$

A microprobe analysis of a used crucible was performed to confirm that SiC was formed. Figure 3.10 shows the crucible wall and the solidified silicon after a finished experiment. Three distinct phases can readily be identified, and the x-ray analysis confirmed that the brightest phase was silicon, the darkest phase was graphite, and that the third phase—formed on the interface between silicon and graphite—was silicon carbide. For the nitride crucibles, the equilibrium would be between nitrogen in the form of silicon nitride, and nitrogen in solution:

$$Si_3N_4(s) \rightleftharpoons 3Si(l) + 4\underline{N}(l) \tag{3.2}$$

In addition to this reaction, one needs to consider the reaction across the gas-liquid-interface. Dissolved nitrogen atoms have the opportunity to form nitrogen gas and leave the melt through the gas phase:

$$2\underline{N}(l) \rightleftharpoons N_2(g) \tag{3.3}$$

High partial pressures of N_2 would drive this reaction towards the left, while low N_2 pressures would drive it towards the right. In order to investigate the influence of the gas phase, two of the Si-N experiments were performed in a 100 % argon atmosphere, while three were performed in 100 % N_2. For carbon, the gas-phase should not have an influence on the experiments.

The time required for the establishment of equilibrium at a specific temperature is an important factor in the discussion of the results. Specifically, it is necessary to know whether the samples are extracted at a time when the carbon or nitrogen levels in the liquid are still increasing, or if the solubility limit has been reached. For each sample the settlement time, t_s, is defined as the time elapsed between attained sampling temperature and extraction of the sample. The settlement time was recorded for all samples so that any time-dependence of the carbon or nitrogen content could be investigated.

In each sampling, a quartz tube was fed into the furnace, down through the holes in the radiation shields and into the melt. Then

0.2-1.0 g of liquid silicon was sucked up by use of the syringe and the tube extracted. As explained in the previous section, care was taken to avoid breakage of the seal and to preserve the furnace atmosphere.

When samples were extracted at different temperatures during one experimental run, the samples were always taken in order of increasing temperature. This was done to avoid nitrogen and carbon going into solution at high temperature and then precipitating as Si_3N_4 or SiC once the temperature decreases. As demonstrated by a single sampling performed during cooldown of experiment Si-C-N-4 (see section 4.2.4), such precipitates lead to too high levels during analysis.

A typical temperature profile for an experiment with no boron additions is shown in Figure 3.9.

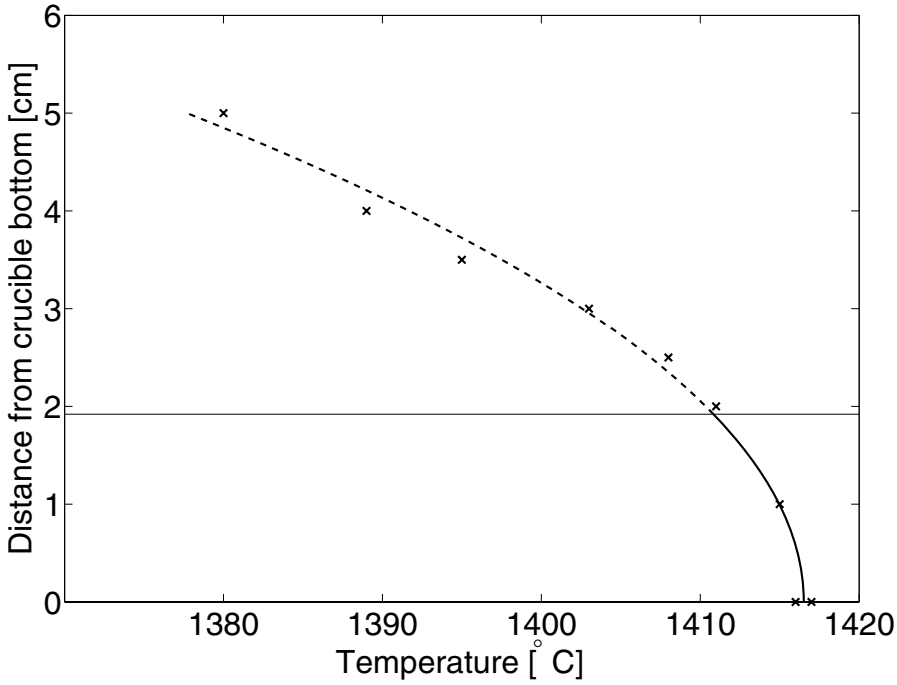

Figure 3.6: Temperature gradient in the tube furnace. A different expression was used to model the temperature above and below the melt surface, as indicated by the horizontal line.

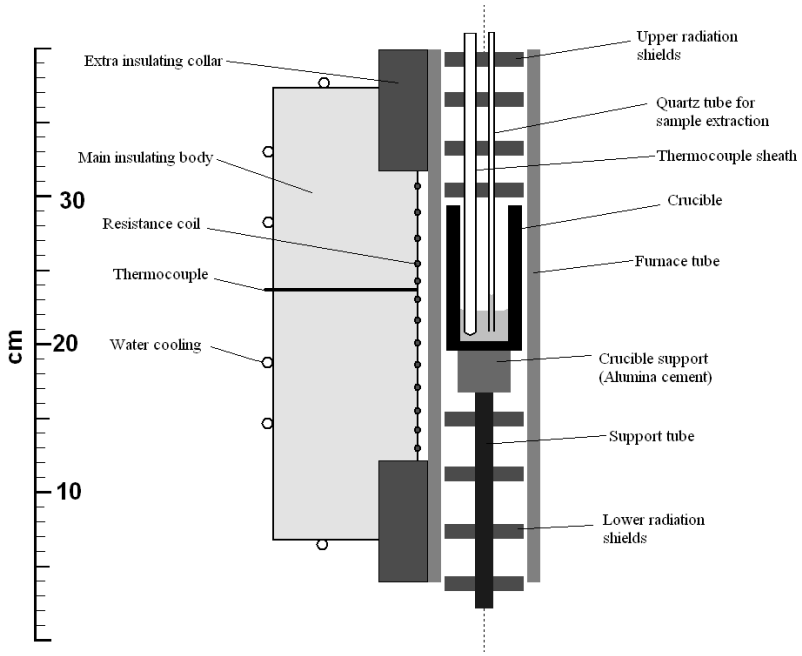

Figure 3.7: Sketch of the interior of the tube furnace. The insulation and water cooling have been excluded on the right hand side of the figure.

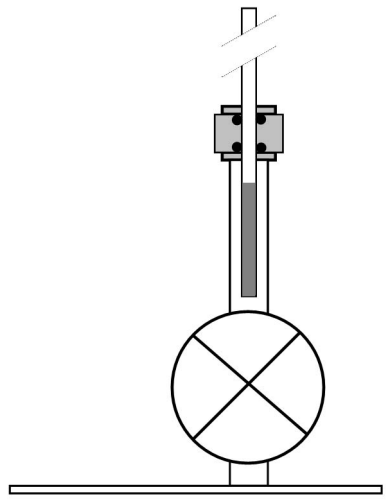

Figure 3.8: The sample taking apparatus. The sketch shows the situation just after sampling is finished, with the ball valve closed beneath the cooling silicon and all silicon beneath the bottom O-ring.

Table 3.2: Overview of experiments performed in the tube furnace.

Experiment	Crucible	Boron addition	Atmosphere	Graphite slab	Samples analysed
Si-C-1	Graphite	-	Ar	-	14
Si-C-2	Graphite	-	Ar	-	9
Si-C-3	Graphite	-	Ar	-	6
Si-C-4	Graphite	-	Ar	-	10
Si-C-5	Graphite	-	Ar	-	5
Si-N-1	Si_3N_4	-	Ar	-	13
Si-N-2	Si_3N_4	-	N_2	-	15
Si-N-3	Si_3N_4	-	Ar	-	12
Si-N-4	Si_3N_4	-	N_2	-	7
Si-N-5	Si_3N_4	-	N_2	-	21
Si-B-C-1	Graphite	0.25 wt%	Ar	-	21
Si-B-C-2	Graphite	0.50 wt%	Ar	-	12
Si-B-C-3	Graphite	1.00 wt%	Ar	-	12
Si-B-C-4	Graphite	1.50 wt%	Ar	-	15
Si-B-C-5	Graphite	2.00 wt%	Ar	-	7
Si-B-C-6	Graphite	0.25 wt%	Ar	-	6
Si-B-C-7	Graphite	0.50 wt%	Ar	-	6
Si-B-N-1	Si_3N_4	0.10 wt%	Ar	-	8
Si-B-N-2	Si_3N_4	1.50 wt%	Ar	-	8
Si-C-N-1	Si_3N_4	-	Ar	Yes	6
Si-C-N-2	Si_3N_4	-	Ar	Yes	6
Si-C-N-3	Si_3N_4	-	Ar	Yes	4
Si-C-N-4	Si_3N_4	-	Ar	Yes	6
Si-C-N-5	Si_3N_4	-	Ar	Yes	6
Si-C-N-6	Si_3N_4	-	Ar	Yes	6

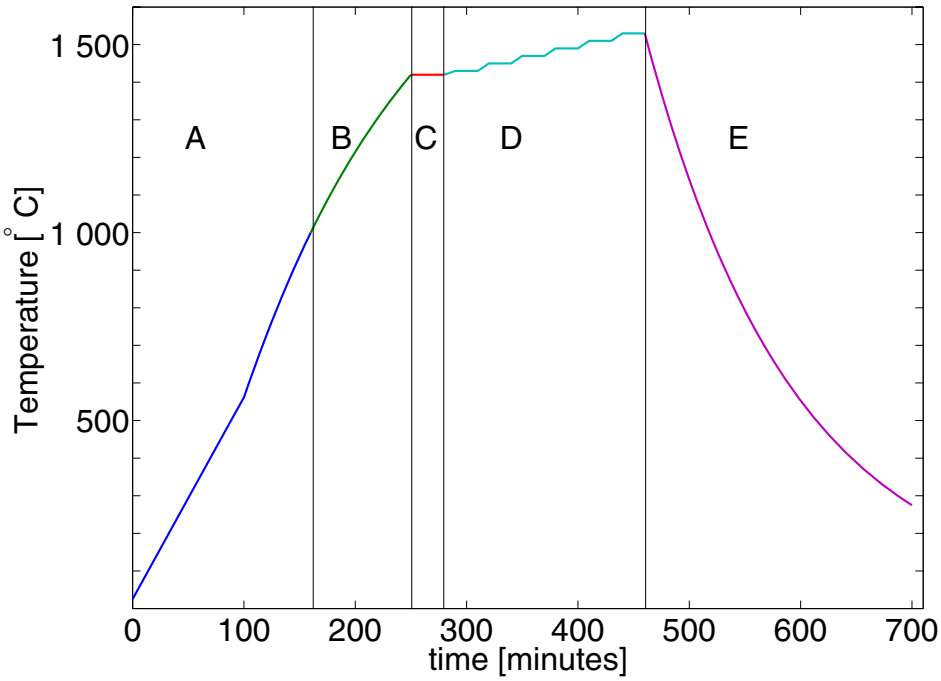

Figure 3.9: Typical temperature profile for an experiment in the tube furnace with no boron additions. The letters indicate the different segments of the experiment. A: Heating in vacuum. B: Heating in Ar/N_2 atmosphere. C: Melting of Si. D: Sample taking. E: Cooldown. For experiments with boron additions, an additional segment of 240 minutes at 1420 °C is included between C and D.

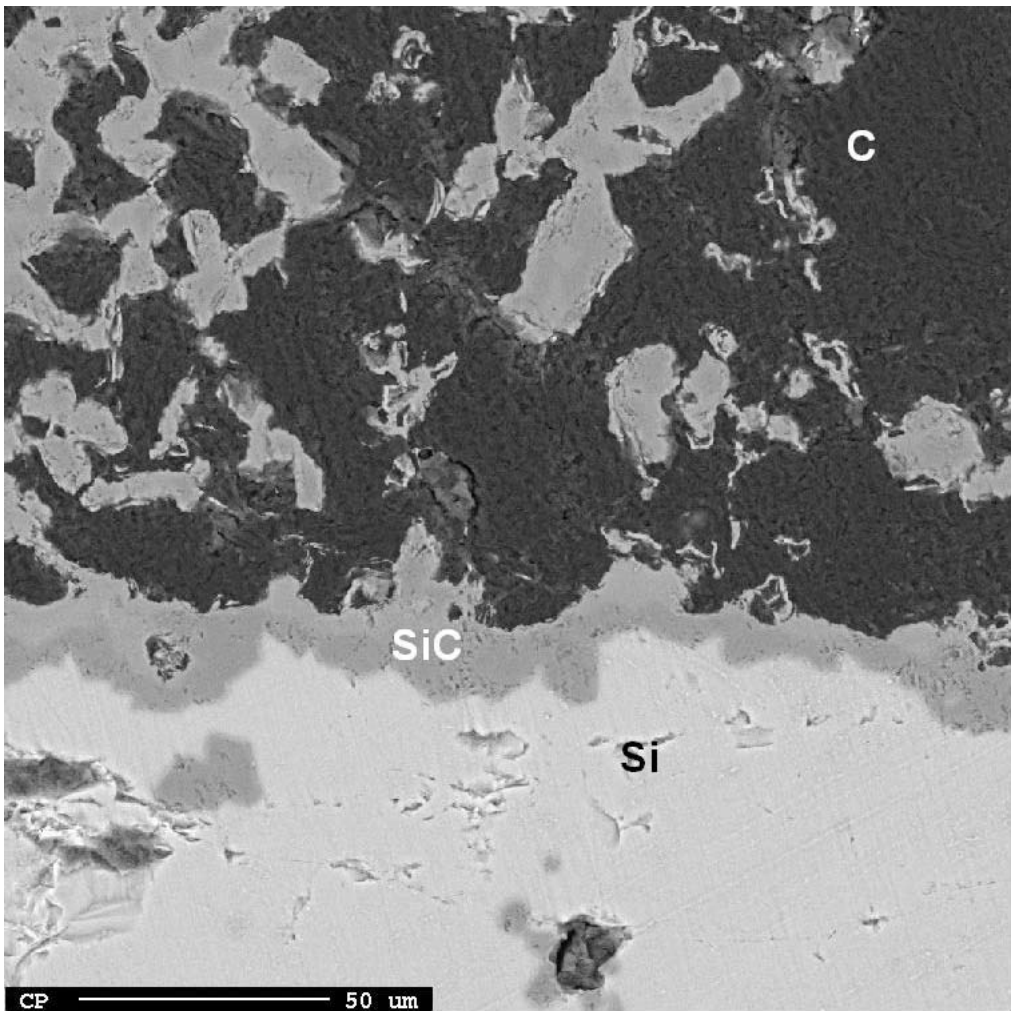

Figure 3.10: Microprobe image of the crucible-silicon interface after a finished experiment. The silicon and graphite are easily identified as the brightest and darkest phases, while the intermediate phase is SiC.

3.3 Sample preparation and analysis

3.3.1 Preparation of extracted liquid samples

Samples from both the small and large scale furnace were etched in concentrated HF for a couple of days in order to completely get rid of the quartz tubes. The silicon was then rinsed in distilled water and sent to analysis.

In order to verify that no carbides or nitrides precipitated on the quartz-silicon interface and were lost in the etching process, two samples each from Si-C-2 and Si-N-1 were investigated by use of microprobe. One sample from each experiment was investigated with the quartz tube intact, and no particles were found on the quartz-silicon interface. The other samples were investigated after etching had taken place, and the sample surface could not be seen to have been affected by the etching in any way. The images can be seen in figure 3.11.

3.3.2 Preparation of samples from the directionally solidified ingots

Samples were cut from the directionally solidified ingots using a saw. For GDMS and Leco analysis, ∼3 cm x 3 cm square columns were cut running the height of the ingot. These were then sliced into ∼1 cm thick segments. The remaining height of the column was measured before each cut in order to more correctly gauge the correct distance from the bottom of the ingot to each sample surface. The samples were ground with SiC paper in order to remove any residue introduced by the saw. This is more of a concern for the Leco-samples than for the GDMS samples because of the pre-sputtering of the GDMS (see below). Thus, the samples for Leco were thoroughly ground on all sides with 80 and 320 grit SiC-paper, while the GDMS samples were given a quick polish with 320 grit paper. Figure 3.12 illustrates how

an ingot can be cut to prepare a series of samples for GDMS or Leco.

3.3.3 Mass spectrometric analyses

Glow discharge mass spectroscopy

The boron analyses of the solid samples from the direct solidification experiments were performed using glow discharge mass spectroscopy (GDMS). Glow discharge is the name of a plasma created by the passing of an electric current through a noble gas. In GDMS, this plasma is used to ionise the sample. The sample chamber is filled with argon at low pressure, and an electric field is set up between the sample—acting as a cathode—and an anode. The potential difference between the anode and the sample ionises the argon atoms and accelerates them onto the sample, where they dislodge atoms from the sample surface. These atoms are ionised by the argon plasma and can then pass through a hole in the anode. As in all mass spectrometers, the ions are then accelerated through electric and magnetic fields, where their paths are determined by their mass to charge ratio. Since the elements are classified based on their mass to charge ratio, it is possible to confound the relevant elements with other ions. This can be remedied by scanning for other isotopes of the relevant elements which will have a different charge-mass ratio.

The GDMS at NTNU is a Finnigan ELEMENT GD manufactured by the Thermo Electron Corporation. Its detection limits for some impurities is in the ppb range. Before an analysis is begun, a 10 minute pre-sputtering is performed at a rate of 20 nm/s, meaning that 12 μm is removed from the sample surface and any surface contaminants are gotten rid off. It is possible to perform several analyses during one run by including a short sputter period between each analysis.

Inductively coupled plasma mass spectrometry

Another mass spectrometric method that was employed in the current work was inductively coupled plasma mass spectrometry (ICP-MS). The method is principaly the same, the difference lies in how the sample is ionised. In ICP-MS this is done by a torch of inducively coupled plasma, into which the sample is introduced in liquid form. Since the sample needs to be in liquid form, it needs to be dissolved in a suitable medium. The analysis is therefore destructive. Furthermore, an analysis at a specific surface of the sample, like in GDMS, is not possible. In the present work ICPMS was used to analyse several samples for boron content: The liquid samples from DS-Si-B-2; the solid samples from the same experiment analysed at Elkem; and the liquid samples from Si-B-N-1 and Si-B-N-2.

A related experimental method, inductively coupled plasma optical emission spectrometry (ICP-OES), was used for the analysis of phosphorous in the samples from DS-Si-B-2 analysed at Elkem. The sample is ionised in the same manner as ICP-MS, but rather than measuring the ions directly, it is the wavelengths of the photons created by the recombination of ions and electrons within the plasma that are measured.

3.3.4 Infrared spectroscopy-analyses

Infrared spectroscopy analyses are a class of analysing techniques that takes advantage of the fact that electromagnetic radiation in the infrared spectrum is absorbed differently by different atomic bonds. This is caused by the different vibrational and rotational oscillations exhibited by the bonds which will absorb IR-radiation with a corresponding frequency. Thus a certain molecule will have a fingerprint absorption spectrum, with absorption peaks associated with the varying vibrational and rotational modes of its different molecular bonds.

Leco

Several methods of analysis were considered for the determination of carbon and nitrogen levels. It is known that Elkem Research has had much experience in analysing high purity silicon for both carbon and nitrogen in connection with the activities at Elkem Solar. To have the samples sent away for analysis in their laboratories was therefore an attractive proposition that was leapt upon when the opportunity arose.

Elkem Research use Leco instruments for the analysis of carbon and nitrogen in silicon. Leco is a trademark of the Leco Corporation, and is used as the name for an entire range of different instruments. Nonetheless, it is not uncommon in the scientific community that reference is made simply to an "analysis by Leco" without further detail about the specific instrument and method employed.

The instruments used at Elkem Research are a Leco C200 for carbon analysis and a Leco TCH600 for nitrogen and oxygen. In the C200 instrument, the sample is combusted in a ceramic crucible in an induction furnace under O_2 atmosphere, causing carbon to react and form CO_2. The CO_2 content is then measured by IR-spectroscopy.

In the TCH600 instrument the sample is also combusted in an induction furnace, but in a He atmosphere and using a graphite crucible. The oxygen will form CO-gas in the crucible, and as the sample gas pass through a CuO column it is further oxidised to CO_2. In an IR-cell, the CO_2 is then detected by IR-spectroscopy. The sample gas is cleaned for CO_2 by NaOH and $MgClO_4$ before being led into a nitrogen measuring cell. Here, the nitrogen content is detected as a change in thermal conductivity relative to a reference of pure helium gas.

The necessary sample amount is 0.2 g for each parallel, but oxygen and nitrogen can be measured on the same parallel. Since these are combustion methods, the analyses are destructive.

In the current work, the analyses for carbon, nitrogen and oxygen

in all small scale experiments were performed at Elkem Research using these methods.

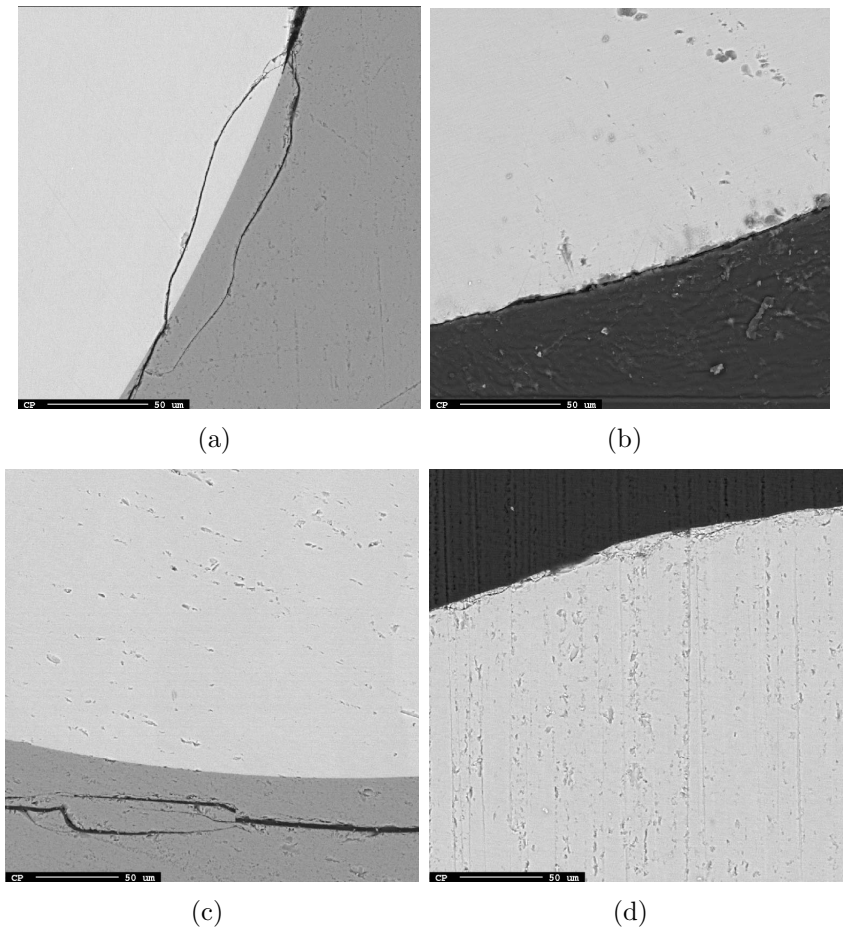

Figure 3.11: Microprobe images of extracted samples. a: the Si-SiO_2 interface on a Si-C sample with the quartz tube still intact. b: the interface between an etched Si-C sample and the surrounding epoxy. c: the Si-SiO_2 interface on a Si-N sample with the quartz tube still intact. d: the interface between an etched Si-N sample and the surrounding epoxy. In neither of the images are SiC or Si_3N_4 particles observed.

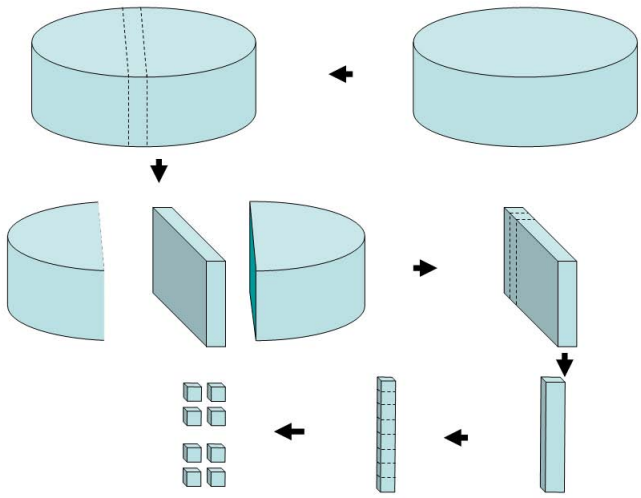

Figure 3.12: Simple sketch illustrating the cutting of the ingot. First, a slab is cut from the ingot, from which is cut a 3 cm x 3 cm column which is then cut into slabs for GDMS or Leco analysis. Note that the sketch is meant as a simple illustration of the cutting, and is not drawn to scale.

Chapter 4

Results

4.1 Results from DS-Si-B-1&2

Slabs were cut from the finished ingots as described in section 3.3.2. From DS-Si-B-1, a single column was cut into eight slabs, while two columns from DS-Si-B-2 were cut into six slabs each. Three slabs from the DS-Si-B-1 casting were analysed at NTNU which included the bottom slab that has only one smooth face, thus a total of five faces were analysed. The analysis was performed at two spots on each face, with three separate analyses in each spot and a five minute sputtering between each analysis.

As two parallels of slabs were cut from DS-Si-B-2, one parallel was analysed at NTNU, while one was sent to external labs for analysis. At NTNU, two series of analyses were performed. In the first series, three slabs were analysed with one spot on each face, three analyses in each spot and a five minute sputtering between each analysis. In the second series of analyses, all six slabs were analysed with one spot on each face and one analysis in each spot. In the following discussion, these two series of analysis are referred to as NTNU-1 and NTNU-

2, respectively. In addition to the samples analysed at NTNU, two slabs were analysed using GDMS at Thermo Fisher Scientific, Bremen, Germany[1], with one spot on each face and only one sample in each spot. The remaining four slabs were analysed at Elkem Research, using ICP-MS for the boron analyses and ICP-OES for the phosphorus analyses. As mentioned in section 3.3.3, ICP-MS and ICP-OES require that the samples are ground down. Therefore, these analyses do not represent a specific height in the ingot, but rather an average over a small vertical interval. All boron data from all analyses of DS-Si-B-1 and DS-Si-B-2 are plotted versus ingot height in Figure 4.1, and all data for other elements are presented in Figure 4.2. Additionally, all data are listed in table form in Appendix A.1.

[1]This is the manufacturer of the GDMS at NTNU.

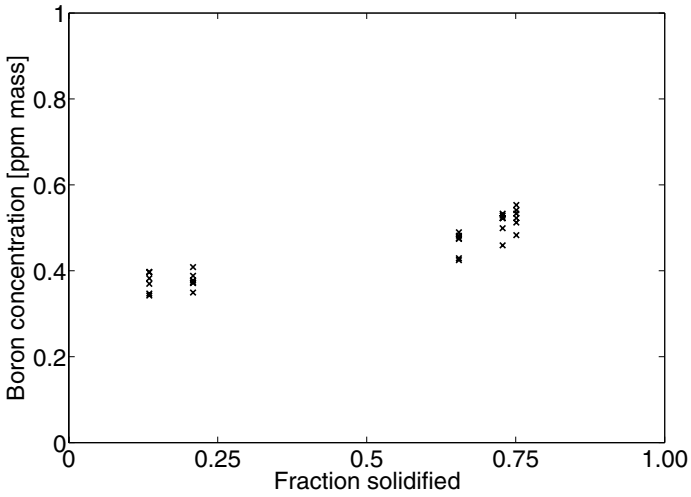

(a)

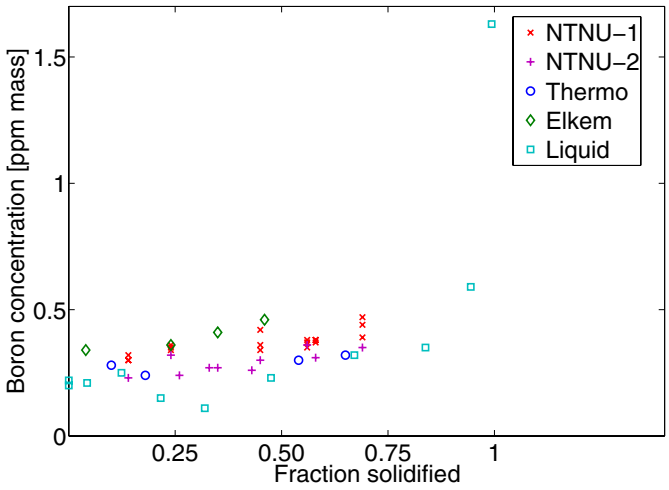

(b)

Figure 4.1: All measured boron concentrations in a: DS-Si-B-1 and b: DS-Si-B-2. For the liquid samples and samples analysed at Elkem, the stated solidified fraction represents the center of the samples that were ground down.

The boron levels are seen to increase with increasing ingot height, as is expected from the Scheil equation for an impurity with a distribution coefficient less than one. The fact that the increase is apparent even in the lower 90 % of the ingot indicates that the distribution coefficient is rather large, somewhere in the region of 0.1-1.0. As shown in Figure 2.8 (page 66) showed, the concentration profile for a very low distribution coefficient would be very flat up until the very top of the ingot.

The absolute values of the boron concentrations range from 0.23–0.55 ppmm, which is reasonable given the feedstock concentration of 0.5 ppmm. However, there seem to be some discrepancies among the analyses at the various laboratories. These will be dealt with in more detail in Chapter 5, where these results are discussed with respect to the derivation of the distribution coefficient of boron.

The GDMS data from Thermo reported sulphur, phosphorus and fluorine in the samples that were not found in the analysis performed at NTNU. The GDMS at NTNU had not shown reliable results with respect to phosphorus, so this element was not included in the analysis. However, a phosphorus level of just below 1 ppm in upgraded metallurgical grade silicon seems reasonable given the relatively high reported distribution coefficients of phosphorus [53]. Similar levels of phosphorous were also reported from Elkem.

In the case of sulphur, ^{32}S is confounded with $2{\cdot}^{16}$O, i.e. an oxygen molecule, which is the likely explanation for this discrepancy. At NTNU, a check was made by analysing for ^{34}S. This should theoretically give the same sulphur levels as when analysing for ^{32}S, but they were lower by one order of magnitude, leading to the conclusion that there were not significant amounts of sulphur in the samples.

The fluorine levels reported at Thermo can not be explained by confounding elements, and were not found in the analysis at NTNU or Elkem. Thus, this remains inconclusive.

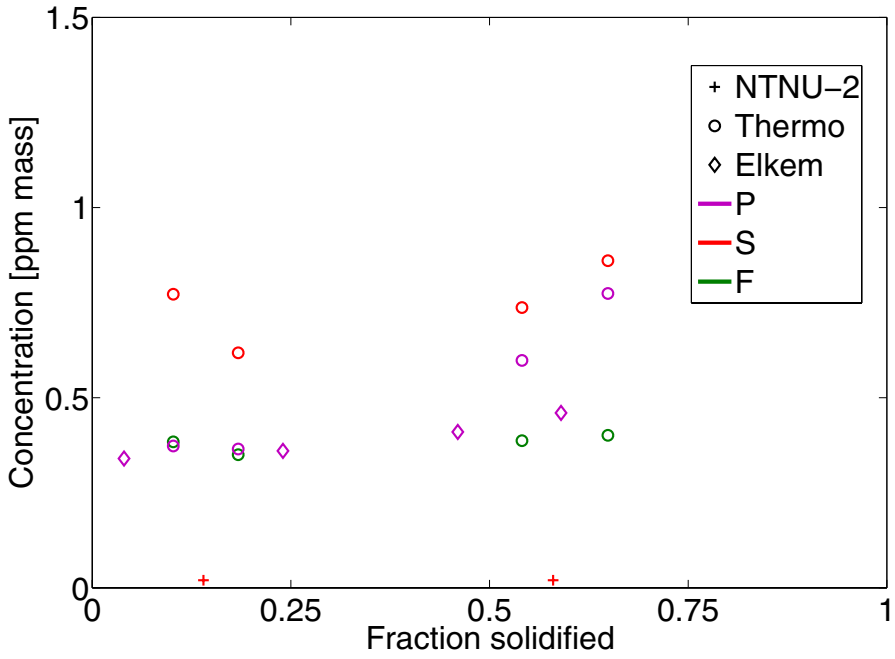

Figure 4.2: Other elements in DS-Si-B-2. For the samples analysed at Elkem, the stated solidified fraction represents the center of the ground down samples.

4.1.1 The liquid samples from DS-Si-B-2

Twelve samples were extracted from the liquid phase during the DS-Si-B-2 experiment. Three were extracted prior to the start of solidification, while nine where extracted at various times during crystallisation. The extraction time was recorded for all samples and compared with the data logged by the furnace control. Discontinuities in the graphs showing temperature and power output versus time revealed at what times the solidification process began and ended. Assuming a constant solidification rate, the fraction of the silicon that was solid at each sampling could be estimated. Figure 4.1 shows the fraction solidified and reported boron levels for all twelve samples. A full tabulation of the data is given in table A.4 in the appendix.

The samples extracted from the liquid phase are seen to follow a Shceil-like distribution, meaning that the liquid was enriched in boron throughout the solidification process, as expected for boron. However, they are seen to lie below the values from the solid phase which is irreconcilable with a distribution coefficient less than unity. This discrepancy between the solid and liquid samples will be discussed in more detail in Chapter 5, in which it will become apparent that the data from the liquid samples are most likely suffering from a systematic error. However, it will also be shown how they can be reinterpreted to tentatively confirm the results from the solid phase.

4.2 Results from the tube furnace

4.2.1 Identification of outliers

Some consideration was made as to what data points to include in the discussion in order to select the points that represent the actual solubility. In order to identify outliers, the carbon and nitrogen levels from all parallels were sorted in groups according to temperature, atmosphere and boron level. Any data point that deviated from the mean of its group by more than two standard deviations was deemed an outlier and removed (in a normal distributed population, an observation will lie within two standard deviations of the mean approximately 95% of the time). This process was repeated for each temperature group until all data points lay within two standard deviations of the group average. Because of the expected segregation in the samples as described in section 2.3.1, any sample that contained an outlying parallel was removed altogether, as the average of the remaining parallels could no longer be expected to represent the true carbon or nitrogen content in the sample.

There can be several reasons why these parallels are outliers. All parallels defined as outliers showed a positive deviation, which suggested pollution. Because of the small sample sizes and low impurity levels, the analyses are prone to disturbances from pollution. Each parallel is run with approximately 0.2 g of sample, so a pollution of only 20 μg is equivalent to 100 ppmm. Thus even the smallest pollution of the sample can have a large effect on the analysis.

In this chapter, all experimental data is presented graphically. For a full tabulation of all numerical data, see Appendix A.

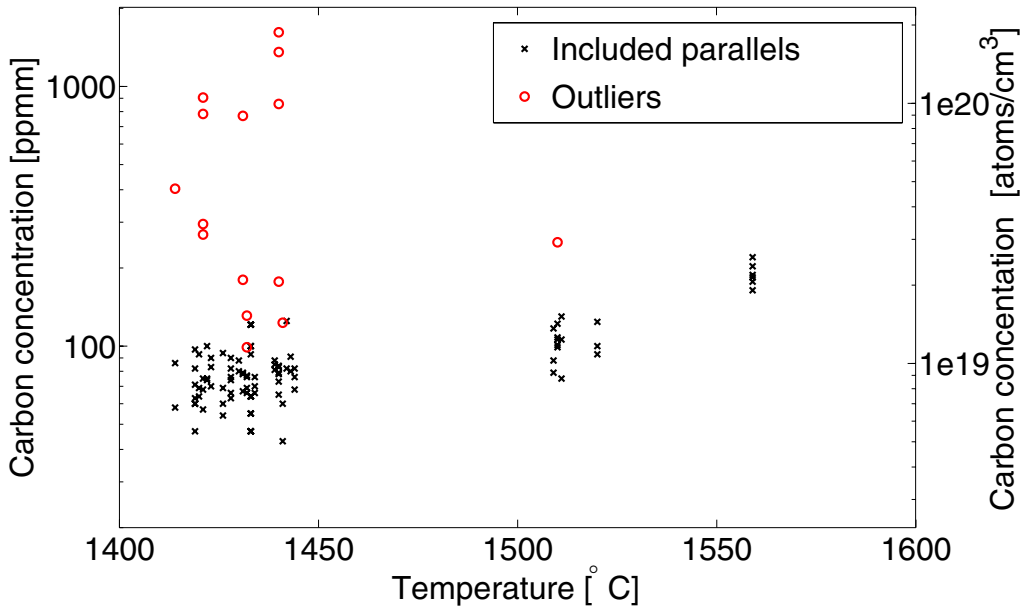

Figure 4.3: Overview of all parallels considered in the discussion of the Si-C system. The red circles represent statistical outliers that were not included in the discussion. A full tabulation of the data is included in Appendix A.2.

4.2.2 Results from the Si–C system: the solubility of carbon in silicon

From five experimental runs, a total of 56 samples were successfully extracted. Of these, 44 samples were analysed in three series of 13 samples each. The samples were analysed in one to four parallels, depending on the amount of silicon available. Figure 4.3 shows an overview of the samples. A full tabulation of the data is included in Appendix A.2.

Carbon content as a function of t_s

Samples were extracted after different settlement times, in order to investigate the evolution of carbon content over time. If a detectable time delay exists in the establishment of equilibrium, it would also be reasonable to expect that there existed a relationship between the carbon content C_C and the settlement time t_s in the form of

$$C_C(t_s) = C_C^0 e^{\frac{-t_0}{t_s}}, \tag{4.1}$$

where t_0 is a measure of the time required to reach the equilibrium concentration C_C^0.

In order to find an estimate for t_0, the data points were grouped together according to temperature as outlined in the previous paragraph. It was assumed that all data points within each temperature group had followed the same time evolution towards the same equilibrium value C_C^0. Using the average concentrations of the different temperature groups as values for C_C^0 and assuming that the time constant t_0 was temperature-independent over the investigated temperature range, the result is a small and negative time constant. This unphysical result implies that there is an infinite amount of carbon in the melt at $t = 0$, and that after a short time this drops off to a constant level. This is of course an impossible result, but the conclusion

can be drawn that the carbon content of the melt is constant during the sampling period, and that any change in composition takes place in the first few minutes. This means that equilibrium is established quickly, and that no samples should be excluded from the discussion based on a short settlement time. Figure 4.4 shows the carbon content versus settlement time for three data temperature groups: the experimental values, as well as the fitted curves.

Carbon content as a function of temperature

Based on the above discussions, the data set with the outliers removed was fitted to an Arrhenius function using the method of least squares. The best fit gave, for the temperature range between 1414–1559 °C:

$$C_C(T) = 482.84 \cdot \exp\left(-\frac{18897}{T}\right) \tag{4.2}$$

Figure 4.5 shows the best fit equation together with all the considered experimental values. At the melting point of silicon (1414° C), the model gives a solubility of 66 ppm mass carbon in liquid silicon.

4.2.3 Results from the Si–N system: the solubility of nitrogen in silicon

A total of five experiments were performed, two in 100 % Ar (experiment Si-N-1 and Si-N-3) and three in 100 % N_2 (experiment Si-N-2, Si-N-4 and Si-N-5). A total of 73 samples were extracted between 1428 and 1542 °C of which 68 were analysed. Depending on the size of the sample, each sample was analysed in one to three parallels for a total of 158 parallels. All parallels are plotted in Figure 4.6, and a full tabulation is given in Appendix A.3.

Of the 68 analysed samples, seven were extracted during experiment Si-N-4. These samples showed a very large variance compared to

the other samples, and while some of the parallels seemed like sensible results, it was decided to disregard all results from this experiment. In addition, any sample with an outlying parallel was removed as described at the beginning of this chapter.

Time dependence of the nitrogen content

Samples were extracted with settlement times of up to two hours. There did not seem to be any variation in the nitrogen levels with time for either atmosphere. In regardt to the case of carbon solubility, an attempt was made to fit the nitrogen content as a function of time to Equation 4.1. Again, a small and negative t_0 was the result. The conclusion must be the same: there is no detectable time delay in the establishment of equilibrium, and no samples should be excluded from the discussion based on a short settlement time.

Effect of the atmosphere

As mentioned in chapter 3.2.2, the effect of the gas phase needs to be considered when investigating the solubility of nitrogen in silicon. This is because nitrogen is able to enter or leave the melt as N_2 gas:

$$2\underline{N}(l) \rightleftharpoons N_2(g) \tag{3.3}$$

This reaction is influenced by the atmospheric conditions in the furnace. If the partial pressure of nitrogen is high, this will drive nitrogen out of the gas phase into the silicon. In the present work, this would be the case for the experiments performed under 100% N_2 atmospheres. In an Ar atmosphere however, the partial pressure of nitrogen would be low, and nitrogen would leave the solution to increase the nitrogen content in the gas phase up to the equilibrium partial pressure. In the

present work, nitrogen would constantly be leaving the melt because the gas phase is not stagnant but rather flows through the furnace.

The solubility data were plotted as functions of temperature for both the Ar and N_2 atmospheres. The data were fitted to Arrhenius equations using the method of least squares, and the results were (the superscripts indicating the atmosphere):

$$C_N^{Ar}(T) = 1.6297 \cdot 10^5 \cdot exp\left(\frac{-29579}{T}\right) \tag{4.3}$$

$$C_N^{N_2}(T) = 1.5730 \cdot 10^5 \cdot exp\left(\frac{-29578}{T}\right) \tag{4.4}$$

These functions are plotted in Figure 4.7. As can be seen from the plot, the variation between the two curves is less than the variation at individual temperatures, indicating that the atmosphere has only a negligible effect on nitrogen solubility. Furthermore, at higher temperatures the equations obtained suggest a higher nitrogen content in an argon atmosphere than in a nitrogen atmosphere. If the atmosphere did have an effect on the nitrogen content, one would expect the opposite result as more nitrogen would be expected to leave the melt through the argon atmosphere. Thus it can be concluded that the atmosphere has no detectable effect on nitrogen solubility, and that the difference between equations 4.3 and 4.4 is simply due to the variance in the experimental data.

The physical implication of this conclusion is that the dissolution of nitrogen into the melt from the crucible walls is much faster than the off-gassing of N_2 gas. This situation can be seen as a dynamic equilibrium, in which nitrogen leaving the melt through the gas phase is immediately replaced by the dissolution of nitrogen from the crucible. A rapid dissolution mechanism at the crucible wall is in agreement with the observed rapid establishment of equilibrium described in the previous paragraph.

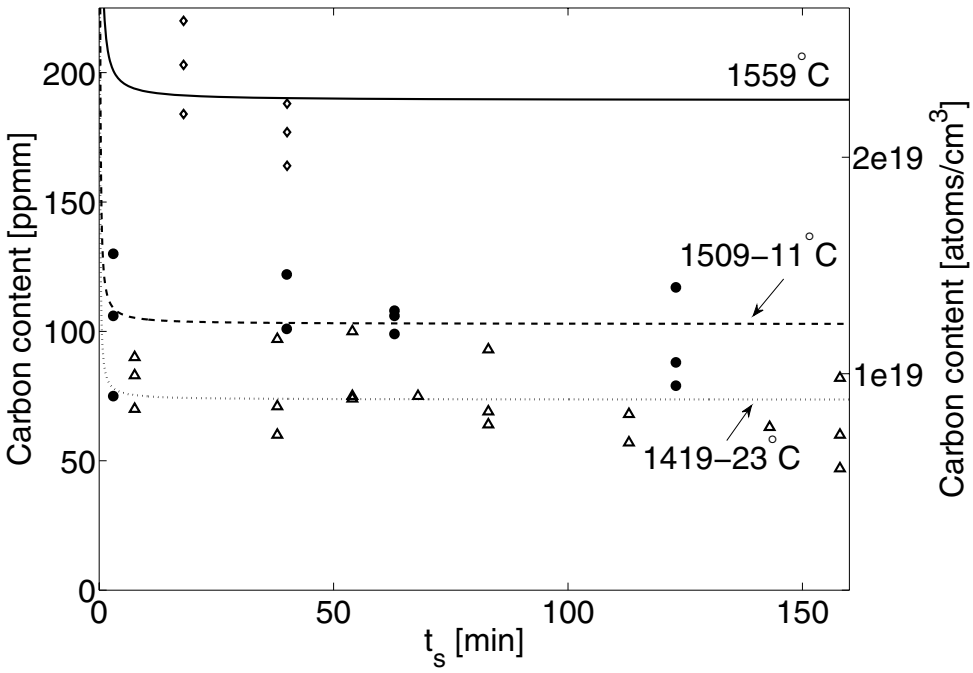

Figure 4.4: The found carbon levels plotted versus settlement time for three results within three temperature groups. The best fit curves are included. The different groups are: T=1419-23°C: Triangular markers and dotted curve; T=1509-11°C: Circular markers and dashed curve; T=1559°C: Diamond markers and solid curve.

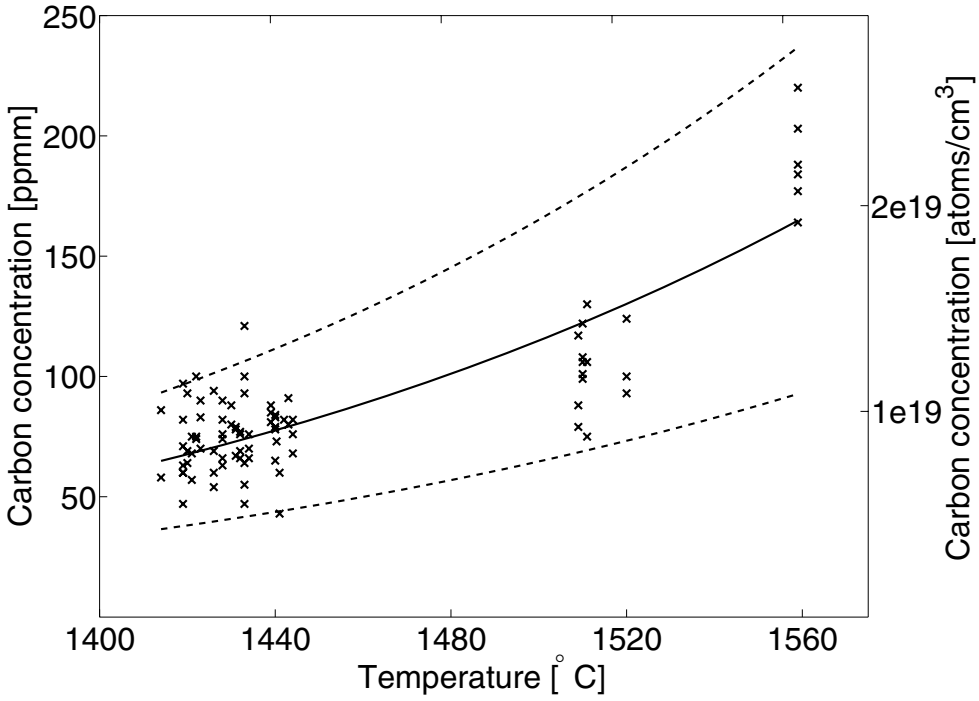

Figure 4.5: Carbon concentration as function of temperature. The experimental points are shown together with the plot of the best fit Arrhenius equation. The dashed curves represent a 95% confidence interval.

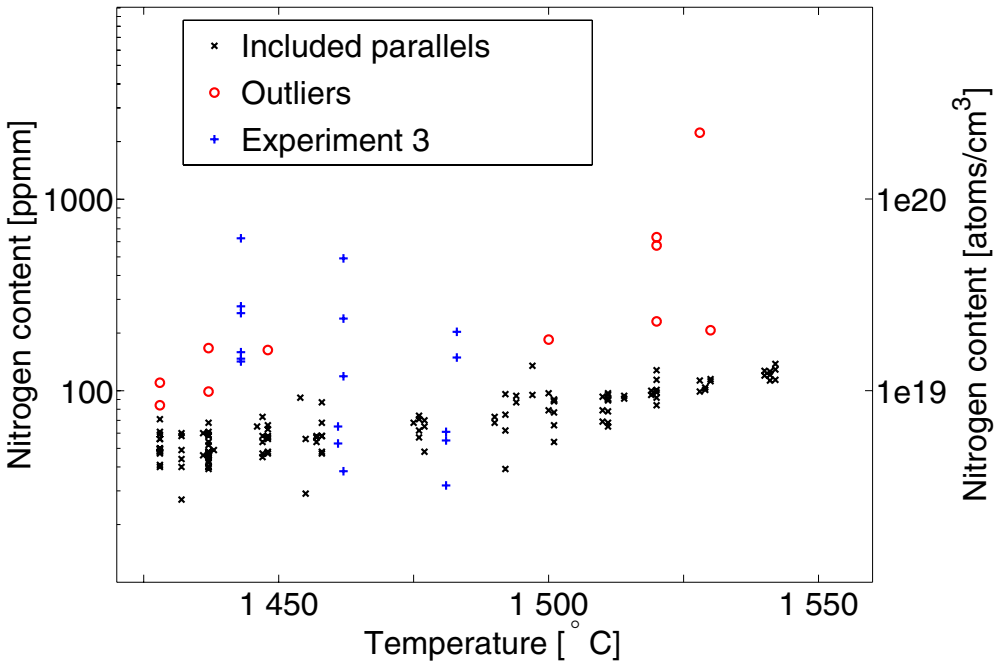

Figure 4.6: Overview of all Si-N parallels plotted versus temperature. The blue crosses represent results from experiment 3 that were excluded due to large variance, while the red circles indicate parallels classified as outliers from a statistical argument. The black crosses represent the data taken into account in the analysis

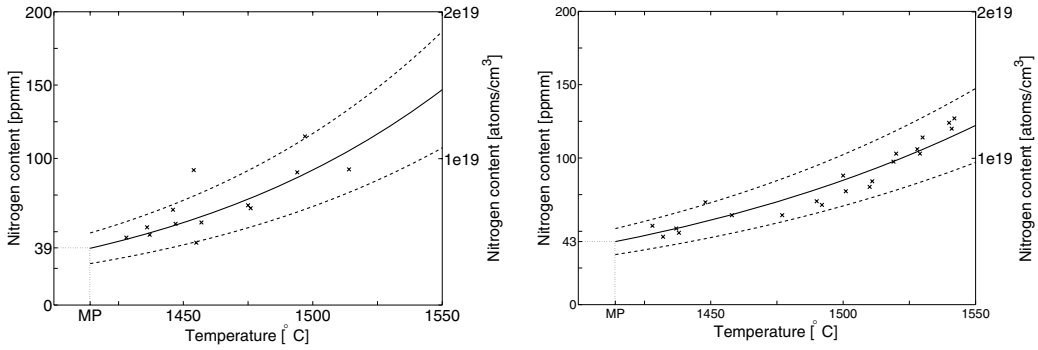

(a) Ar atmosphere (b) N_2 atmosphere

Figure 4.7: Nitrogen solubility as a function of temperature based on experiments performed in a: Argon atmosphere and b: Nitrogen atmosphere. The dashed curves indicate a 95 % confidence interval of the predicted values.

Temperature dependence of the nitrogen solubility

Having established that the choice of atmosphere has no effect on the nitrogen content in the melt, the next logical step is to simultaneously analyse the two data sets. Fitting an Arrhenius equation to the combined solubility data, the result is:

$$C_N(T) = 1.0484 \cdot 10^5 exp\left(\frac{-28841}{T}\right) \tag{4.5}$$

This equation is valid between 1428 and 1542 °C. Extrapolating to the melting point of silicon, this equation gives the solubility of nitrogen in liquid silicon as 39 ppmm with a standard deviation of 8 ppmm.

4.2.4 Simultaneous saturation of carbon and nitrogen in liquid silicon

Six experimental runs were conducted in the Si–C–N-system, from which 107 samples were extracted in the temperature range between 1422–1525 °C. Of these, 34 samples were analysed in two to three parallels each. Because of limitations in the sample size, each sample could not be analysed for both carbon and nitrogen. Therefore, half the samples were analysed for carbon, while the other half were analysed for nitrogen. The results for all parallels are shown in Figure 4.8 and a full tabulation of the data can be found in Appendix A.4.

One analysed sample from Si-C-N-4, indicated with asterisks in Figure 4.8, was extracted at 1428 °C at the end of an experiment during cooldown. Prior to this sampling, the melt had been exposed to temperatures of over 1500 °C for ∼45 minutes with a maximum temperature of 1519 °C. This sample showed a higher nitrogen content than other samples extracted at similar temperatures, as is to be expected from a sample extracted during cooling. Thus, this sample is not representative of the solubility limit at 1428 °C and was not

included in the analysis of the data. This exemplifies the necessity of only extracting samples at increasing temperatures as described in section 3.2.2.

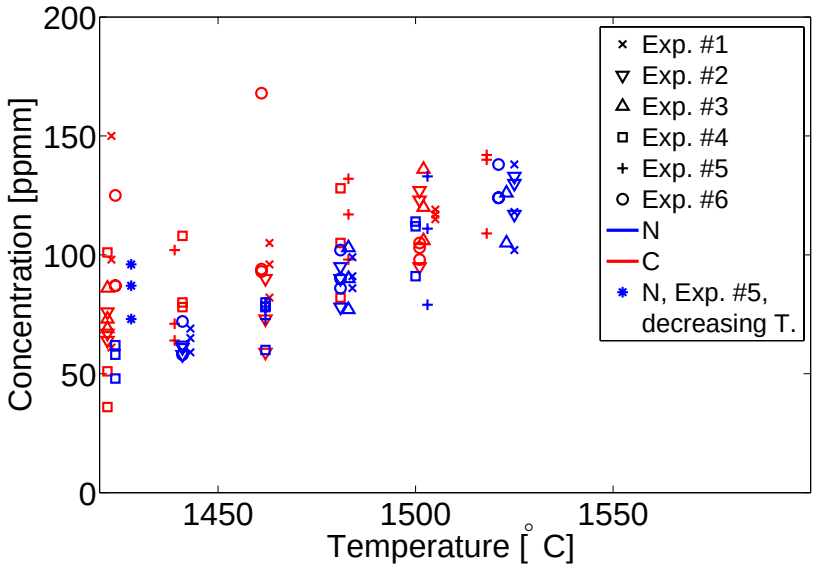

Figure 4.8: All parallels from the Si-C-N experiments. Red markers indicate carbon and blue markers nitrogen. The shape of the markers indicates the day of the experiment. The three asterisks represent the nitrogen level in three parallels from a sample extracted during decreasing temperature, which were not included in the discussion.

The remaining parallels were used in the fitting of two Arrhenius equations, the first of which describes the carbon solubility in a nitrogen saturated silicon melt as a function of temperature while the other equation describes the nitrogen solubility during carbon satura-

tion. The resulting equations were

$$C_C^{N_{Sat}} = 5.84 \cdot 10^7 \exp(-23451/T) \quad (4.6)$$
$$C_N^{C_{Sat}} = 3.88 \cdot 10^5 \exp(-14420/T) \quad (4.7)$$

Here, the superscript X_{Sat} indicates saturation of substance X. These equations are displayed in Figure 4.9 together with the experimental points and curves for the pure systems. It can be seen that the predicted nitrogen solubility is higher at all temperatures for the carbon-saturated case. The case for carbon-solubility is not so straightforward, as the two solubility curves can be seen to intersect at approximately 1500 °C. This is caused by the data point at 1560 °C in the pure system predicting a very high solubility. This data point lies well outside the temperature range of the experiments performed during nitrogen-saturation, and the inclusion of this data point in the comparison of the two data sets is thus debatable. For this reason, a new Arrhenius equation was fitted to the data obtained from the pure Si-C system in the temperature range between 1414 °C–1520 °C. The resulting equation was:

$$C_C(T) = 73700 \cdot \exp(-11731/T) \quad (4.8)$$

This equation is plotted as the blue curve in Figure 4.9(a). It is seen to lie well below the equation for the nitrogen-saturated system, which is analogous to the case for nitrogen solubility under carbon saturation.

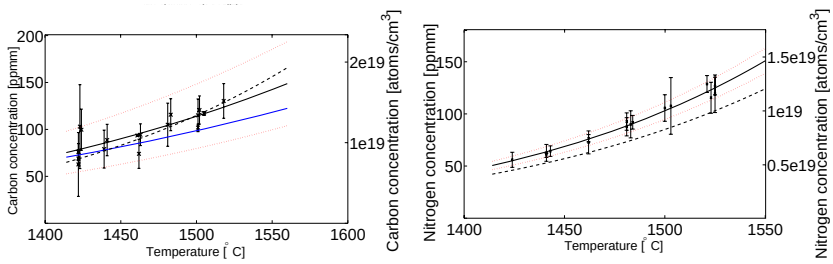

(a) (b)

Figure 4.9: The best fit Arrhenius equations for the solubility of nitrogen and carbon during simultaneous saturation in liquid silicon. In both cases the dashed curve indicates the solubility limit in the pure system, while the red dotted curves indicate a 95 % confidence interval of the solubility in the saturated Si-C-N system. a: The solubility of carbon during nitrogen saturation. The blue curve represents the equation found for the pure Si-C case when only including results from 1520 °C and below. b: The solubility of nitrogen during carbon saturation.

4.2.5 Results from the Si–C–B-system: the effect of boron on carbon solubility

From seven experiments with boron-enriched silicon melts in graphite crucibles, a total of 97 samples were extracted and 75 analysed. The samples were analysed in one to four parallels, depending on the amount of sample available in each case. All considered parallels are illustrated in Figure 4.10 together with the removed outliers. A full tabulation of the data is presented in Appendix A.5.

An Arrhenius expression showing the temperature dependence of the carbon solubility was constructed from the experimental data for each of the different levels of boron additions. Figure 4.11 shows the plots of the best fit equations together with the result for the pure silicon as discussed in the previous section. It can be seen that in all cases carbon solubility is greater with boron additions present compared to the case of pure silicon. In addition, apart from the case of 0.25%/0.50%, the carbon concentration increases with increasing boron content.

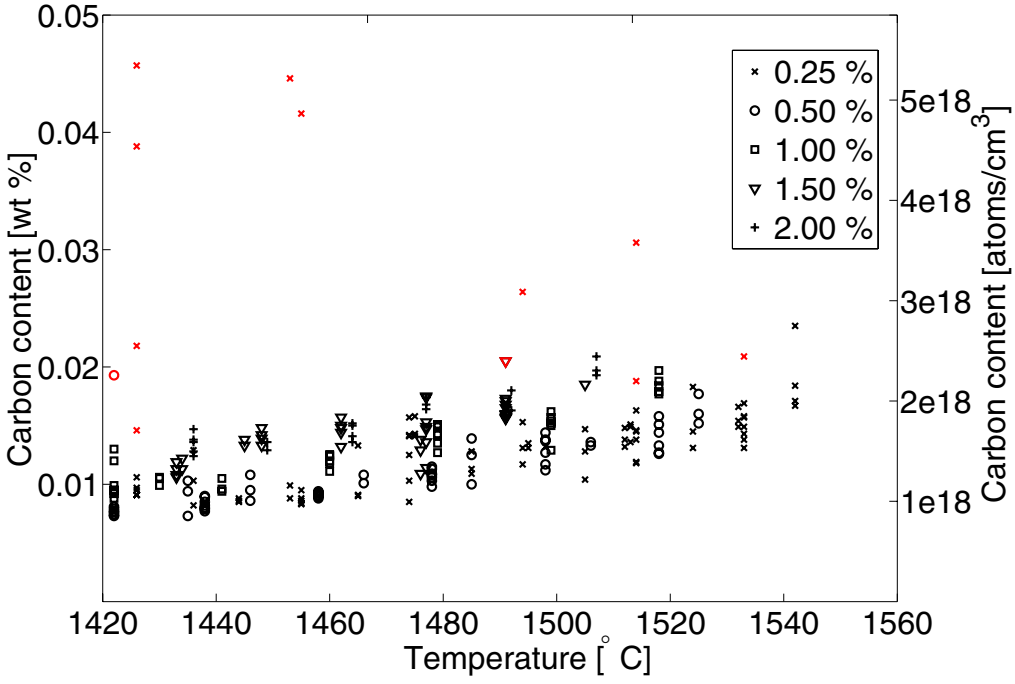

Figure 4.10: Overview of all parallels considered in the discussion of the Si-B-C system. Red markers indicate outliers that have been excluded from the discussion. Note the logarithmic scale on the y-axis.

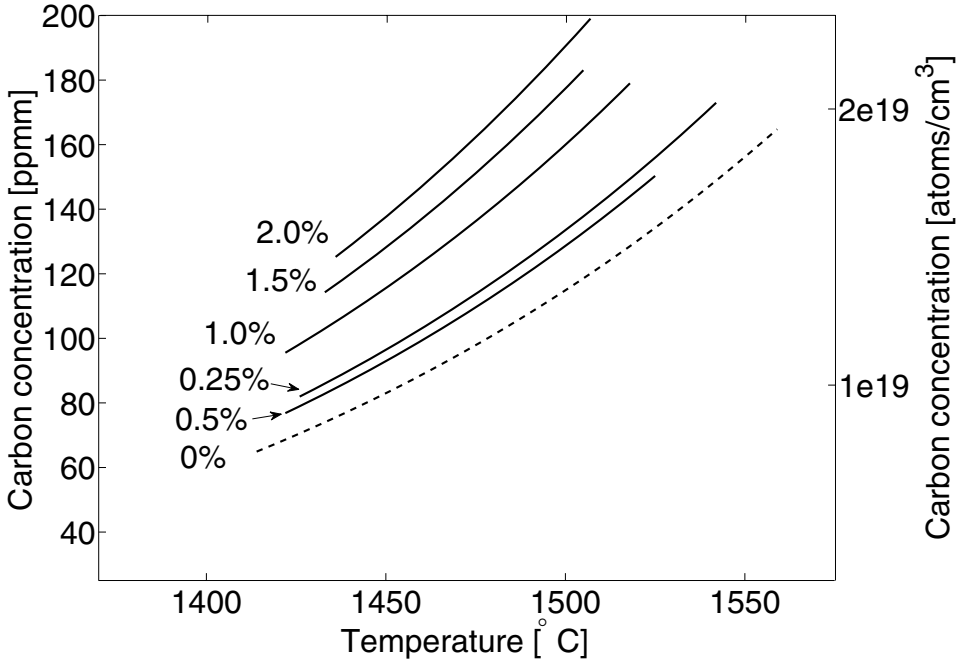

Figure 4.11: Carbon solubility as a function of temperature for different boron additions. The dashed curve indicates pure silicon, and is included for reference.

4.2.6 Results from the Si–N–B-system: the effect of boron on nitrogen solubility

As a preliminary investigation of the Si–N–B-system, two experiments were performed in a Si_3N_4 crucible with boron additions. From these, 37 samples were extracted of which 16 were analysed. Since there exist the possibility of BN-precipitation in the Si–B–N-system, it was decided that one experiment should be performed at a boron level at which no BN would be expected to be found, while the other was performed at a high level of supersaturation. According to the experiments of Noguchi et al. [64], the saturation level of boron in liquid silicon at p_{N2}=$1.01 \cdot 10^4$ Pa and 1450 °C is 0.193 m.%. The saturation level was found to decrease with increasing p_{N2}. Since the partial pressure of nitrogen in the current work was close to zero, it was decided that the experiments should be performed at 0.10 m.% and 1.50 m.% boron additions, respectively.

The nitrogen data obtained were fitted to Arrhenius equations describing the nitrogen content as a function of temperature at a given boron level. Figure 4.12 shows these equations together with the experimental points and the graph of equation 4.5 for the boron-free case. It can be seen in both cases that the presence of boron in the system reduces the nitrogen content. This effect is also more pronounced in the case of a 1.5 m.% addition than for a 0.1 mass% addition.

Figure 4.13 shows a microprobe image from the Si-B-N-2 experiment. Two main phases can be identified: the matrix which is silicon with dissolved nitrogen and boron, and a grey phase that appears to have formed in a eutectic reaction. Chemical analyses reveal this phase to be rich in silicon and boron, consistent with the phase being a silicon boride. No nitrogen was detected in this phase. The matrix and the assumed silicon boride were the only phases detected. No BN was found.

The boron levels of two of the extracted samples were also mea-

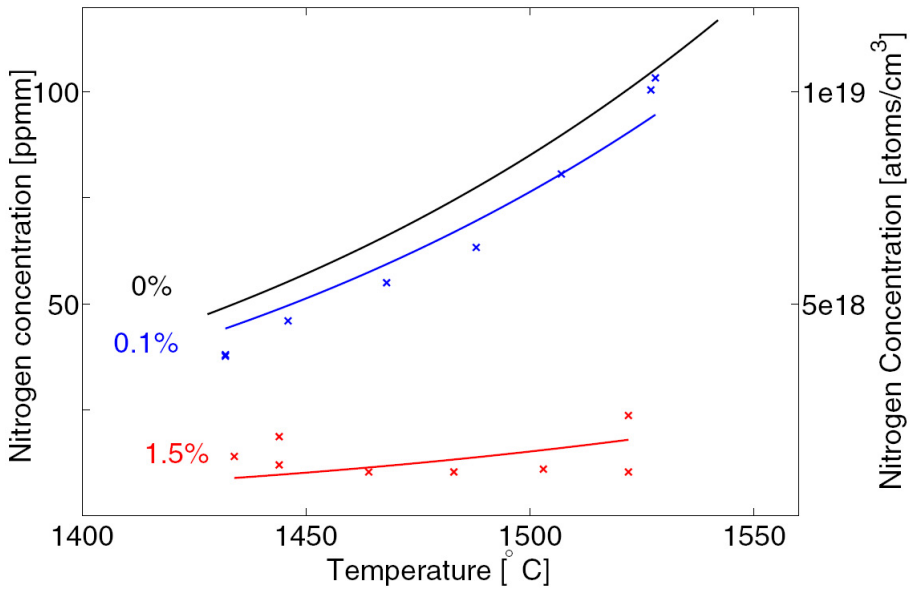

Figure 4.12: Arrhenius equations describing the nitrogen solubility as function of temperature for different boron levels.

sured using ICP-MS, 0.08 m.% and 1.43 m.% were obtained for the two experiments, respectively.

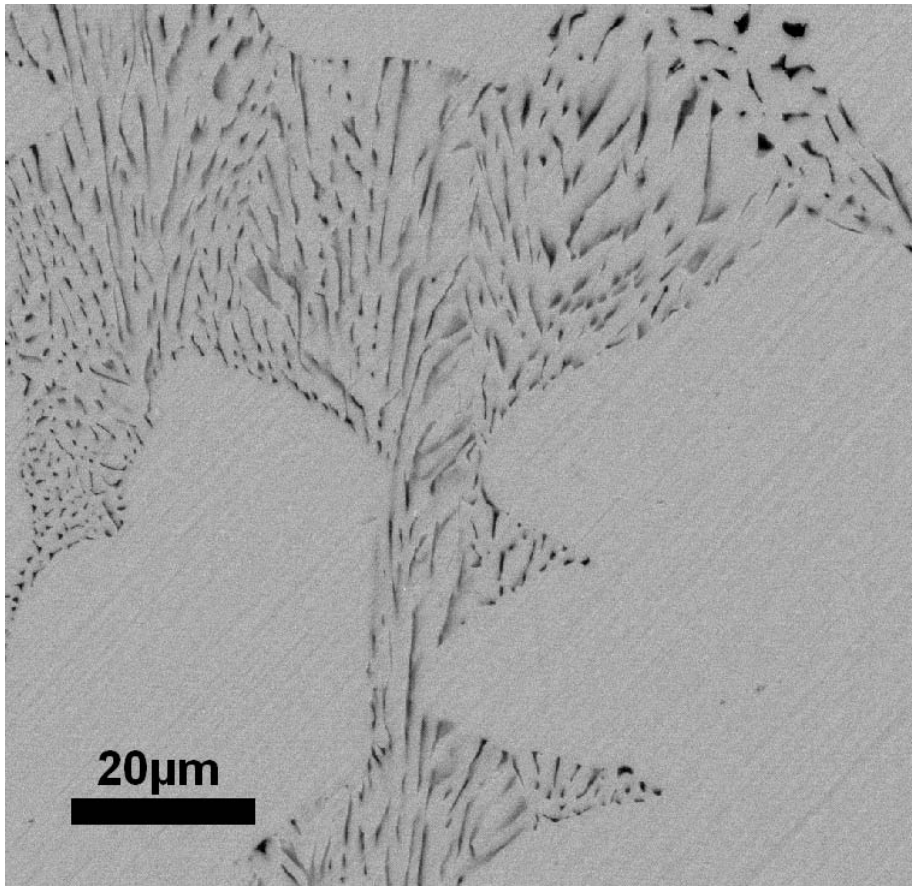

Figure 4.13: Microprobe image of a sample from the Si-B-N-2 experiment. The grey matrix is silicon and the darker grey phase is identified as a silicon boride, possibly SiB_6.

Chapter 5

Discussion

5.1 The distribution coefficient of boron in silicon

As expected, the boron data from the DS-Si-B-1 and DS-Si-B-2 experiments did not show a uniform distribution throughout the ingot. Because of the difference in solubility in solid and liquid silicon as described in section 2.3, the concentration will display a variation throughout the ingot determined by the equilibrium distribution coefficient as described by the Scheil equation:

$$C_{solid}(f) = k_0 C_0 \cdot (1-f)^{k_0-1} \tag{2.44}$$

This equation is valid under the assumption of a flat solid–liquid interface, negligible solid state diffusion and a perfect mixing in the liquid phase. As previously mentioned the liquid phase will not be perfectly mixed in real cases, although the Scheil equation can still be used if the equilibrium distribution coefficient is replaced by the effective distribution coefficient k_e:

$$C_{solid}(f) = k_e C_0 \cdot (1-f)^{k_e-1} \tag{5.1}$$

k_e is the ratio between the impurity concentrations at the interface of the solid phase and in the bulk of the liquid phase, and is related to k_0 through equation 2.45.

In order to estimate the effective distribution coefficient of boron in silicon, the boron-data obtained from the different analyses and experiments were fitted to the Scheil equation using a recursive method in which both C_0 and k_e were determined by fitting the experimental data. The GDMS-data from the DS-Si-B-1 casting is shown in Figure 5.1. The best fit of Scheil's equation gave a value of the distribution coefficient of $k_e = 0.80$. This best fit is plotted in Figure 5.1 together with the data points. The starting concentration was calculated to 0.44 ppmm, which is in good agreement with the 0.5 ppmm value as given by Elkem.

The same analysis of the boron-data was performed for the DS-Si-B-2 casting for both the individual analyses and the complete data set. The individual subsets gave values ranging from 0.69 to 0.86 for the distribution coefficient while the best fit to the complete data set, seen in Figure 5.2, gave 0.75. In this case, the starting concentration of boron was calculated as 0.37 ppmm.

The distribution coefficients of the various data sets are indicated in Figure 5.2 and also tabulated in more detail in Table 5.1. The right column of this table gives the residual error of the regression, which is a measure of how well the best-fit Scheil equation reproduces the experimental data. As the residual error is calculated as the sum of squares of the differences between the experimental and modelled values at all data points, it will increase with sample size. The values given in Table 5.1 are therefore divided by the number of parallels used in each regression so that they become comparable.

It can be seen that the spread in results among the different laboratories and analyses causes the residual error to be greatest when all the data are included. This indicates that the k_e based on all data may not be the best possible estimate.

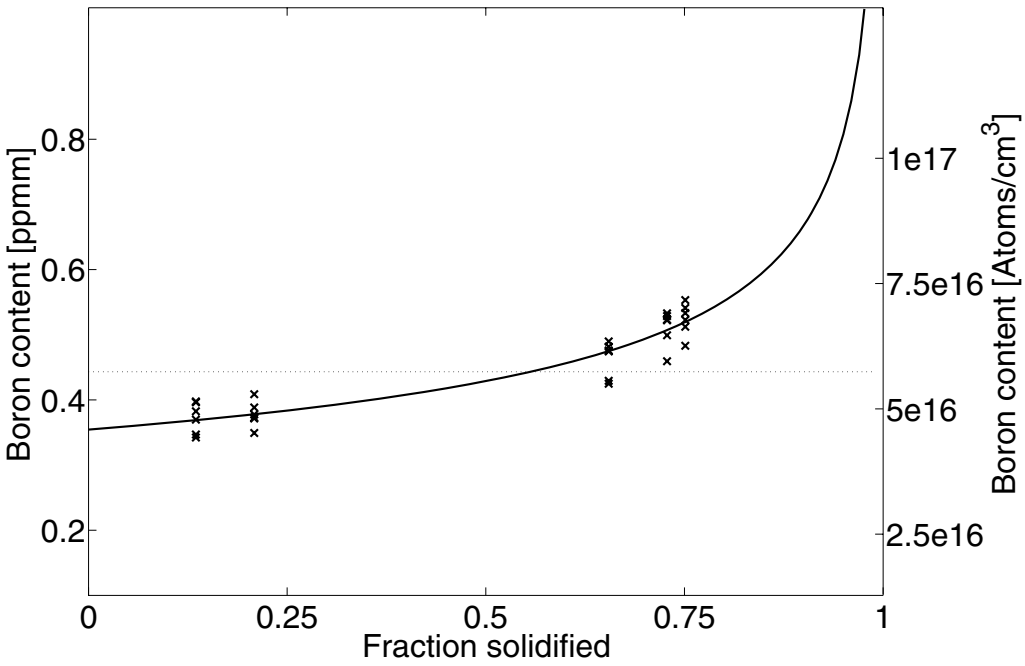

Figure 5.1: Boron distribution in the DS-Si-B-1-casting. The solid curve represents the best fit of the data to Scheil's equation with $k_e = 0.80$. The dotted horizontal line indicates the starting concentration of boron calculated to $C_0 = 0.44$ ppmm.

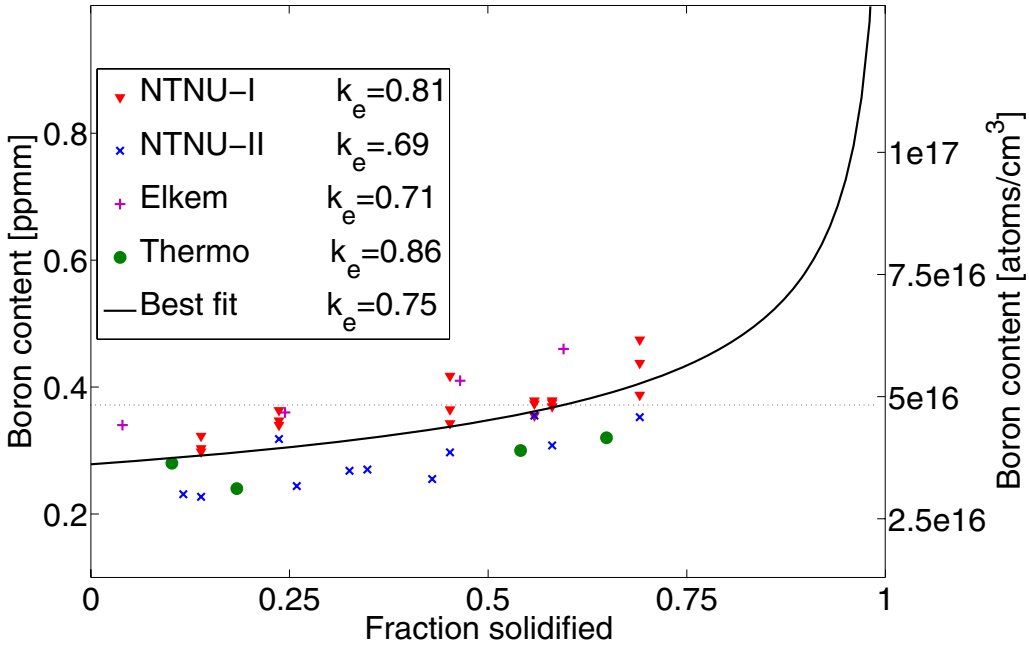

Figure 5.2: Boron as a function of solidification height in the DS-Si-B-2-casting. Best fit Scheil curve together with the data points from the various analyses. The distribution coefficients obtained from each individual data set are indicated in the legend. he dotted horizontal line indicates the starting concentration of boron calculated to $C_0 = 0.37$ ppmm.

Table 5.1: Distribution coefficient of boron in silicon as calculated from the different data sets. The number of parallels and the total residual error per parallel are indicated in each case.

Casting	Analysis	k_e	C_0	Number of parallels	total residual error per parallel [$\cdot 10^{-3}$]
DS-Si-B-1	NTNU	0.80	0.44	30	0.56
DS-Si-B-2	NTNU-1	0.81	0.38	18	0.63
DS-Si-B-2	NTNU-2	0.69	0.34	11	0.67
DS-Si-B-2	Elkem	0.71	0.47	4	0.018
DS-Si-B-2	Thermo	0.86	0.29	4	0.26
DS-Si-B-2	All	0.75	0.37	37	2.27

The measurements from NTNU-1 and NTNU-2 were made using the same instrument on the same sample-set, and should therefore show the same results. However, the results from NTNU-1 seem to be displaced upwards by a few tenths of a ppm relative to the later results. The samples from DS-Si-B-1 were also analysed using the same instrument. Even though these results were obtained from a different experiment, the experimental conditions were similar enough that—theoretically—one would expect the same results in all three analyses. It is apparent from Figures 5.1 and 5.2 and Table 5.1 that the data from DS-Si-B-1 agree better with the NTNU-1 analyses from DS-Si-B-2 than the NTNU-2 analyses.

In order to investigate the effect a constant displacement of all data points would have on the estimated k_e, a perfect artificial data set was created using the Scheil equation with k_e=0.7 and C_0=0.5 ppmm. This data set was then fitted several times to the Scheil equation, displacing the boron levels of the entire data set by a certain amount each time. The resulting k_e was then plotted as a function of displacement in

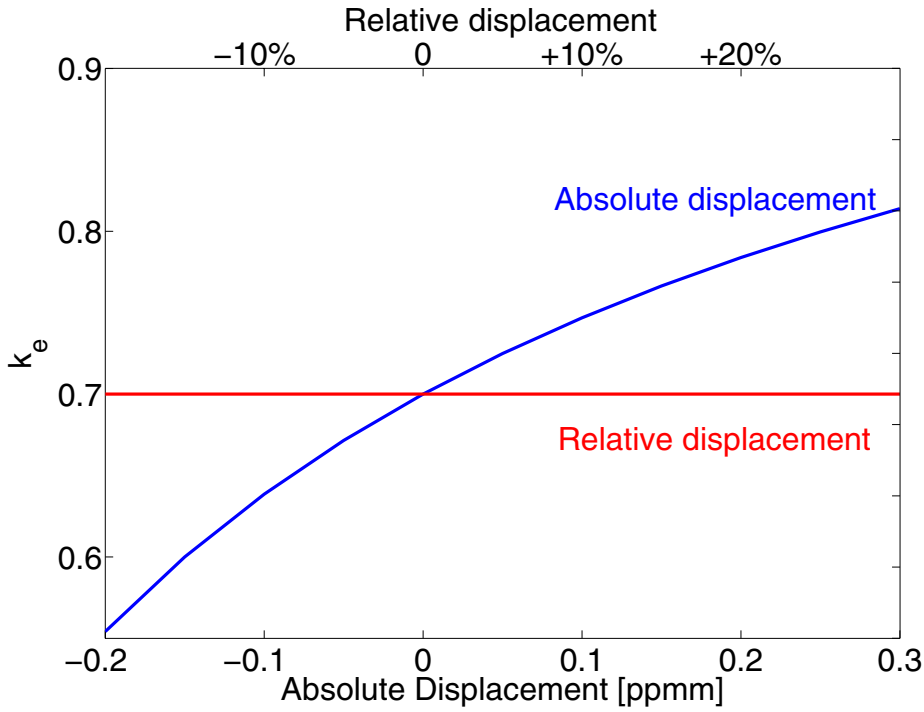

Figure 5.3: Effect of displacements of the data set on the predicted distribution coefficient. The red curve illustrates the situation when all data is displaced by a relative amount, while the blue curve shows the situation when all data is displaced by an absolute amount.

Figure 5.3 for two different cases of displacement. The red line in the figure illustrates that when all data points are changed with a given percentage, the outcome of the best fit distribution coefficient does not change. On the other hand, the blue curve shows the situation when all results are displaced by a constant absolute amount. It is clearly demonstrated that this has a significant influence on the predicted segregation coefficient, with the segregation coefficient being displaced in the same direction as the data points. So if all the data points are overestimated by a small amount, this means that the segregation coefficient will also be overestimated.

This explains the observation that the data from NTNU-1, which show slightly higher absolute values than NTNU-2, also gives a slightly larger value for k_e.

If NTNU-1 is correct, then the data from Thermo are not in the right area, but give a similar distribution coefficient to NTNU-1. The data from Elkem would be in the right area, but they predict a k_e of 0.71 as opposed to 0.81 which is the result derived from NTNU-1. These data cannot be made consistent by assuming a constant displacement of the Thermo and/or Elkem data. The Elkem data are already in the proper area, so any displacement to correct the distribution coefficient would no longer make the absolute values agree with NTNU-1. If the Thermo data are assumed to suffer from a systematic negative deviation, this would mean that 0.86 is too low of a value for k_e, so the adjusted k_e would not agree with that found from NTNU-1.

In contrast, if NTNU-2 is correct, then the Elkem data give the correct distribution coefficient without being in the correct area, while the Thermo data are in the correct region but give the wrong distribution coefficient. Again, an assumption of a constant displacement of the Elkem data will not make the data sets consistent with respect to both the absolute values and distribution coefficient.

One possible explanation is that the data from Elkem are wrong by a set percentage. Since a constant relative error does not influence

the estimate of the segregation coefficient, this would explain why the Elkem and NTNU-2 analyses give different absolute values but similar segregation coefficients. The same method can also be used to make the Thermo data consistent with NTNU-1, but neither an absolute or relative displacement can explain the discrepancies between the Elkem and NTNU-1 data.

Looking at the data from Thermo in Figure 5.2, it appears that either the first or second data point from the bottom of the ingot is slightly off—a Scheil curve can easily be drawn through the remaining three points if one of these is removed. If the very bottom data point at 0.10 fraction solidified is removed, the k_e-estimate becomes 0.72, while this changes to 0.95 if the bottom data point is included but the second one left out. This demonstrates the large influence a single data point has on the results of such a small data set. If it is the first data point that is wrong, the data from Thermo actually agree quite well with NTNU-2 with respect to both the absolute values and estimated distribution coefficient. It is impossible however to decide which data point is the outlier with only two other points to compare it with.

Nevertheless, the assumption that NTNU-2 is correct allows for plausible explanations as to why the other analyses are in disagreement. If NTNU-1 is assumed to be correct, the results from Thermo and Elkem cannot be as easily explained.

The NTNU-1 and NTNU-2 analyses were performed at a time when the GDMS at NTNU was still reasonably new, and the instrument was in the process of being "broken in". The data from DS-Si-B-1 were obtained at an earlier time than the NTNU-1 analyses from DS-Si-B-2. So if there was a small discrepancy present in the analytical method during the NTNU-1 analyses, it would also presumably be present in these earlier analyses. It would be logical to assume during this period that the performance of the instrument and operator improved over time, in which case more faith should be placed in the later results.

The conclusion of the current discussion is therefore that the data from NTNU-2 is believed to be the most accurate. This conclusion implies that the data from NTNU-1 and DS-Si-B-1 show values which are too high and are displaced by a constant amount. It also implies that the data from Elkem have a constant, positive, relative error, that the first data point from the Thermo analysis is wrong and that the effective distribution coefficient of boron in silicon is around 0.7.

Based on these conclusions, the best estimate of k_e will be an average of the values obtained from the Elkem data, the NTNU-2 data, and the top three data points from the Thermo data weighted after number of parallels:

$$k_e = \frac{1}{11+4+3}\left(11 \cdot 0.69 + 4 \cdot 0.71 + 3 \cdot 0.72\right) = 0.70. \tag{5.2}$$

Liquid samples

The reported boron content of the liquid samples from DS-Si-B-2 are shown in Figure 5.4. The curve of the best fit Scheil equation obtained from the solid data of the same experiment is also shown in the same figure, as well as the boron content that could be expected to be found in the samples if the results from the solid samples are correct.

The liquid samples obviously do not fit very well with the solid samples, as a lower boron content in the liquid compared to the solid phase indicates a distribution coefficient greater than one. If this was the case however, then the boron contents in both the liquid and solid samples should decrease with increasing fraction of solidification. Since the opposite is observed, either the liquid or the solid data must be incorrect. The results from the solid samples are based on a greater amount of data, and these samples were analysed at several different laboratories using various methods, giving them a higher credibility than the single set of liquid samples that were analysed at a single

laboratory. The conclusion is that the reported boron contents of the liquid samples are not on the correct level.

Nonetheless, looking at Figure 5.4 the results do seem to follow a Scheil-like distribution, albeit at absolute values which are too low. This, and the reproducibility demonstrated by the fact that the three samples extracted before the start of solidification show more or less the same boron content, lends at least some credibility to these data. Therefore, an attempt is made to extract useful information from them.

The absolute difference of the calculated starting concentration C_0 and the average of the three samples extracted before the onset of solidification is 0.17 ppm mass. By scaling all the data upwards by this amount, the liquid data can be made more consistent with the solid data. By fixing the starting concentration at 0.37 and fitting the scaled up liquid data to the liquid Scheil equation the distribution coefficient is determined as $k_e = 0.77$.

At the outset of the present work, it was planned to estimate the distribution coefficient through a direct comparison of the found boron contents in the liquid and solid phases throughout the ingot. By using the scaled liquid data, an estimate of the distribution coefficient can be made by calculating the ratio between the boron content in the liquid phase and the calculated boron content in the solid phase at the same point in the solidification. Taking the average of all these estimates, one obtains:

$$k_e = \frac{1}{12} \sum_{i=1}^{12} \frac{C_{calc}^{solid}}{C_{experimental}^{liquid}} \tag{5.3}$$

This calculation produces an estimate of the distribution coefficient of $k_e = 0.90$. In conclusion it can be said that the data from the liquid phase point in the same direction as the solid samples, and to a certain degree confirm them. However, due to the poor quality of the original

liquid data, too much emphasis cannot be put on these results.

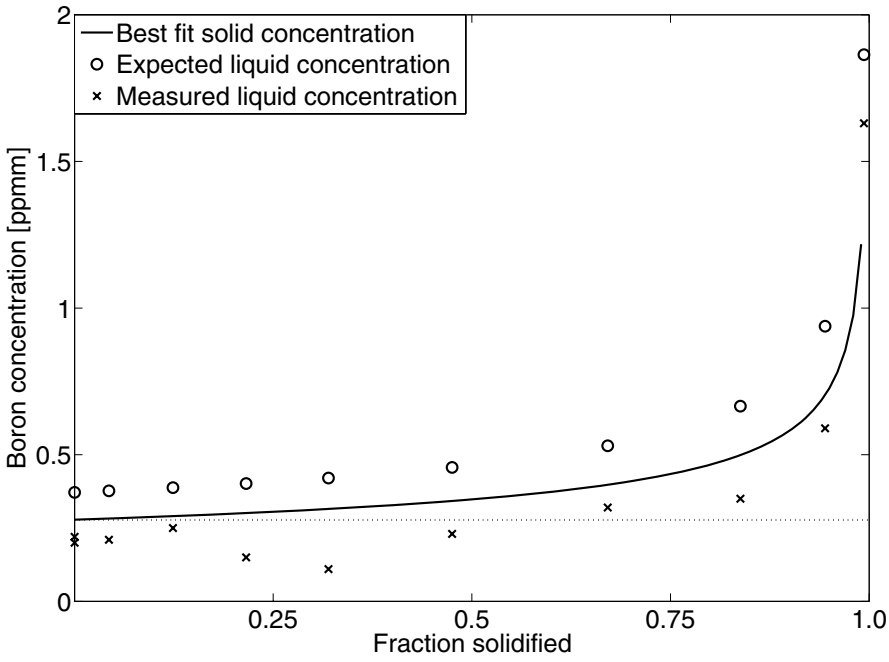

Figure 5.4: Comparison between the actual reported data from the liquid phase and the values expected from the results found in the solid phase of the DS-Si-B-2-experiment. The curve represents the calculated boron distribution in the solid phase and the dotted horisontal line the calculated starting concentration of boron.

Comparison with previous results

Based on the solid samples, the effective distribution coefficient of boron in silicon was determined to 0.70 for the DS-Si-B-2 casting. This is in reasonable agreement with the data available in literature. In Czochralski silicon, k_e has been determined by Huff et al. to $k_e = 0.7$ [53], by Sim et al. to $k_e = 0.738 \pm 0.006$ [54], and by Ravishankar et al. to $k_e = 0.786 \pm 0.036$ [55]. Ravishankar et al. also investigated Bridgman grown polycrystals, and reported $k_e = 0.803 \pm 0.036$ in Bridgman polycrystals [55]. However, they used growth rates of 5 and 10 cm/hr, which are significantly higher than the 0.7 cm/hr used in the present work. It is therefore not surprising that they obtained slightly higher values for k_e.

Phosphorous segregation

Although it was not intended to be a part of this thesis at the outset of the current work, I will report on the limited results of phosphorous segregation. The analyses of samples from DS-Si-B-2 at Elkem and Thermo gave a limited amount of data from which a rough estimate of the distribution coefficient of phosphorous could be made. Through a fitting of this data to Scheil's equation, the effective distribution coefficient was determined as:

$$k_e^P = 0.27 \tag{5.4}$$

This is in reasonable agreement with the work of Huff et al. [53], who found 0.32 and 0.42 respectively.

5.2 Solubility of carbon and nitrogen in liquid silicon

5.2.1 Solubility data

Si–C

The solubility of carbon in liquid silicon as a function of temperature in the temperature range between 1414–1559 °C was found to follow:

$$C_C(T) = 482.84 \cdot \exp\left(-\frac{18897}{T}\right) \tag{4.2}$$

Figure 5.5 shows this equation together with results reported by other authors. All results have been extrapolated to the melting point of silicon for reference.

The present work is seen to show a good agreement with Ottem [36], with similar results near the melting point of silicon, and only a slight difference in the temperature dependency. Reasonable agreement is also seen with the works of Hall [20] and Yanaba et al. [33] Hall agrees on the solubility limit at the melting point, but predicts a more pronounced temperature dependence. On the other hand, Yanaba and co-workers predict a 20 % higher carbon content at the melting point, while their temperature dependency is closer to those found in the present work and by Ottem.

Poor agreement is seen with the results of Scace and Slack [19], Oden and McCune [31], and the review by Durand and Duby. [22]

Weaknesses around these publications have already been pointed out in section 2.1.1. In the works of both Scace and Slack and of Oden and McCune, carbon might have been lost in the sample preparation process, as portions of the silicon ingots were removed before analysis. The work of Durand and Duby is a review article based on the data of Kleykamp and Schumacher [37], Hall [20], and Dash [19, 20], but their

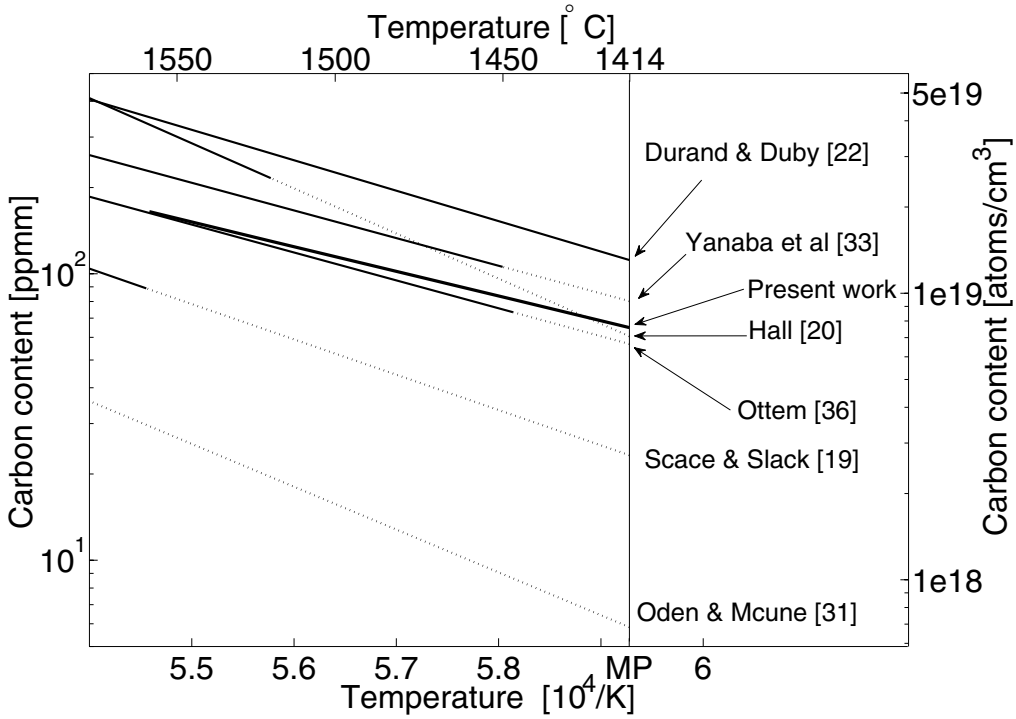

Figure 5.5: Solubility of carbon in liquid silicon as a function of temperature; a comparison with previously reported results. The heaviest line represents the present work, the other lines are marked with their references number. Dotted lines indicate extrapolations beyond the temperature regions in which the experiments were run.

published equation gives a higher solubility at 1414 °C compared to any of the publications on which they base their review.

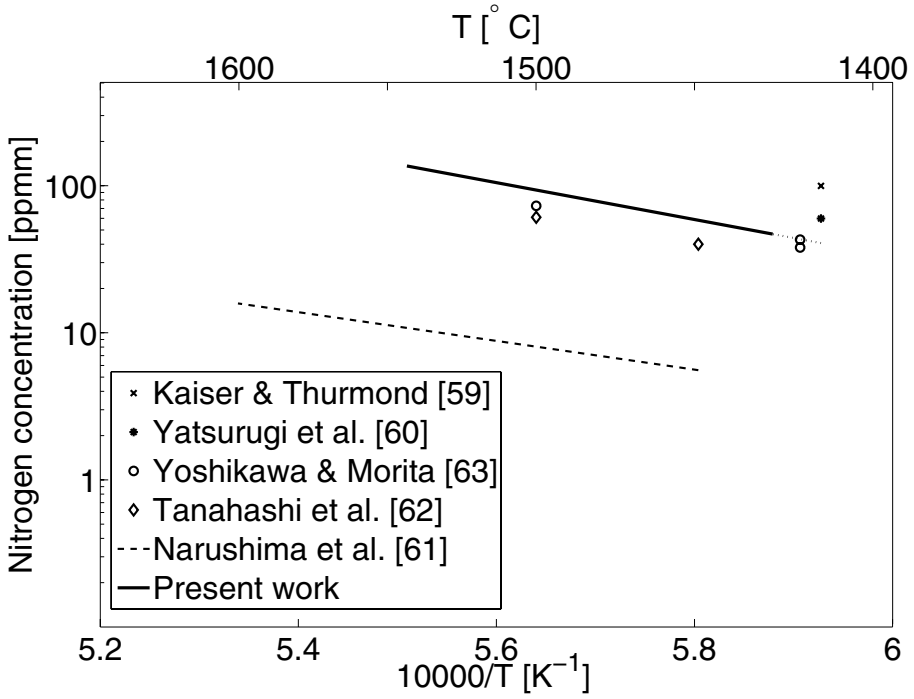

Figure 5.6: Comparison of the obtained nitrogen solubility results with previously reported data from the literature. The dotted line indicates the extrapolation of the present work to the melting point of silicon.

Si–N

The temperature dependency of the solubility of nitrogen in liquid silicon was found to be described by the following Arrhenius equation

between 1428 and 1542 °C:

$$C_N(T) = 1.0484 \cdot 10^5 exp\left(\frac{-28841}{T}\right) \tag{4.5}$$

Figure 5.6 shows an inverse temperature plot of this equation together with previously reported solubility data from the literature. The results of the present work are in reasonable agreement with much of the previously published data [60, 62, 63], but differs from the results of Kaiser and Thurmond [59] by a factor of approximately two and from the data of Narushima et al. [61] by a factor of almost ten.

Kaiser and Thurmond indicated the occurrence of active nitrogen in their experiments, and reported an increased reaction rate in the presence of this higher activity nitrogen. [59] As pointed out by Narushima et al. [61], this increased activity of the active nitrogen could be the reason behind the high levels of solubility. On their own part, Narushima et al. argue the validity of their results based on an enthalpy consideration. Having previously found a correlation between the enthalpy of dissolution of oxygen in a metal and the enthalpy of formation of the corresponding metal oxide [66], they attempt to demonstrate a similar relationship in the case of nitrogen. They do concede that there is too little data available to quantify the relationship, but express increased confidence in their own results as there appear to be a qualitative trend. When calculated from an equation describing the solubility as a function of temperature however, the enthalpy of dissolution does not depend on the absolute value of the solubility, but rather on the term describing its evolution with temperature. Thus the solubility data could be wrong by several orders of magnitude, yet from the enthalpy argument they should be considered sound.

Time evolution of the impurity content

The carbon and nitrogen content of the silicon melt were not found to be time dependent during the sampling period. This means that the solubility limit is reached within the initial three minutes at a given temperature. In other words, SiC and Si_3N_4 will dissolve very rapidly when in contact with molten silicon. In fact for nitrogen, the dissolution of Si_3N_4 was found to be fast enough to completely dominate the transport of nitrogen through the gas phase.

Taking the dimensions of the current experimental set-up into account, the following conservative conclusion can be drawn: Any silicon melt in contact with SiC or Si_3N_4 will be saturated with carbon/nitrogen at least in the region within ∼2 cm of the SiC/Si_3N_4 within three minutes.

This conclusion assumes the slowest possible saturation velocity that explains the observation of no time dependence of the carbon and nitrogen content after three minutes in a crucible with diameter ∼2 cm. Of course, a higher saturation velocity is also consistent with these observations.

5.2.2 Dissolution energies of carbon and nitrogen in silicon.

The dissolution of carbon and nitrogen in liquid silicon can be expressed as the following sums of reactions:

$$C(s) + Si(l) \rightleftharpoons SiC(s) \tag{5.5}$$

$$-(\underline{C}(l) + Si(l) \rightleftharpoons SiC(s)) \tag{5.6}$$

$$C(s) \rightleftharpoons \underline{C}(l) \tag{5.7}$$

$$\begin{array}{rcll} (1/4)\left[3Si(l) + 2N_2(g)\right. & \rightleftharpoons & \left.Si_3N_4(s)\right] & (5.8) \\ +(1/4)\left[Si_3N_4(s)\right. & \rightleftharpoons & \left.3Si(l) + 4\underline{N}(l)\right] & (3.2) \\ \hline (1/2)N_2(g) & \rightleftharpoons & \underline{N}(l) & (5.9) \end{array}$$

Since the silicon, silicon carbide and silicon nitride phases in these cases are virtually pure, the derivation outlined in section 2.2.4 is justified, and the dissolution energies can be calculated from equation 2.34:

$$\Delta G_C^{diss} = \Delta G_{SiC}^f - RT \ln\left(C_C(T)\right) \quad (5.10)$$

$$\Delta G_N^{diss} = (1/4)\left(RT \ln\left[(C_N(T))^4\right] - \Delta G_{Si_3N_4}^f\right) \quad (5.11)$$

The tabulated energy of formation of silicon carbide in Joules per mol is [96]:

$$\Delta G_{SiC}^f = -1.13 \cdot 10^5 - 11.4T \log T + 75.7T \quad (5.12)$$

Thus by combining this expression with equation 4.2, one obtains

$$\Delta G_C^{diss} = 4.6 \cdot 10^4 - 11.4T \log T + 23.2T \quad (5.13)$$

for the dissolution energy of carbon. This expression is valid between 1414 and 1559 °C. When it is extrapolated to the melting point of silicon, it gives the dissolution energy of carbon as 23.2 kJ/mol. Yanaba et al. found 20.4 kJ/mol for the same value [33].

Similarly, starting with the expression for the energy of formation of silicon nitride [96]:

$$\Delta G_{Si_3N_4}^f = -8.74 \times 10^5 + 405T \quad (5.14)$$

and combining it with equation 4.5, the dissolution energy of nitrogen between 1428 and 1542 °C—in Joules per mol—is found as:

$$\Delta G_N^{diss} = -1.59 \times 10^4 + 77T \quad (5.15)$$

At the melting point of silicon, this equation gives a dissolution energy of 28.3 kJ/mol. Narushima et al. [61] used a similar derivation to obtain an analogous expression. Their work points to a dissolution energy of 67.5 kJ/mol at the melting point.

5.2.3 Carbon and nitrogen in the production of silicon for solar cells

Carbon in the production of silicon

In the present work, a melt in contact with SiC was found to be saturated with carbon within minutes. However, the ratio of the SiC-surface to the silicon volume was quite large due to the small scale of the experiments.

In a larger furnace, the time it takes silicon to become saturated will obviously be longer, but how much longer is difficult to gauge. The convection in the melt will naturally play an important role; if sufficient mixing is provided saturation should occur rapidly even for larger melt volumes. At low convection rates the impurity transport will be determined by the rate of diffusion of carbon in liquid silicon. In the industrial casting of multi-crystalline silicon ingots, the melt will not be in direct contact with SiC, so the rate of saturation of the melt will not be a concern.

As was mentioned in the introductory chapters, carbon can enter the melt as CO gas that may form when SiO-gas from the quartz crucible reacts with the graphite parts of the furnace. Thus the carbon saturation of an industrial silicon melt depends on atmospheric conditions such as the gas-flow pattern of the furnace, rather than the reaction speed of SiC dissolution.

A carbon-rich silicon melt that undergoes directional solidification will continually be enriched with carbon due to the low distribution coefficient. [24, 25, 27, 30] From the results of Nozaki et al. [27], Kolbesen

and Mühlbauer [30], and from Kolbesen and Mühlbauer's interpretation of the data of Nozaki et al., a carbon distribution coefficient in the region of 0.06 seems reasonable. Using this value with the 66 ppmm solubility limit found for the liquid phase in the current work yields a solid solubility of approximately 4 ppmm.

Figure 5.7 shows the theoretical expected distribution of dissolved carbon during directional solidification for different starting concentrations of carbon assuming a liquid solubility of 66 ppmm, a solid solubility of 4 ppmm and a distribution coefficient of 0.06. It is also assumed that all solid forms evenly on a flat solid-liquid interface (i.e. no precipitation in the melt), that there is perfect and complete mixing in the liquid phase and that there is no diffusion in the solid phase. Finally, solidification is assumed to occur under equilibrium conditions, and no metastable phases are considered. The figure shows the carbon concentration as a function of ingot height for the case of a starting carbon concentration of 2, 30 and 80 ppmm respectively.

Looking at the low-carbon case in which the melt has a pre-solidification carbon content of 2 ppmm, the blue curve in Figure 5.7 illustrates how the dissolved carbon follows a Scheil distribution in the lower 95 % of the ingot, and that the solid solubility limit of 4 ppmm is not surpassed in this region. A calculation reveals that the SiC saturation limit is reached when 97.6 % of the ingot is solidified, and an integration of the Scheil equation from this point to the top of the ingot yields an average concentration of carbon in the form of SiC in the ingot of 1.5 ppmm (corresponding to an SiC concentration of 5 ppmm), while an average of 0.5 ppmm exists as substitutional carbon.

In the intermediate case of 30 ppmm carbon, the situation in principle is the same as for the 2 ppmm case, except that saturation occurs much sooner in the solidification process as seen from the red curve in Figure 5.7. The amount of dissolved carbon is seen to increase with ingot height, following the Scheil distribution to just under 60 % solidification after which it is constant, as it cannot increase past the

saturation limit in the solid. From this point in the casting process, the solidification proceeds by a eutectic reaction. The melt has a carbon concentration of 66 ppmm, so if 4 ppmm is incorporated in the solid silicon phase, from this point in the solidification there is a concentration of carbon in the form of SiC of 62 ppmm which is equivalent to an SiC concentration of 207 ppmm. Calculations reveal that the exact point of saturation is 56.8 % of the ingot height and the average concentration of substitutionally dissolved carbon across the entire ingot is 3.2 ppmm. The concentration of carbon present as SiC averages 26.8 ppmm across the ingot, corresponding to an SiC concentration of 89.4 ppmm.

The final case—described by the green curve in Figure 5.7—represents a case in which the carbon content in the liquid is greater than the melting point saturation level. In this case, as the temperature drops (from some point above 1444 °C, where equation 4.2 gives the solubility of carbon as 80 ppmm) towards the melting point of silicon, SiC will be the first solid to form. With the assumption stated above that all solid forms on the solid-liquid interface, this means that a thin SiC layer will form at the very bottom of the ingot. This is indicated by the green curve in the figure displaying a zero concentration of dissolved carbon near 0% solidification. Once enough SiC has formed to reduce the carbon content of the melt to 66 ppmm, solidification will proceed through the eutectic reaction as stated above. The amount of carbon in dissolved form and as SiC remains constant throughout the ingot, except in the negligibly thin SiC layer at the bottom. This layer corresponds to 14 ppmm of carbon, while the SiC distributed throughout the ingot represents 62 ppmm. The total SiC concentration in this case is 253.8 ppmm.

In reality, the carbon distribution will not be exactly as described by Figure 5.7. Since carbon can enter and leave the melt via the gas phase, the total amount of carbon will not remain constant during the entire solidification process. If solidification starts prior to carbon

saturation versus the gas phase, more carbon will enter the melt as long as it is not saturated with carbon. This will cause the carbon content in these regions of the ingot to be higher than what is predicted by Figure 5.7. If the carbon content is higher than the saturation limit against the gas phase however, the extra carbon that is expelled into the liquid from the solidifying crystal can leave the melt through the gas phase, leading to an overestimation of the carbon content in the upper regions of the ingot.

In addition, the precipitation of SiC will not occur immediately upon carbon saturation. Due to nucleation kinetics, some supersaturation is necessary in order to initiate the process so that the onset of SiC formation will happen at a later point than what is predicted by Figure 5.7. This also means that the maximum amount of dissolved carbon in the solid may be slightly higher than the saturation limit. If the solid is supersaturated with carbon, it is of course possible that the extra carbon will form SiC during cooldown, either by precipitating in the solid or by diffusing to already formed precipitates.

During directional solidification, the mixing in the liquid will not be perfect: there will be a build-up of carbon immediately in front of the solidification front where the carbon concentration is higher than in the bulk of the liquid. Thus, precipitates may form in this region even though the amount of carbon super saturation in the bulk of the melt is not sufficient to initiate nucleation. In fact, it is possible that nucleation and precipitation can occur in the boundary region of a casting in which the bulk concentration of carbon in the melt never reaches saturation levels.

To some extent the precipitates will be pushed upwards by the advancing solidification front and to some extent be incorporated by it depending on the particle size and the velocity of the solidification front. At a given velocity, particles larger than a critical size will be engulfed while the smaller ones will be pushed. The critical particle size decreases with increasing solidification velocity, meaning that

more particles are engulfed at higher growth velocities. Thus, compared with Figure 5.7, the SiC particles will be found higher up in the finished ingot than expected, and this effect will be more pronounced at lower solidification velocities.

As carbon continues to enter the melt after the onset of SiC-nucleation, the growth of already existing precipitates will be kinetically favoured over the nucleation of fresh particles. Therefore, if a particle forms in the boundary region, it will continue to grow as long as it is being pushed by the solidification front. However, as it grows the chance of it being engulfed by the solidification front increases. An SiC particle that is in the process of being incorporated by the solid will be straddling the solid-liquid interface. In this position, it will still serve as a favourable growth substrate for SiC-formation in the liquid, although it will quickly be completely engulfed by the solid. It seems plausible that as SiC continues to grow from this precipitate during and after its engulfment, this can lead to the formation of SiC in its filament form, growing in the direction of solidification.

Taking into account the various effects just discussed, the qualitative trends of the carbon distribution in a real casting can be summed up as follows: The final ingot can be expected to show an increase in carbon content with ingot height throughout the ingot, with the prevalence and size of SiC precipitates also increasing towards the top of the ingot. A higher starting concentration of carbon will also lead to SiC formation at an earlier stage in the solidification process and of course to larger overall amounts of carbon and SiC.

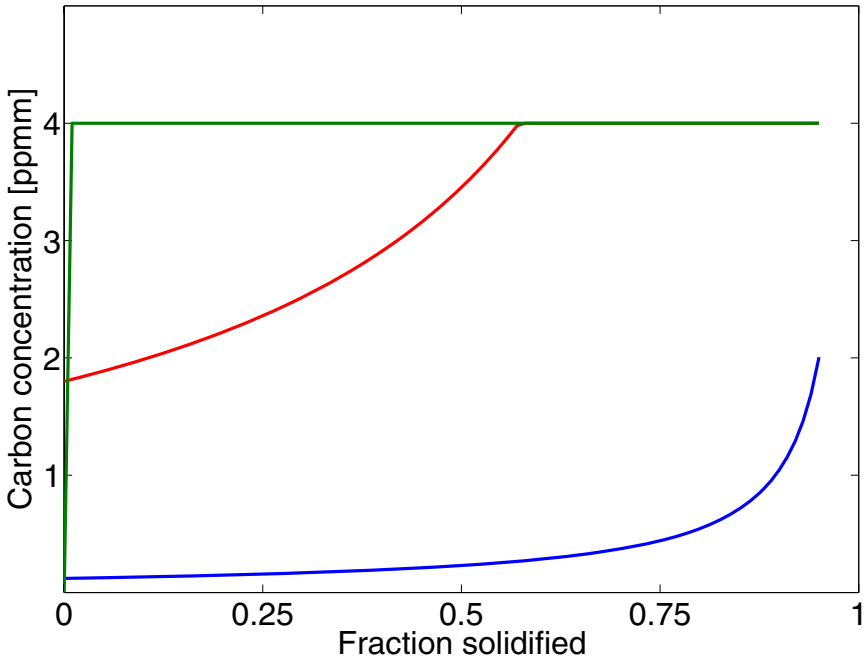

Figure 5.7: Theoretical distribution of substitutionally dissolved carbon in a directionally solidified ingot as a function of ingot height. The curves show the situation for different starting concentrations of carbon: 2 ppmm (blue curve), 30 ppmm (red curve) and 80 ppmm (green curve).

Nitrogen in the production of silicon

The situation for nitrogen is similar to that of carbon in many respects, but a main difference is that in industrial situations molten silicon will commonly be in direct contact with Si_3N_4, as this is used to coat the SiO_2 crucibles in which the solidification process takes place.

In the current work, it was observed that a $\sim$75 g melt held in a $\sim$2 cm diameter crucible was saturated within three minutes at the most. This rapid dissolution must also be expected to take place on the industrial scale, but the exact time it takes for saturation to take place will depend on how quickly the dissolved nitrogen is transported away from the locally saturated regions near the crucible walls. In an industrial setting, an induction furnace is likely to be used in which case the convection can be expected to be greater than in the present work.

A crude estimate can be made by comparing the mass to surface area ratio of the two cases. In the current work, 75 g of silicon was melted in a 18 mm radius crucible. Assuming a liquid silicon density of 2.57 gm/cm^3, this implies a contact area of 42 cm^2 and a mass to surface area ratio of 1.79.

A 250 kg industrial melt—assumed cubic for simplicity—will have a contact area of approximately 10^4 cm^2 and a mass to surface area ratio of 25.

Assuming a linear dependence on the mass to area ratio, the industrial ingot will be saturated after $(25/1.79)\cdot 3$ min$\approx$42 min.

Thus, if the saturation time depends linearly on the surface to mass-ratio, an industrial melt can also be assumed to be saturated at the start of solidification. If the dependence is quadratic however, the saturation time will be close to ten hours.

Whether it will take 42 minutes or 10 hours to saturate a specific melt will depend on various furnace-specific properties. As mentioned in the above discussion concerning carbon, the convection of the melt

and the diffusion of nitrogen will play a key role.

The melting and solidification step in industry will naturally vary from furnace to furnace, but a combined process time of more than 24 hrs. for both processes is typical. This means that even at the high end of the estimate of the saturation time, the melt will be expected to be saturated before the end of solidification.

The description of nitrogen during solidification has many parallels to that of carbon. Under equilibrium conditions, Si_3N_4 will form upon saturation of the melt, while in reality some degree of supersaturation is required. There will again be a region of increased nitrogen concentration immediately in front of the solidification front, where it is possible that Si_3N_4 may form even though the prerequisites for precipitation are not fulfilled in the bulk of the liquid.

If precipitates do form in the liquid, they will once again be subjected to pushing and engulfing by the solidification front. They will also grow as more nitrogen is expelled into the liquid, increasing the chance of engulfment as they become bigger.

While nitrogen will not enter the melt via the gas-phase like carbon, it has the opportunity to leave the melt as N_2. In the present work, the dissolution of Si_3N_4 was seen to dominate the gas-phase transport, but again this may depend heavily on the contact-area to volume ratio, and also on the ratio between the melt volume and the gas-liquid interface.

In either case, it is clear that nitrogen will not follow the Scheil distribution, as the total amount of nitrogen in the silicon will not remain constant and there are strong possibilities of particle formation. As is the case for carbon however, it is to be expected that the constant enrichment of the melt coupled with the formation and pushing of Si_3N_4 particles will lead to a nitrogen distribution that increases towards the top of the ingot. The frequency and size of Si_3N_4 particles can also be expected to increase with ingot height.

5.3 The interactions of carbon, nitrogen and boron in liquid silicon

Having discussed the behaviour of carbon, nitrogen and boron in pure silicon, the focus of the next section will be on silicon melts with more than one of these elements present and how the elements interact.

5.3.1 Carbon-nitrogen interactions in liquid silicon

The results obtained from a melt simultaneously saturated with carbon and nitrogen were described in section 4.2.4. The Arrhenius equations describing the carbon solubility during nitrogen saturation and the nitrogen solubility during carbon saturation are plotted in Figure 4.9, and table 5.2 summarises some of the predictions they make regarding solubilities at 1414°C, 1450°C and 1500°C.

Table 5.2: The solubilities of carbon and nitrogen in liquid silicon in the binary and ternary systems.

System	Carbon content						Nitrogen content					
	Temperature						Temperature					
	1414°C		1450°C		1500°C		1414°C		1450°C		1500°C	
Si-C	66	±9	83	±12	114	±16						
Si-N							39	±8	56	±11	90	±18
Si-C-N	79	±12	92	±14	111	±17	51	±2	69	±3	103	±4

It is evident that the solubilities of both carbon and nitrogen increase during simultaneous saturation, meaning that the interaction coefficients e_C^N and e_N^C are negative.

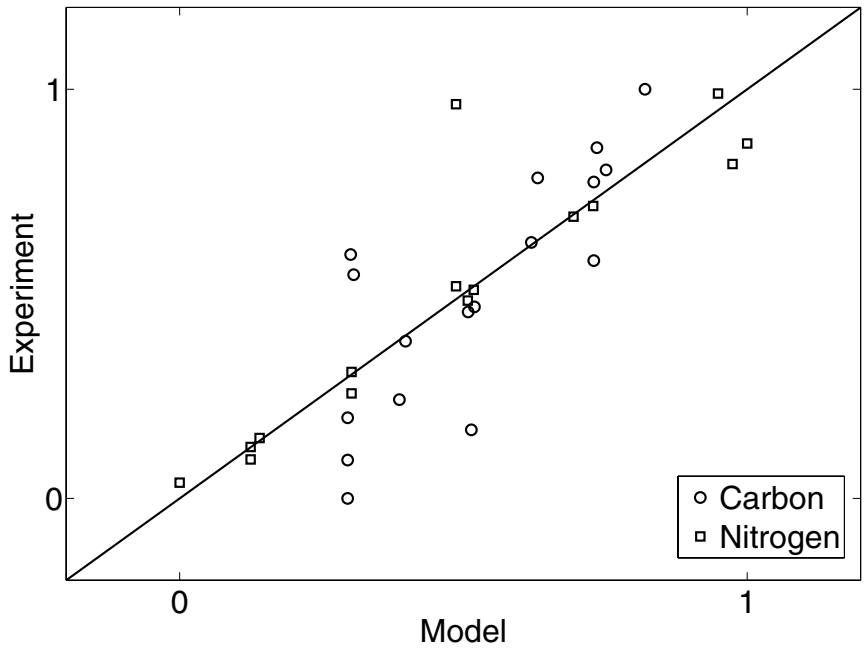

Figure 5.8: Comparison of the experimental and modelled solubility levels for carbon and nitrogen during simultaneous saturation. All data have been scaled to a value between zero and unity using equation 5.20

As outlined in section 2.2.5, the solubility of a solute in silicon as a function of temperature and the concentration of one other solute can be described by equation 2.40. In the case of the carbon solubility in a nitrogen enriched silicon melt the equation of interest will be

$$C_C(T, C_N) = A_C \cdot \exp\left\{\frac{-B_C}{T} - \ln(10) \cdot \left[e_C^N \cdot C_N\right]\right\} \tag{5.16}$$

while for nitrogen the equation becomes:

$$C_N(T, C_C) = A_N \cdot \exp\left\{\frac{-B_N}{T} - \ln(10) \cdot \left[e_N^C \cdot C_C\right]\right\} \tag{5.17}$$

Here, A_C, B_C, A_N and B_N are the coefficients from the Arrhenius equations describing the solubility levels in the pure Si–C and Si–N systems and are known from equations 4.5 and 4.8. Since the interaction parameters are linked by $e_N^C = (M_N/M_C) \cdot e_C^N$ from equation 2.20 and the temperature dependence of the interaction parameters follows $e = \alpha + \beta/T$, there are two parameters that need to be determined through a fitting of the experimental data.

The extracted samples were all analysed for carbon or nitrogen only. Therefore, in the fitting of the data, the concentration of the element that was not measured for each sample was calculated using the found Arrhenius equations 4.6 and 4.7. Using the method of least squares, the best fit of the experimental data results in:

$$e_N^C = 110.83 - 207123/T \tag{5.18}$$

$$e_C^N = 95.01 - 177555/T \tag{5.19}$$

These equations are valid between 1422 and 1525 °C. Figure 5.8 compares the values predicted by the model with those found experimentally. For the purpose of this plot, the experimental and modelled

values were all scaled to a value between zero and unity by the following formula:

$$C'_x = \frac{C_x - C_x^{min}}{C_x^{max} - C_x^{min}} \tag{5.20}$$

Here C_x^{min} and C_x^{max} are the minimum and maximum of all modelled and experimental values for element x. In the case of a perfect fit, such a plot would show all points along the line $x = y$. The data points in the present case are clearly seen to follow this general trend, albeit with some scatter.

Using equations 5.18 and 5.19 in equation 5.16 and 5.17, one obtains expressions showing the solubility of carbon as a function of temperature and nitrogen content, as well as the nitrogen solubility as a function of temperature and carbon content in the temperature range between 1422–1525 °C:

$$C_C(T, C_N) = 7.37 \cdot \exp\left\{\frac{-11731}{T} - \ln(10) \cdot [(95.01 - 177555/T) \cdot C_N]\right\} \tag{5.21}$$

$$C_N(T, C_C) = 104840 \cdot \exp\left\{\frac{-28841}{T} - \ln(10) \cdot [(110.83 - 207123/T) \cdot C_C]\right\} \tag{5.22}$$

Assuming only first-order interactions, these equations will be valid up to the saturation limit of the secondary impurity. They are therefore useful for calculating the solubility limit of carbon or nitrogen in situations where the other element is present in small and known quantities. One example could be the estimation of the carbon content in silicon melted in a graphite crucible in a nitrogen free environment when the silicon feedstock contains a known amount of nitrogen.

In the situation where the melt is simultaneously saturated with both carbon and nitrogen, such as is the case in the experimental

set-up of the current work, the equations cannot be used so straightforwardly, since the carbon saturation limit depends on the nitrogen saturation limit and vice versa. At a given temperature, one basically has to find the solutions to a set of equations in the form of:

$$C_C = a \cdot \exp(b \cdot C_N) \tag{5.23}$$
$$C_N = c \cdot \exp(d \cdot C_C) \tag{5.24}$$

which cannot be done analytically. Thus, a numerical or iterative solution method must be employed. An iterative solution method was chosen in the present work, and the resulting solubility limits are plotted in Figure 5.9. It can be seen that the solubility limits depend almost linearly on temperature. Therefore, linear approximations were constructed for the solubility of carbon and nitrogen as functions of temperature during simultaneous saturation:

$$C_C^{N_{sat}} = 3.80 \cdot 10^{-5} T - 5.62 \cdot 10^{-2} \tag{5.25}$$
$$C_N^{C_{sat}} = 7.03 \cdot 10^{-5} T - 0.114 \tag{5.26}$$

These approximations are valid in the temperature regime of the current work, i.e. between 1422–1525 °C. The R^2 between the linear and non-linear model was greater than 0.99 in both regressions.

Looking at Figure 5.9, it can be seen that the nitrogen solubility becomes greater than the carbon solubility at around 1515 °C. This is a result of working with mass as the measure of quantity, as in this case the interaction coefficient depends on the ratio of molar masses. Thus, the effect of carbon on nitrogen solubility will be greater than the effect of nitrogen on the solubility of carbon. If the solubility is defined in terms of the number of atoms, the lines in Figure 5.9 would never cross.

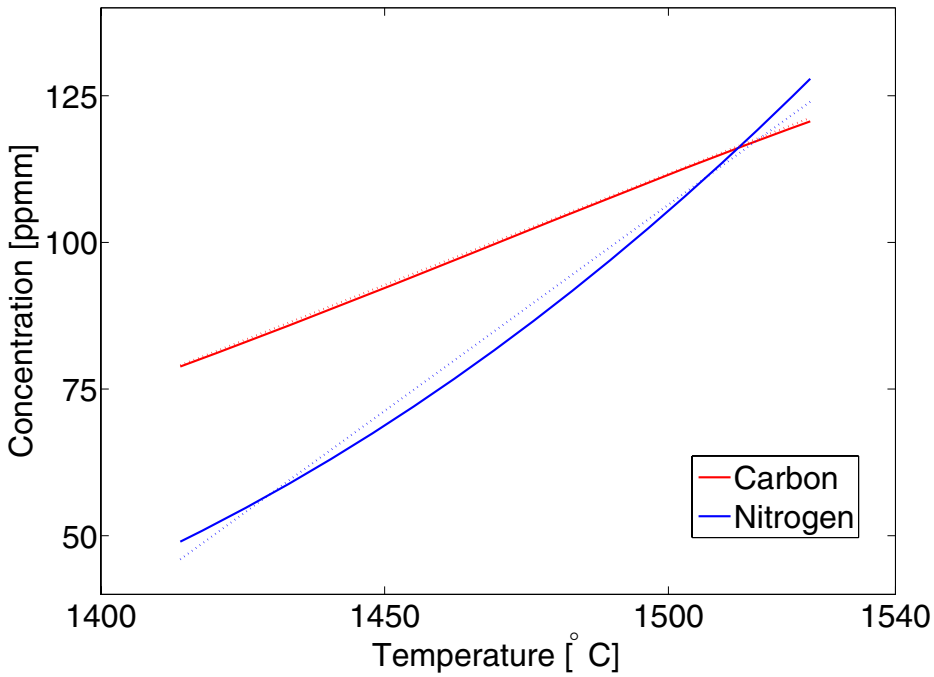

Figure 5.9: Solubility limits of carbon and nitrogen as functions of temperature during simultaneous saturation in liquid silicon. The solid curves represent the iterative solutions of equations 5.21 and 5.22 at each temperature, while the dashed lines represent the linear approximations to these solutions given by equations 5.25 and 5.26.

Table 5.3: Carbon levels at certain temperatures and boron levels as predicted by Arrhenius equations fitted for each boron level.

Boron-addition	Temperature					
	1414°C		1450°C		1500°C	
0	66	±9	83	±12	114	±16
0.25 %	78	±11	98	±14	134	±20
0.50 %	74	±7	94	±8	128	±11
1.00 %	92	±8	117	±10	159	±14
1.50 %	102	±12	129	±16	176	±21
2.00 %	110	±7	139	±9	189	±12

5.3.2 Carbon-boron interactions in liquid silicon

The carbon content in the samples extracted from liquid silicon with boron additions was higher than what was found in the pure Si–C-system. Figure 4.11 shows the Arrhenius equations describing the found carbon content for various boron additions, and table 5.3 summarises the solubility levels as predicted by these equations at 1414°C, 1450°C and 1500°C, respectively.

Similar to the carbon–nitrogen interaction described above, the increase in solubility with the addition of boron indicates a negative interaction parameter e_C^B. Again, the carbon solubility can be described by an equation in the form of equation 2.40:

$$C_C(T, C_B) = A_C \cdot \exp\left\{\frac{-B_C}{T} - \ln(10) \cdot \left[e_C^B \cdot C_B\right]\right\} \tag{5.27}$$

Since A_C and B_C are given from equation 4.2 and the temperature dependency of e_C^B follows $\alpha + \beta/T$, two parameters need to be determined in the fitting of the experimental data. Using the method of least squares, the boron–carbon interaction coefficient was determined

as:

$$e_C^B = -0.15 + 51.6/T \tag{5.28}$$

Inserting this expression into equation 5.27, an explicit expression for the carbon solubility as a function of both temperature and boron level is obtained:

$$C_C(T, C_B) = 482.84 \cdot \exp\left\{-\frac{18897}{T} - \ln(10) \cdot [(-0.15 + 51.6/T) \cdot C_B]\right\} \tag{5.29}$$

Both equation 5.28 and equation 5.29 are valid between 1422 and 1542 °C. Figure 5.10 shows the experimental data from the Si–C–B-system together with the predicted solubility values calculated from this equation. As in the previous section, all data is scaled to a value between 0 and 1 using equation 5.20. The model is seen to agree well with the experimental points.

Equation 5.29 predicts a negative e_C^B for all temperatures in the liquid range of silicon. This is at variance with the results of Yanaba et al. [79] who found an expression (Eqn. 2.4) indicating a positive interaction parameter above 1982 °C. Figure 5.11 shows a comparison of the current results with those found by Yanaba et al. Figure 5.11(a) shows a comparison in the temperature region of experimentation, while figure 5.11(b) illustrates the differences in high temperature predictions. It is apparent that the two predictions are within reasonable agreement at low temperatures, but then diverge rather rapidly at higher temperatures. A positive interaction parameter as predicted by the model of Yanaba et al. at high temperatures would imply a decrease in carbon solubility with an increase in boron content.

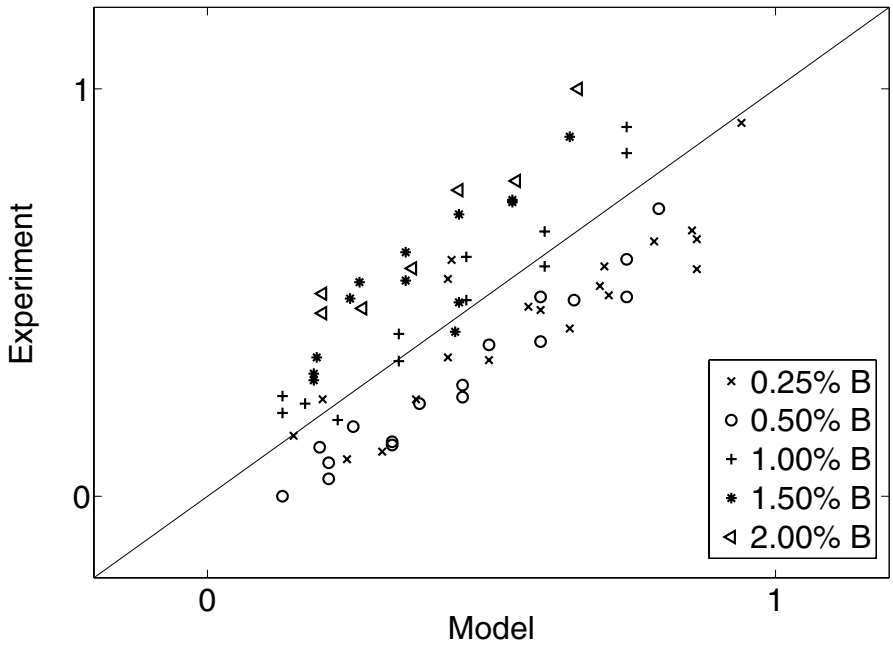

Figure 5.10: Comparison of modelled and experimental results from the Si–C–B-system. All data have been scaled to a value between zero and unity using equation 5.20.

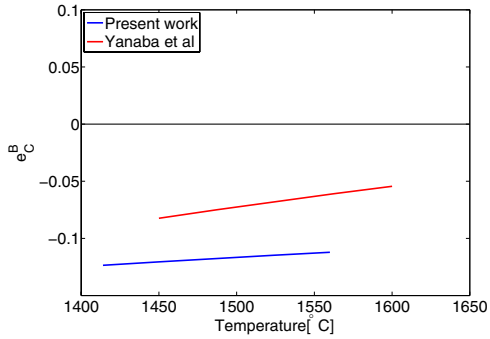

(a)

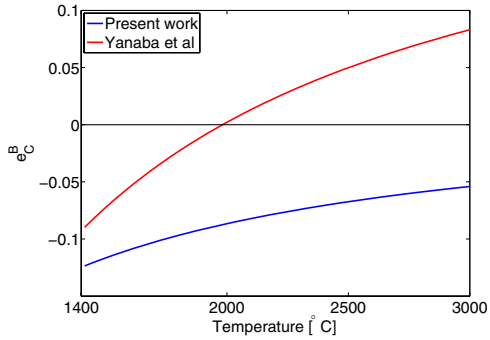

(b)

Figure 5.11: Comparison of the found carbon–boron interaction coefficient with the results of Yanaba et al. [79] a: Within the temperature regions of the respective experiments. b: Extrapolations to high temperatures.

5.3.3 Nitrogen-boron interactions in silicon

The nitrogen content of the extracted samples was seen to decrease significantly in the experiments with boron added to the melt when compared to the boron free experiments on the Si–N-system. There was also a significantly larger observed effect in the case of a 1.50 m.% boron addition compared to the 0.10 m.% addition. However, since it can be expected that BN had formed in the 1.50 m.% experiment, these two cases are not directly comparable. Therefore, in the following discussion of the BN-interactions the results from the two experiments are treated separately. First, the results from the 0.10 m.% experiment are discussed with respect to the N–B interaction coefficient, and then the results from the 1.50 m.% experiment are treated with respect to BN-formation.

The nitrogen-boron interaction coefficient

In the case of additions of 0.1 m.%B, the boron content is below the required limit for the precipitation of BN. The observed reduction of nitrogen content in the samples from this experiment can therefore be taken as an indication that e_N^B—the boron–nitrogen interaction coefficient in silicon—is positive. Using only the data from the Si-N-B-1 experiment, the nitrogen-boron interaction coefficient can be calculated as

$$e_N^B = -6.9 + 13532/T \tag{5.30}$$

meaning that it ranges from $\sim 1.1 - 0.6$ in the temperature range where the samples were extracted. This is in reasonable agreement with the estimates of Noguchi et al. [64] who calculated $e_N^B = 2.70$ based on their experiments with molten silicon held in a BN crucible at 1450 °C. Yoshikawa and Morita [63] observed an even greater effect of boron on nitrogen solubility, estimating the boron-nitrogen interaction

coefficient as $e_N^B = 7.1$, $e_N^B = 5.5$ and $e_N^B = 5.5$ at 1425, 1450 and 1500°C respectively.

The equation for the solubility of nitrogen in liquid silicon as a function of temperature and boron level becomes:

$$C_N(T, C_B) = 104840 \cdot \exp\left\{\frac{-28841}{T} - \ln(10) \cdot [(-6.9 + 13532/T) \cdot C_B]\right\} \tag{5.31}$$

BN precipitation in a nitrogen saturated silicon melt

Based on the work of Noguchi et al. [64], boron additions of 1.5 m.% should be expected to lead to the formation of BN precipitates.

Considering the Si(l)–Si_3N_4-equilibrium in theoretical terms, as boron is added a three-phase equilibrium Si(l)–Si_3N_4–BN is immediately established, although no BN will be present while the boron content remains low. Because of the positive interaction coefficient, nitrogen solubility will decrease due to the presence of boron. This decrease in nitrogen solubility will continue with increasing boron additions until the boron saturation limit is reached and BN is formed. At this point, further boron additions will cause the creation of more BN, and theoretically the boron content of the melt should remain unchanged. Hence, boron additions above the solubility limit of BN should not influence nitrogen solubility.

As Figure 4.12 shows however, there is a decrease in the nitrogen content when going from 0.1 to 1.5 m.% boron addition.

If BN did form in the Si-B-N-2 experiments, it could form as precipitates in the melt or along the crucible wall, where nucleation sites could exist as roughness on the crucible walls. If BN precipitates in the melt formed in significant amounts, this would cause the measured nitrogen levels of the extracted samples to be overestimated, as both the dissolved nitrogen and the nitrogen in the form of BN would

be taken into account. If BN instead formed on the crucible walls, the nitrogen levels measured in extracted liquid samples would not be directly influenced, although the boron levels would be significantly lower than what was added to the melt.

In the present work, the measured boron content of the sample from Si-B-N-2 was reasonably close to the amount added to the melt, while the measured nitrogen levels were in the ppm-range. This indicates that most of the boron in the melt did not exist as BN at high temperatures.

The microprobe image shown in Figure 4.13 agrees with this assessment. The chemical analysis of the grey phase is consistent with it being a silicon boride. However, due to the small spatial extent of these regions compared to the beam diameter of the microprobe analyser, a quantitative analysis of the exact stoichiometric form of boride is impossible. The grey phase has formed elongated regions with a thickness on the order of a few tenths of a μm, while the beam diameter is ~ 1 μm. Therefore, depending on the thickness of the grey phase at the point of analysis, a considerable portion of the collected signal will come from the surrounding matrix. In addition, the beam penetrates several μm below the specimen surface which may again yield a signal from the silicon matrix.

However, due to the large amounts of grey phase observed and the low amount of other elements present in the system, it must be assumed to be a silicon boride. As the sample was rapidly solidified from temperatures above 1414°C, it is probable that the boride in question is SiB_6 which has formed in a eutectic reaction upon the solidification of the sample. SiB_6 is the stable boride around the melting point of silicon, and it is likely that it has remained in this form throughout the cooling period even though SiB_3 is more stable at room temperature.

The exact form of boride is not important however. Whether it is SiB_6 or SiB_3 its presence necessitates the conclusion that most of the added boron existed as dissolved boron in the melt. Had it existed as

boron nitride particles, these should still be found in this form after quenching and the nitrogen levels of the extracted samples would also be affected.

A possible explanation is that the melt is supersaturated and metastable due to some suppression of the formation of BN. The respective amounts of boron and nitrogen are different by several orders of magnitude: There will be around 1.50 m.% boron, but less than 50 ppmm nitrogen. This means that there are at least 250 boron atoms for each nitrogen atom. With so little nitrogen present, the agglomeration of sufficient amounts of boron and nitrogen may simply be too improbable to take place.

If BN precipitation could be proven to be completely suppressed, the results from Si-B-N-2 could be taken as being due to melt interactions between boron and nitrogen, and the results could be included in the above calculation of e_N^B.

However, if some BN does form, say on the order of a few ppm, this means that the measured nitrogen levels in the extracted samples are made up of both dissolved nitrogen and BN. In other words, the measured nitrogen levels would be too high, and e_N^B would be underestimated. BN at these levels would not be detectable in the microprobe images.

Figure 5.12 shows a plot of different estimates of e_N^B using different data sets. The first estimate is the one described by equation 5.30 using only data points from the Si-B-N-1 experiment. The other curve is produced using data from both Si-B-N-1 and Si-B-N-2. The abrupt change in temperature dependence, when including the high boron-level experiment, may be taken as an indication of a fundamental change to the investigated system, for example BN precipitation. Therefore, in the present work the results from Si-N-B-2 are not included in the final estimation of e_N^B, due to the suspected presence of BN. This experiment has shown that the formation of BN is strongly suppressed in a nitrogen-saturated silicon melt.

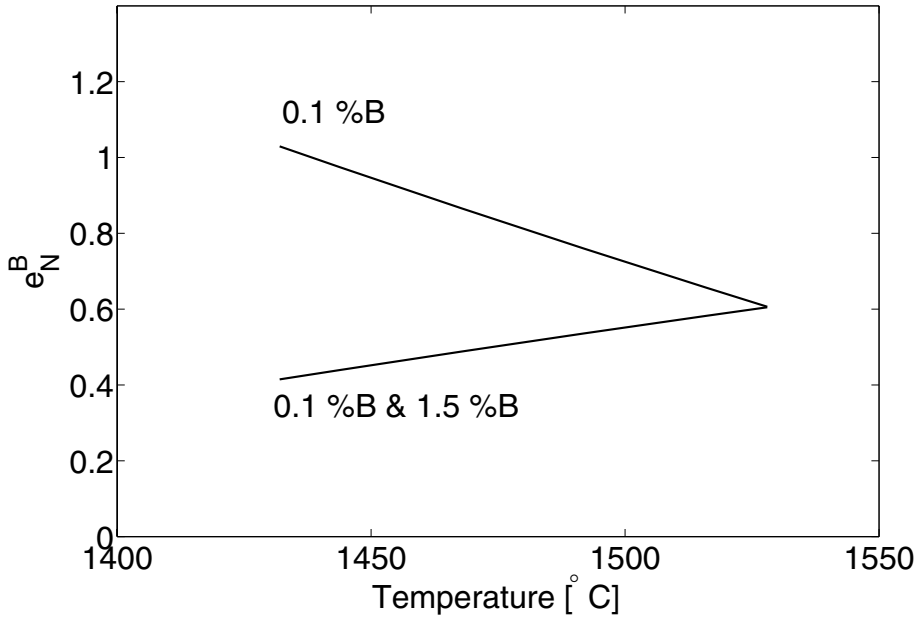

Figure 5.12: e_N^B computed using varying datasets. Each estimate includes all data up to a certain boron level. The first one only includes data from the 0.10 m.%B-experiment (Si-B-N-1) and the final one includes data from experiments with both 0.1 and 1.5 m.%B (i.e. Si-N-B-1 and Si-N-B-2), respectively.

5.3.4 The interactions between boron, carbon and nitrogen during the production of silicon solar cells

Carbon–nitrogen interactions

In the present work, it was shown that the carbon–nitrogen interactions in liquid silicon caused the solubility limits of both elements to increase significantly. In an industrial furnace during the directional solidification of silicon, this may have some impact on how carbon and nitrogen are distributed throughout the ingot.

A key effect of course is that increased saturation limits in the liquid allow for higher amounts of carbon and nitrogen to enter the melt, leading to higher total amounts spread out across the finished ingot.

Another important issue is whether the same effect is also present in the solid phase. If it is not, this means that the distribution coefficients of carbon and nitrogen are effectively lowered ($k_0 = C^s/C^l$), which would lead to a more "top heavy" distribution of carbon and nitrogen.

If the solubilities in the solid phase are also increased, the changes in the distribution coefficients will be determined by the ratio of the relative changes. If the relative change in the solid solubility is greater than the relative change in the liquid solubility, the distribution coefficient will increase. On the other hand, if the relative change is greater in the liquid phase, the distribution coefficient will decrease.

Unless there is a very large difference however in the relative effect on solubility, the effect on the distribution coefficient will be quite small. It will certainly still be within the same order of magnitude, meaning that the qualitative distributions from the single-element systems are retained.

The change in liquid solubility may also influence the formation of

SiC and Si_3N_4. If equilibrium conditions are assumed, the situation for each element will be as the single-element cases except that the precipitation will first be initiated at a later stage in the crystal growth process.

However, as in the single-element cases, some amount of supersaturation will be necessary to initiate precipitation. With two elements present, if the two elements reach saturation at around the same stage in the process, it is possible that some co-precipitation mechanism leads to a lower necessary degree of supersaturation.

If the situation is such that one element becomes saturated and forms precipitates at an earlier stage than the other element, the first precipitates to form can function as nucleation sites for the precipitation of the other element, significantly lowering the degree of supersaturation necessary for precipitation.

If precipitation is subject to either of these two mechanisms, the position in the ingot at which SiC and Si_3N_4 are first observed may not change much from the single element cases. As was mentioned in the introductory chapters, SiC and Si_3N_4 are frequently found clustered together in silicon, meaning that co-precipitation or a situation in which one type of precipitates serves as nucleation sites for the other is plausible.

In summary, the most obvious effect of the carbon–nitrogen interaction will be an increased total amount of both elements in the finished ingot due to the increased incorporation of dissolved carbon and nitrogen in the melt. The onset of SiC and Si_3N_4 formation may or may not happen at a later stage in the solidification process, depending on the effect of co-precipitation and seeding.

Carbon–boron and nitrogen–boron interactions

Using equation 5.29, the change in carbon solubility can be predicted for various boron additions. To investigate the effect of boron addi-

tions in the ranges typically encountered in the production and processing of solar grade silicon, the increase in carbon solubility was calculated at 1414 and 1600 °C for boron contents of 1 and 5 ppmm, respectively. The predicted additional solubility for these cases ranged from 2 to 27 ppbm.

Similarly, when feeding boron concentrations likely to occur in solar cell manufacturing into equation 5.31, the reduction in nitrogen solubility is found to amount to a trifle. For a boron addition of 1 ppmm for example, the model predicts a reduction in solubility of only 12 ppbm at 1450 °C, and even at temperatures as high as 1520 °C, a boron content of ∼50 ppmm is required for a reduction in nitrogen solubility of 1 ppmm. Thus, on the basis of the current work, the influence of boron on the carbon and nitrogen solubilities can be disregarded in industrial processes.

5.4 Uncertainty and reproducibility of the results

5.4.1 Random and systematic error

The model versus experimental plots in Figure 5.8 and Figure 5.10 both show a linear trend, albeit with some scatter. The reasons behind the scatter can be many and complex, but it is likely that the inherent difficulty of analysing low amounts of carbon in silicon plays a significant role. As discussed in the results-section, some data points deviate so much as to be defined as outliers. As previously mentioned, these outliers are probably caused by contamination. It is possible that certain other samples are also contaminated to a much smaller degree, and that this is a cause for some of the scatter.

It is likely that at least some aluminium is present in the melt because of the presence of alumina in the furnace interior and the thermocouple sheath. According to Yanaba et al. [79], an aluminium content of 0.1 %wt will increase the carbon solubility by ∼0.3 % at 1550 °C. An aluminium content of 0.1 %wt in a 75 g silicon melt corresponds to 0.075 g which would represent a noticeable consumption of alumina. No such consumption has been observed, and it is believed that the real aluminium content in the melt is far below 0.1 %wt and the effect on carbon solubility negligible.

Another concern is the oxygen content in the melt and samples. A few samples were analysed for oxygen content, and were found to contain between 29 and 90 ppmm of oxygen for temperatures between 1419 and 1520 °C. Figure 5.13 shows the oxygen measurements together with various estimates of the solubility limit of oxygen in liquid silicon from the literature.

It can be seen that oxygen levels are in the region of the solubility limit in liquid silicon. However, no SiO_2 particles have been observed

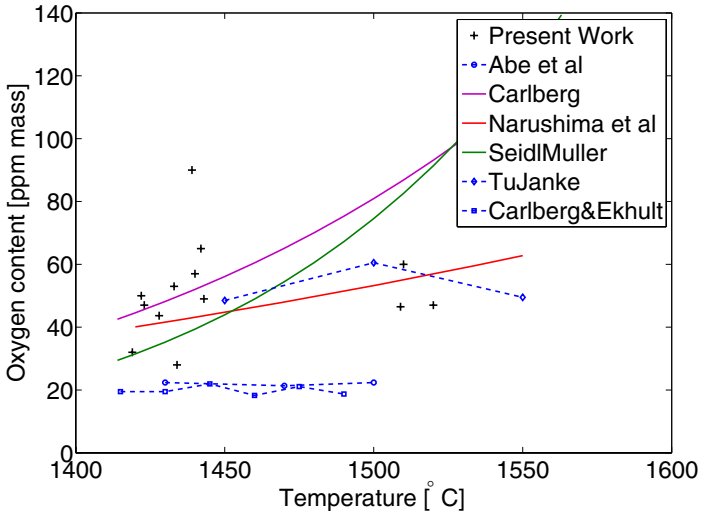

Figure 5.13: The oxygen content of analysed samples together with literature estimates of the solubility limit of oxygen in liquid silicon [97, 98, 66, 99, 100].

in the microprobe analysis of the samples. This can be due to a variety of reasons. The precipitation may be kinetically suppressed with the small supersaturation insufficient for free nucleation. Another possibility is that there is no supersaturation at all. There is a substantial spread in data both the experimental data from the current work and in the values from literature, meaning that sub-saturation levels of oxygen cannot be ruled out. A third possibility is that the silicon samples have increased their oxygen content once the liquid entered into the quartz tube, meaning that the true oxygen levels of the melt are lower than that measured in the samples. The main point however is that the oxygen level has been kept at a level at which there is no

precipitation of SiO_2.

The formation of SiO_2 at the Si-SiC interface could disturb the Si-SiC equilibrium. Furthermore, the presence of SiO_2 particles have been known to facilitate the precipitation of SiC particles, and no SiC-particles were detected in the samples. Of course, while nucleation could have been suppressed by a variety of effects, the lack of SiC substantiates the assumption that no SiO_2 particles are available in the melt to act as nucleation centres. When it comes to dissolved oxygen, Yanaba et al. [79] assumed that it did not influence the carbon solubility, and the database created by SINTEF [17] indeed predicts that an oxygen content of 50 ppmm will decrease the carbon solubility in the melt by only 0.12 %. Thus the oxygen levels in the current work does not significantly influence the carbon solubility and can be ignored.

5.4.2 Reproducibility of the results

The current discussion has been written with a view to communicate a set of conclusions. These conclusions were known at the outset of this writing, but obviously not at the outset of experimentation. The actual experimental process included more twists and turns than has perhaps been apparent from the—hopefully—linear description given in this text. This has been done to promote clarity and ease of understanding for the reader, although by not elaborating on the stepwise progress toward the final model, some issues on reproducibility have been lost. Therefore, in this section, I will present two of the intermediate models based on early results and show how they compare with later results.

The Si–C-system

The Si–C system was the first to be investigated, and the bulk of the data from this system represent the earliest results obtained in the tube furnace. The last experiment to be performed however was an experiment on the Si-C system in which nine samples were extracted between 1456 and 1525 °C. Five of these samples were analysed and found to show good agreement with the equation describing the carbon solubility as it stood at that time. The comparison of these data with the old carbon solubility equation is seen in Figure 5.14.

The new results are seen to compare favourably with the old equation, demonstrating reproducibility of the carbon solubility data. Since these data are taken from the very first and last experiments performed, it also demonstrates consistency in the apparatus over the period of experimentation.

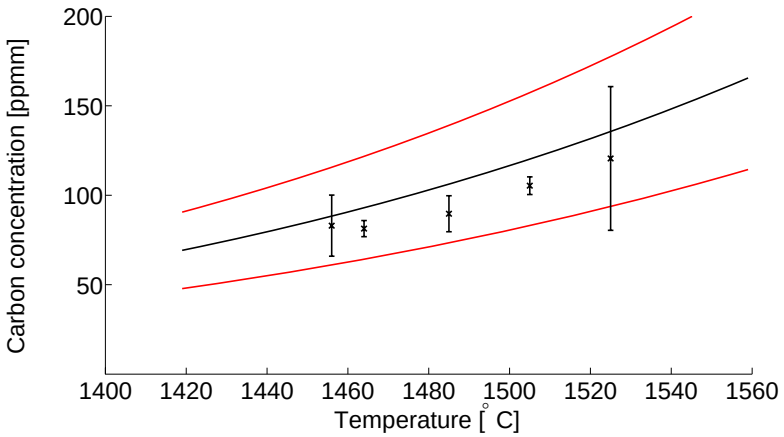

Figure 5.14: Comparison between the data from the last experiment performed on carbon solubility and the model equation based on the data available at the time of this experiment.

The Si–B–C-system

Among the final experiments performed were two additional experiments performed on the solubility of carbon with 0.25 wt% and 0.50 wt% boron additions. The first series of experimentation had shown higher carbon solubilities for 0.25 wt% as compared to 0.50 wt% boron, so these systems were therefore re-investigated.

31 samples were extracted, and 12 of these were analysed. These data are compared with the previously obtained data from the Si–B–C system with 0.25 and 0.50 wt% boron in Figure 5.15. The most recent results are seen to fall very much in the same area as the earlier results from these systems which are both plotted in Figure 5.15(a). It is not then not surprising, that the model based on the early results predicts the latest results rather well, as seen in Figure 5.15(b).

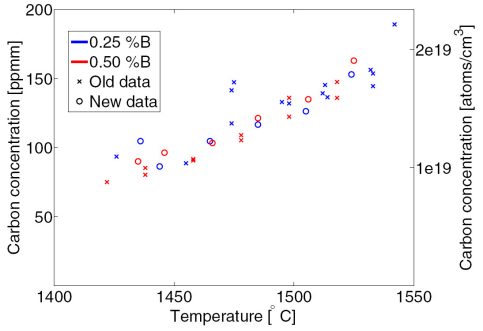

(a)

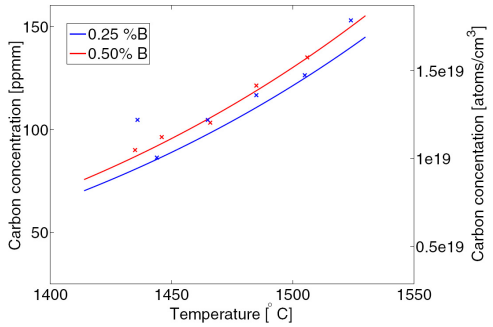

(b)

Figure 5.15: Comparison between the last two experiments performed on carbon solubility in the Si-B-C system and previous experiments performed in the same system. a: The data points obtained in early and later experiments with 0.25 and 0.50 wt% boron. b: The data points from the late experiments compared with the model equations derived from the earlier experiments.

Chapter 6

Conclusions

The silicon rich portion of the Si–C–N–B-system has been experimentally investigated in terms of solution thermodynamics in the temperature range between 1414-1560 °C. The main experimental work has been performed in a small, resistance heated tube furnace, wherein ∼75 g batches of silicon have been melted in graphite or Si_3N_4 crucibles. In addition, two ∼12 kg castings have been performed in a pilot scale directional solidification furnace using Si_3N_4-coated quartz crucibles.

Although some portions of the present work are based on the analysis of solid samples cut from finished silicon ingots, the main experimental method of data acquisition has been the direct extraction of liquid samples from the silicon melt. These samples were subsequently analysed for content of the impurity of interest. The challenges that needed to be overcome with this method can be divided into those directly involved with the experimental method and those connected with the difficulties of obtaining reliable chemical analyses of impurities in the ppm-range.

Experimentally, the preservation of the atmosphere and the quenching of the samples were major concerns. Ideally, one would like to be

able to extract samples with no disturbance of the furnace atmosphere and then quench them instantaneously. In the present experimental work, various sealing mechanisms and increased furnace pressure were employed on the two furnaces in order to preserve the atmosphere. While these apparatus cannot be expected to completely preserve the furnace atmosphere, they where efficient enough to keep the oxygen content of the melts at a point where SiO_2-particles did not form. As for the quenching of the samples, the cooling was fast enough to avoid visible nucleation of SiC and Si_3N_4 particles.

In the early days of the present work, different methods of chemical analysis were considered. In the work with the Si–B-system, several methods and laboratories were compared. The variation in the results discussed herein underlines the difficulty of working with low concentrations of impurities. In carbon and nitrogen containing systems, the analyses of Elkem were trusted because of their considerable experience in this field. A slight scatter of the data is still to be expected in experimental work of this nature, and can be remedied by statistical treatment of the data.

6.1 Main conclusions

From two directionally solidified castings, several solid samples were analysed at various laboratories. By fitting the boron content as a function of ingot height to the Scheil equation for the different data sets, different values were derived for the effective distribution coefficient of boron in silicon, in the interval 0.69-0.86. Through a critical assessment of the avaiable data sets, a subset of measurements were chosen from which

- The effective distribution coefficient of boron in silicon was estimated as
$$k_e = 0.70$$

The chemical analysis of the samples extracted from the liquid phase during the directional solidification of the second ingot showed a Scheil-like distribution of boron. However, the absolute values were lower than what was found in the solid phase, meaning that these results were erroneous. However, by re-scaling all data from the liquid samples with a constant amount so that the starting liquid concentration matched what was calculated from the solid samples, analyses could be performed that pointed to a distribution coefficient on the order of 0.8. While there was great uncertainty connected to the results from the samples extracted from the liquid phase, they were taken as a weak confirmation of the data found from the solid samples.

A main part of the work has been the behaviour of carbon and nitrogen in a silicon melt held in a graphite or Si_3N_4 crucible. An important conclusion was that the concentrations of carbon and nitrogen rose rapidly to their eqiuilibrium concentrations; in other words:

- The dissolution of SiC into liquid silicon with dissolved carbon is very rapid, and the equilibrium carbon concentration is achieved within a maximum of three minutes of attaining temperature.
- The dissolution of Si_3N_4 into liquid silicon with dissolved nitrogen is very rapid, and the equilibrium nitrogen concentration is achieved within a maximum of three minutes of attaining temperature.

The dissolution of nitrogen was investigated under both an Ar and a N_2 atmosphere. As no significant difference was observed between the two, it was concluded that:

- The dissolution of Si_3N_4 into liquid silicon with dissolved nitrogen is much faster than the off gassing of nitrogen as N_2-gas at the gas–liquid interface.

Through the fitting of the experimental solubility data from the pure Si–C and Si–N systems it was concluded that:

- The solubility of carbon in liquid silicon equilibrated with SiC as a function of temperature for the temperature range between 1414–1559 °C is described by:

$$C_C(T) = 482.84 \cdot \exp\left(-\tfrac{18897}{T}\right)$$

- The solubility of nitrogen in liquid silicon equilibrated with Si_3N_4 as a function of temperature in the temperature range between 1428–1542 °C, is described by:

$$C_N(T) = 1.0484 \cdot 10^5 exp\left(\tfrac{-28841}{T}\right)$$

From the Arrhenius equations describing solubility, simple thermodynamical derivations were performed in order to obtain expressions for the dissolution energies of carbon and nitrogen:

- The dissolution energy of carbon after the reaction:
  $C(s) \leftrightharpoons \underline{C}(l)$
  was found to follow:
  $\Delta G_C^{diss} = 4.6 \cdot 10^4 - 11.4T \log T + 23.2T$

- While the dissolution of nitrogen after the reaction:
  $(1/2)N_2(g) \rightleftharpoons \underline{N}(l)$
  was found to follow:
  $\Delta G_N^{diss} = -1.59 \times 10^4 + 77T$

The Si–SiC–Si_3N_4-equilibrium was studied through an experimental investigation of a silicon melt simultaneously saturated with carbon and nitrogen. With a basis in the solubility equations for the pure

Si–C and Si–N systems, the fitting of the experimental data led to the conclusion that:

- The interaction parameters between carbon and nitrogen in liquid silicon in the temperature range between 1422-1525 °C are given as:

$$e_N^C = 110.83 - 207123/T$$

and

$$e_C^N = 95.01 - 177555/T$$

From these expressions, an equation describing the carbon solubility as a function of both temperature and nitrogen concentration could be derived:

- The solubility of carbon in a nitrogen-enriched silicon melt is described by:

$$C_C(T, C_N) = 7.37 \cdot \exp\left\{\frac{-11731}{T} - \ln(10) \cdot [(95.01 - 177555/T) \cdot C_N]\right\}$$

This equation is valid up to the solubility limit of nitrogen, and for the temperature range between 1422–1525 °C.

Similarily, for the solubility of nitrogen as a function of temperature and carbon content:

- The solubility of nitrogen in a carbon-enriched melt is described by:

$$C_N(T, C_C) = 104840 \cdot \exp\left\{\frac{-28841}{T} - \ln(10) \cdot [(110.83 - 207123/T) \cdot C_C]\right\}$$

This equation is valid up to the solubility limit of carbon, and for the temperature range between 1422–1525 °C.

Since the above expressions cannot be used explicitly to predict the carbon and nitrogen content as a function of temperature during simultaneous saturation, an iterative solution method was used in order to plot the saturation limits of carbon and nitrogen in liquid silicon during simultaneous saturation. It was observed from this plot that the saturation limits depended almost linearly on temperature, and a linear regression was performed to obtain approximations to the solubility limits as explicit functions of temperature:

- During simultaneous saturation of carbon and nitrogen, the carbon solubility in liquid silicon can be approximated by the linear expression:

$$C_C^{N_{sat}} = 3.80 \cdot 10^{-5} T - 5.62 \cdot 10^{-2}$$

- During simultaneous saturation of carbon and nitrogen, the nitrogen solubility in liquid silicon can be approximated by the linear expression:

$$C_N^{C_{sat}} = 7.03 \cdot 10^{-5} T - 0.114$$

The ternary system Si–B–C was investigated through a series of experiments with a boron-enriched silicon melt in a graphite crucible. With basis in the Arrhenius equation found for the carbon solubility in pure silicon, the experimental data was used to estimate the carbon-boron interaction coefficient. It was concluded that:

- The solubility of carbon in liquid silicon increases in the presence of boron, and the greater the greater the boron addition the greater the effect.

- The boron–carbon interaction coefficient in silicon was determined as:

  $e_C^B = -0.15 + 51.6/T$

- The solubility of carbon in a boron-enriched silicon melt is given as a function of temperature and boron content as:

  $C_C(T, C_B) = 482.84 \cdot \exp\left\{-\frac{18897}{T} - \ln(10) \cdot [(-0.15 + 51.6/T) \cdot C_B]\right\}$

A preliminary study of the ternary Si–B–N-system was carried out with two experiments on a boron-enriched silicon melt in a Si_3N_4 crucible. The presence of boron caused the amount of nitrogen in the extracted samples to decrease when compared to the pure Si–N-system. One of the experiments was carried out at boron levels below the saturation limit of BN in liquid silicon. From this experiment it was concluded that:

- The solubility of nitrogen in liquid silicon decreases in the presence of boron.
- The boron–nitrogen interaction coefficient in silicon was determined as:
  $e_N^B = -28 + 52551/T$

A second experiment in the Si–B–N-system was carried out at a high level of supersaturation of boron with respect to the formation of BN. No detectable amounts of BN were found in the extracted samples and it was concluded that:

- The formation of BN is strongly suppressed in nitrogen saturated liquid silicon.

6.2 Suggestions for future work

In the present work, some preliminary experiments were performed in the Si–B–N-system. A logical next step would be to investigate this system more thoroughly. The estimate of e_N^B could be improved by conducting more experiments similar to the ones already performed, but with boron additions below 0.1 m.%. It would also be interesting to use a BN crucible in order to investigate the simultaneous saturation of boron and nitrogen.

Another logical continuation would be to include new elements. One could then investigate the solubility of these new elements in liquid silicon, and later consider the interactions between the new elements and the ones already studied. Several elements would be of interest, with some logical candidates being oxygen and phosphorous.

A somewhat different but perhaps more exciting prospect would be to investigate the behaviour of carbon and nitrogen during directional solidification. If an in situ analysis of the gas phase was possible, an understanding of how these elements enter, leave and precipitate in silicon during solidification could be the result.

The current work has focused mainly on silicon in the liquid state. A logical continuation would be to investigate the solubilities and interactions of carbon, boron and nitrogen in solid silicon. This would represent not so much a continuation and expansion of the current work as a completely new and independent project that—while closely related to the current work "in spirit"—would represent a whole new and different set of opportunities and challenges.

Bibliography

[1] The Intergovernmental Panel on Climate Change. Summary for Policymakers: The Science of Climate Change - IPCC Working Group I. Retrieved from: <http://www.ipcc.ch/pdf/climate-changes-1995/spm-science-of-climate-changes.pdf>, December 3rd, 2009, 1995.

[2] S. Solomon, D. Qin, M. Manning, R.B. Alley, T. Berntsen, N.L. Bindoff, Z. Chen, A. Chidthaisong, J.M. Gregory, G.C. Hegerl, M. Heimann, B. Hewitson, B.J. Hoskins, F. Joos, J. Jouzel, V. Kattsov, U. Lohmann, T. Matsuno, M. Molina, N. Nicholls, J.Overpeck, G. Raga, V. Ramaswamy, J. Ren, M. Rusticucci, R. Somerville, T.F. Stocker, P. Whetton, R.A. Wood, and D. Wratt. Technical summary. In S. Solomon, D. Qin, M. Manning, Z. Chen, M. Marquis, K.B. Averyt, M. Tignor, and H.L. Miller, editors, *Climate Change 2007: The Physical Science Basis. Contribution of Working Group I to the Fourth Assessment Report of the Intergovernmental Panel on Climate Change*. 2007.

[3] The German Advisory Council for Global Change. http://www.wbgu.de, retrieved: 26-06-09.

[4] B. G. Streetman and S. Banerjee. *Solid state electronic devices*. Prentice Hall international, 5 edition, 2000.

[5] M. Quirk and J. Serda. *Semiconductor manufacturing technology*. Prentice Hall, 2001.

[6] R. E. Hummel. *Electronic properties of materials*. Springer, 3 edition, 2001.

[7] B. Ryningen, K. S. Sultana, E. Stubhaug, O. Lohne, and P. C. Hjelmås. Dislocation clusters in multicrystalline silicon. In *Proccedings of the 22nd European photovoltaic solar energy conference*, pages 1086–1090, 2007.

[8] G. Du, L. Zhoua, P. Rossettob, and Y. Wanb. Hard inclusions and their detrimental effects on the wire sawing process of multicrystalline silicon. *Solar Energy Materials & Solar Cells*, 91:1743–1748, 2007.

[9] C.V.H. Rao, H.E. Bates, and K.V. Ravi. Electrical effects of SiC inclusions in EFG silicon ribbon solar-cells. *Journal of applied physics*, 47(6):2614–2619, 1976.

[10] M. H. Al-Rifai, O. Breitenstein, J.P. Rakotoniaina, M. Werner, A. Kaminski, and N. Le Quang. Investigation of material-induced-shunts in block cast multicrystalline silicon solar cells caused by SiC precipitate filaments. In *Proceedings of the 19th European photovoltaic solar energy conference, 7-11 June 2004, Paris, France*, pages 632–635, 2004.

[11] A. Çiftja, T. A. Engh, M. Tangstad, and A. Kvithyld. Recycling of silicon scrap by filtration. In *Proceedings of the 23rd European Photovoltaic Solar Energy Conference, Valencia, Spain*, pages 1274–1277, 2008.

[12] J.P. Rakotoniaina, O. Breitenstein, M. Werner, M. Hejjo Al-Rifai, T. Buonassisi, M.D. Pickett, M. Ghosh, A. Müller, and

N. Le Quang. Distribution and formation of silicon carbide and silicon nitride precipitates in block-cast multicrystalline silicon. In *Proceedings of the 20th European photovoltaic solar energy conference*, pages 773–776, 2005.

[13] A-K. Søiland, E. J. Øvrelid, O. Lohne, J. K. Tuset, T. A. Engh, and Ø. Gjerstad. Carbon and nitrogen contents and inclusion formation during crystallisation of multi-crystalline silicon. In *Proceedings of the 19th European photovoltaic solar energy conference, 7-11 June 2004, Paris, France*, pages 911–914, 2004.

[14] A-K. Søiland, E.J. Øvrelid, T.A. Engh, O. Lohne, J.K. Tuset, and Ø. Gjerstad. SiC and Si_3N_4 inclusions in multicrystalline silicon ingots. *Materials science in semiconductor processing*, 7:39–43, 2004.

[15] K. Tang. Thermochemical and kinetic databases designed for the solar grade silicon materials. In *Proceedings of the 2nd international workshop on crystalline silicon solar cells. Xiamen, China, December 9-13*, 2007.

[16] K. Tang. Personal communication.

[17] K. Tang, E. J. Øvrelid, G. Tranell, and M. Tangstad. Thermochemical and kinetic databases for the solar cell silicon materials. In *Crystal growth of Si for solar cells*. Springer, Accepted for publication.

[18] H.J. Möller. Semiconductors for solar cell applications. In *Progress in Materials Science*, chapter 4.1.2 Oxygen and carbon, pages 277–284. 1991.

[19] R. I. Scace and G. A. Slack. Solubility of carbon in silicon. *The journal of chemical physics*, 30:1551–1555, 1959.

[20] R. N. Hall. Electrical contacts to silicon carbide. *Journal of applied physics*, 29:914–917, 1958.

[21] R.W Olesinski and G.J. Abbaschian. The C-Si (Carbon-silicon) system. *Bulletin of alloy phase diagrams*, 5:486–489, 1984.

[22] F. Durand and J. C. Duby. Carbon solubility in solid and liquid silicon-a review with reference to eutectic equilibrium. *Journal of phase equilibria*, 20:61–63, 1999.

[23] R.T. Dolloff. Research study to determine the phase equilibrium relations of selected metal carbides at high temperatures. In *WADD technical report 60-143*. 1960.

[24] R. C. Newman and J. B. Willis. Vibrational absorption of carbon in silicon. *Journal of physics and chemistry of solids*, 26(2):373–379, 1965.

[25] E. Haas, W. Brandt, and J. Martin. Über das verhalten von kohlenstoff beim zonenziehen von silicium. *Solid-State electronics*, 12:915–921, 1969.

[26] A. R. Bean and R. C. Newman. The solubility of carbon in pulled silicon crystals. *Journal of physics and chemistry of solids*, 32(6):1211–1219, 1971.

[27] T. Nozaki, Y. Yatsurugi, and N. Akiyama. Concentration and behaviour of carbon in semiconductor silicon. *Journal of the electrochemical society*, 117:1566–1568, 1970.

[28] Y. Endo, Y. Yatsurugi, N. Akiyama, and T. Nozaki. Infrared spectrophotometry for carbon in silicon as calibrated by charged particle activation. *Analytical chemistry*, 44(14):2258–2262, 1972.

[29] F.W. Voltmer and F.A. Padovani. The carbon-silicon phase diagram for dilute carbon concentration and the influence of carbon on Czochralski growth of silicon. In H.R. Huff and R.R. Burgess, editors, *Semiconductor Silicon*, 1973.

[30] B. O. Kolbesen and A. Mühlbauer. Carbon in silicon: properties and impact on devices. *Solid state electronics*, 25(8):759–775, 1982.

[31] L. L. Oden and R. A. McCune. Phase-equilibria in the Al-Si-C system. *Metallurgical transactions A*, 18:2005–2014, 1987.

[32] A-K. Søiland. *Silicon for Solar Cells*. PhD thesis, NTNU, 2004.

[33] K. Yanaba, M. Akasaka, M. Takeuchi, M. Watanabe, T. Narushima, and Y. Iguchi. Solubility of carbon in liquid silicon equilibrated with silicon carbide. *Materials Transactions*, 38:990–994, 1997.

[34] H. J. Seifert and J. Aldinger. Phase equilibria in the Si-B-C-N-system. In *Structure and bonding*, volume 101, pages 1–58. Springer Verlag, 2002.

[35] S. Suhara, N. Yuge, M. Fukai, and F. Aratani. CAMP-ISIJ 2:1341, 1989.

[36] L. Ottem. Løselighet og termodynamiske data for oksygen i flytende legeringer av silisium og ferrosilisium. Technical Report STF34 F93017, SINTEF, 1993.

[37] H. Kleykamp and G. Schumacher. The constitution of the silicon-carbon system. *Berichte der Bunsen-Gesellschaft für Physikalische Chemie*, 97(6):799–805, 1993.

[38] T. Narushima, A. Yamashita, C. Ouchi, and Y. Iguchi. Solubilities and equilibrium distribution coefficients of oxygen and carbon in silicon. *Materials transactions*, 43(8):2120–2124, 2002.

[39] C. Brosset and B. Magnusson. The silicon-boron system. *Nature*, 187:54–55, 1960.

[40] B. Magnusson and C. Brosset. The crystal structure of $B_{2.89}Si$. *Acta Chemica Scandinavia*, 16:449–455, 1962.

[41] P. Ettmayer, H. C. Horn, and K. A. Schwetz. Untersuchungen im system silicium-bor mit hilfe der elektronenstarhl-mikroanalyse. *Mikrochimica acta*, 4:87–95, 1970.

[42] B. G. Arabei. Interaction in the system Si-B. Translated from Izyvestiya Akademii Nauk SSSR, Neorganicheskie Materialy, vol 15, 1979. *Inorganic materials*, 15(9):1563–1566, 1979.

[43] R.W Olesinski and G.J. Abbaschian. The B-Si (Boron-silicon) system. *Bulletin of alloy phase diagrams*, 5:478–484, 1984.

[44] M. Vlasse, G. A. Slack, M. Garbauskas, J. S. Kasper, and J. C. Viala. The crystal structure of SiB_6. *Journal of solid state chemistry*, 63(1):31–45, 1986.

[45] E. Lugscheider, H. Reimann, and W-J. Quadakkers. Das system bor-silicium. *Berichte der deutschen keramischen gesellschaft*, 56(10):301–305, 1979.

[46] B. Armas, G. Male, D. Salanoubat, C. Chatillon, and M. Allibert. Determination of the boron-rich side of the B-Si phase diagram. *Journal of the less common metals*, 82(1-2):245–254, 1981.

[47] G.V. Samsonov and V.M. Sleptsov. Investigation of the solubility of boron in silicon. *Russian journal of inorganic chemistry*, 8:1047–1048, 1963.

[48] J. Hesse. Loeslichkeit und Ausscheidungskinetik von Bor in polykristallinem Silizium. *Z. Metallkd.*, 59:499–502, 1968.

[49] G. L. Vick and K. M. Whittle. Solid solubility and diffusion coefficients of boron in silicon. *Journal of the electrochemical society*, 116(8):1142–1144, 1969.

[50] H. Ryssel, K. Müller, K. Haberger, R. Henkelmann, and F. Jahnel. High concentration effects of ion implanted boron in silicon. *Applied physics*, 22(1):35–38, 1980.

[51] G. Malé and D. Salanoubat. Sur l'existence d'une phase riche en bore dans le système bore-silicium *(on the existence of a rich boron phase in the boron-silicon system). Revue internationale des hautes températures et des réfractaires*, 18(1):109–120, 1981.

[52] W. R. Thurber, R. L. Mattis Y. M. Liu, and J. J. Filliben. Resistivity-dopant density relationshop for boron doped silicon. *Journal of the Electrochemical society*, 127(10), 1980.

[53] H. R. Huff, T. G. Digges Jr., and O. B. Cecil. Distribution coefficient of boron and phosphorus in silicon. *Journal of applied physics*, 42:1235–1236, 1971.

[54] B. C. Sim, K.H.Kim, and H.W. Lee. Boron segregation control in silicon crystal ingots grown in Czochralski process. *Journal of crystal growth*, 290:665–669, 2006.

[55] P. S. Ravishankar, L. P. Hunt, and R. W. Francis. Effective segregation coefficient of boron in silicon ingots grown by the

Czochralski and Bridgman techniques. *Journal of the Electrochemical society*, 131:872–874, 1984.

[56] F. N. Schwettmann. Characterization of incomplete activation of high-dose boron implants in silicon. *Journal of applied physics*, 45(4):1918–1920, 1974.

[57] R. N. Hall. Segregation of impurities during the growth of germanium and silicon crystals. *Journal of physical chemistry*, 57(8):836–839, 1953.

[58] A. Zerr, G. Miehe, G. Serghiou, M. Schwarz, E. Kroke, R. Riedel, H. Fuess, P. Kroll, and R. Boehler. Synthesis of cubic silicone nitride. *Nature*, 400(6742):340–342, 1999.

[59] W. Kaiser and C. D. Thurmond. Nitrogen in silicon. *Journal of applied physics*, 30:427, 1959.

[60] Y. Yatsurugi, N. Akiyama, and Y. Endo. Concentration, solubility and equilibrium distribution coefficient of nitrogen and oxygen in semiconductor silicon. *Journal of the electrochemical society*, 120(7):975–979, 1973.

[61] T. Narushima, N. Ueda, M. Takeuchi, F. Ishii, and Y. Iguchi. Nitrogen solubility in liquid silicon. *Materials Transactions*, 35(11):821–826, 1994.

[62] M. Tanahashi, T. Fujisawa, and C. Yamauchi. Activity of boron in molten silicon. *Shigen-to-Sozai*, 114(11):807–812, 1998.

[63] T. Yoshikawa and K. Morita. Thermodynamic property of b in molten si and phase relations in the si-al-b system. *Materials transactions*, 46(6):1335–1340, 2005.

[64] R. Noguchi, K. Suzuki, F. Tsukihashi, and N. Sano. Thermodynamics of boron in a silicon melt. *Metallurgical and material transactions B*, 25:903–907, 1994.

[65] S. K. Mitra. Active nitrogen. *Physical review*, 90(4):516–521, 1953.

[66] T. Narushima, K. Matsuzawa, Y. Mukai, and Y. Iguchi. Oxygen solubility in liquid silicon. *Materials Transactions*, 35(8):522–528, 1994.

[67] G. V. Samsonov and N. N. Zhuravlev. Fiz met metalloved. 3:309, 1956.

[68] N. N. Zhuravlev, G. Makarenko, and G. G. Samsonov. Izvest akad nauk sssr, otdel tekh nauk met i toplivo. 1:133, 1960.

[69] R. P. Elliot and R. J. Van Thyne. The boron-carbon system. [f]inal [t]echical [r]eport [arf] 2200-12. US Atomic Energy Comission.

[70] R. Kieffer, E. Gugel, G. Leimer, and P. Ettmayer. Untersuchungen in System Bor-Kohlenstoff-Silisium. *Berichte der deutchen keramischen gesellschaft*, 49(2):41–72, 1972.

[71] H. Saitoh, K. Yoshida, and W. A. Yarbrough. Crystal structure of new composition boron-rich boron nitride using Raman spectrospcopy. *Journal of materials research*, 8(1), 1993.

[72] K. Ploog, H. Schmidt, E. Amberger, G. Will, and K. H. Kossobutzki. $B_{48}B_2C_2$ und $B_{48}B_2N_2$, zwei nichtmetallboride mit der struktur des sog. i tetragonalen bors. *Journal of the Less Common Metals*, 29:161–169, 1972.

[73] A. Y. Liu and M.L Cohen. Prediction of new low compressibility solids. *Science*, 245(4920):841–842, 1989.

[74] C. M. Niu, Y.Z. LU, and C. M. Lieber. Experimental realization of the covalent solid carbon nitride. *Science*, 261(5119):334–337, 1993.

[75] R. Ruh, M. Kearns, A. Zangvil, and Y. Xu. Phase and property studies of boron carbide-boron nitride composites. *Journal of the american ceramics society*, 75(4):864–872, 1992.

[76] K. I. Portnoi, G. V. Samsonov, and L. A. Solonnikova. Alloys of the boron-silicon-carbon system. *Russian journal of inorganic chemistry*, 5(9):988–993, 1960.

[77] P. T. B. Schaffer. The SiC phase in the system SiC-B_4C-C. *Materials Research Bulletin*, 4:213–220, 1969.

[78] E. Gugel, R. Kieffer, G. Leimer, and P. Ettmayer. Investigations in the ternary system boron-carbon-silicon. In *Proceedings of 5th Materials Research Symposium*, pages 505–513, 1972.

[79] K. Yanaba, Y. Matsumara, T. Narushima, and Y. Iguchi. Effect of alloying elements on carbon solubility in liquid silicon equilibrated with silicon carbide. *Materials Transactions*, 39(8):819–823, 1998.

[80] C-L. Liu, W. Windl, L. Borucki, S. Lu, and X-Y. Liu. Ab initio modelling and experimental study of c-b interactions in si. *Applied Physics Letters*, 80(1):52–54, 2002.

[81] D. Yang, D. Li, M. Ghosh, and H. J. Möller. Defects in nitrogen-doped multicrystalline silicon. *Physica B*, 344(1-4):1–4, 2004.

[82] R. Riedel, A. Greiner, G. Miehe, W. Dressler, H. Fuess, J. Bill, and F. Aldinger. The first crystalline solids in the ternary si-c-n system. *Angewandte chemie-international edition in english*, 36(6):603–606, 1997.

[83] E. Gugel, P. Ettmayer, and A. Schmidt. Untersuchungen zum System Silizium-Kohlenstoff-Stickstoff. *Berichte der Deutschen Keramischen Gesellschaft*, 54:395–402, 1968.

[84] T. Kandori, N. Kamiya, and O. Kamigaito. *Japanese journal of applied physics*, 14(1):137–138, 1976.

[85] and J. Seitz J. Bill, G. Thurn, J. Durr, J. Canel, B.Z. Janos, A. Jalowiecki, D. Sauter, S. Schempp, H. P. Lamparter, J. Mayer, and F. Aldinger. Structure analysis and properties of Si-C-N ceramics derived from polysilazanes. *Physica status solidi A-applied research*, 166(1):269–296, 1998.

[86] A. Dörnen, R. Sauer, and G. Pensl. Complexing of nitrogen with carbon and oxygen in silicon: Photoluminescence studies. *Journal of electronic materials*, 17(2):121–125, 1988.

[87] Akito Hara and Akira Ohsawa. New carbon related defects formed in nitrogen rich czochralski silicon crystals. *Applied physics letters*, 59(15):1890–1892, 1991.

[88] M. Weinmann, J. Schuhmacher, H. Kummer, S. Prinz, J.Q. Peng, H.J. Seifert, M. Christ, K. Muller, J. Bill, and F. Aldinger. Synthesis and thermal behavior of novel si-b-c-n ceramic precursors. *Chemistry of materials*, 12(3):623–632, 2000.

[89] Svein Stølen and Tor Grande. *Chemical thermodynamics of materials*. Wiley, 2004.

[90] Crystalox inc ds 250. technical documentation.

[91] R. Kvande, Ø. Mjøs, and B. Ryningen. Growth rate and impurity distribution in multicrystalline silicon for solar cells. *Materials Science and Engineering A*, 413-414:545–549, 2005.

[92] S. Gaal. Personal communication.

[93] J. Fenstad. *Liquidus relations and thermochemistry within the system Fe-Mn-C-O*. PhD thesis, NTNU, 2000.

[94] Morgan Ceramics P. Manison. Personal communication.

[95] A. Çiftja. Personal communication.

[96] O. Kubaschewski and C. B. Alcock. *Metallurgical Thermochemistry*, page 383. Pergamon Press, 5 edition, 1979.

[97] K. Abe, K. terashima, T. Matsumoto, S. Maeda, H. Nakanishi, and K. Hoshikawa. Oxygen solubilities in si melts: The influence of carbon addition. *Journal of the electrochemical society*, 145(1):319–322, 1998.

[98] T. Carlberg. Calculated solubilities of oxygen in liquid and solid silicon. *Journal of the Electrochemical society*, 133(9):1940–1942, 1986.

[99] A. Seidl and G. Müller. Oxygen solubility in silicon melt measured in situ by an electrochemical solid ionic sensor. *Journal of the electrochemical society*, 144(9):3243–3245.

[100] S. W. Tu and D. Janke. On the oxygen solubility in molten silicon. *Zeitschrift für metallkunde*, 85(10):701–704, 1994.

[101] R. Kvande. *Incorporation of impurities during directional solidification of multicrystalline silicon for solar cells*. PhD thesis, NTNU, 2008.

[102] Ø. Mjøs. *Directional solidification of silicon for solar cells.* PhD thesis, NTNU, 2006.

[103] B. Ryningen. *Formation and growth of crystal defects in directionally solidified multicrystalline silicon for solar cells.* PhD thesis, NTNU, 2008.

[104] H.S. Tathgar. *Solubility of Nickel in Mg-Al, Mg-Al-Fe, and Mg-Al-Mn systems.* PhD thesis, NTNU, 2001.

Appendix A

Numerical data

A.1 Boron distribution

Table A.1: Boron contents (ppmm) from the DS-Si-B-1 experiment. Analysed with the GDMS at NTNU.

Sample	Fraction solidified	Spot 1			Spot 2		
		a	b	c	a	b	c
2	0.14	0.38	0.40	0.40	0.34	0.35	0.37
2	0.21	0.39	0.37	0.38	0.41	0.37	0.35
7	0.65	0.48	0.48	0.49	0.47	0.43	0.42
7	0.73	0.52	0.53	0.52	0.46	0.53	0.50
8	0.75	0.51	0.52	0.53	0.48	0.54	0.55

Table A.2: Boron contents (ppmm) from the DS-Si-B-2 experiment, as found for different methods of analysis.

Sample	Face	Fraction solidified	Analysed by NTNU-I			NTNU-II	Thermo	Elkem
A-1	btm	0.00						
B-1	average	0.04						0.34
B-2	btm	0.10					0.28	
A-1	top	0.12				0.23		
A-2	btm	0.14	0.30	0.32	0.30	0.23		
B-2	top	0.18					0.24	
A-2	top	0.24	0.35	0.34	0.36	0.32		
B-3	average	0.24						0.36
A-3	btm	0.26				0.24		
A-3	top	0.33				0.27		
B-4	average	0.35						0.41
A-4	btm	0.35				0.27		
A-4	top	0.43				0.26		
A-5	btm	0.45	0.36	0.42	0.34	0.30		
B-5	average	0.46						0.46
B-6	btm	0.54					0.30	
A-5	top	0.56	0.38	0.35	0.37	0.36		
A-6	btm	0.58	0.38	0.37	0.38	0.31		
B-6	top	0.65					0.32	
A-6	top	0.69	0.39	0.44	0.47	0.35		

Table A.3: Other impurities (ppmm) from the DS-Si-B-2 experiment, as found by the different analyses.

	Sample	Fraction solidified	Impurity		
			P	S	F
Thermo	B-2	0.1	0.37	0.77	0.38
	B-2	0.19	0.37	0.62	0.35
	B-6	0.55	0.6	0.74	0.39
	B-6	0.66	0.77	0.86	0.4
NTNU	A-2	0.14		0.02	
	A-6	0.58		0.02	
Elkem	B-1	0.04	0.5		
	B-3	0.24	0.5		
	B-4	0.35	0.5		
	B-5	0.46	0.6		

Table A.4: The reported boron contents in the samples extracted from the liquid phase.

Sample no.	Fraction solidified	Boron level [ppm mass]	Sample no.	Fraction solidified	Boron level [ppm mass]
1	0	0.20	7	0.32	0.11
2	0	0.20	8	0.48	0.23
3	0	0.22	9	0.67	0.32
4	0.04	0.21	10	0.84	0.35
5	0.12	0.25	11	0.94	0.59
6	0.22	0.15	12	0.99	1.63

A.2 Si–C-system

Table A.5: The carbon levels and settlement times for all parallels from all analysed samples from experiment Si-C-1.

Sample #	T [°C]	t_s [min]	C content [ppm mass]			
1	1432	6	76			
2	1431	23	79	180	78	
3	1431	36	770			
4	1432	51	131			
5	1432	81	69	99		
6	1431	97	67			
7	1430	112	80	88		
8	1432	126	66	77		
9	1442	11	125	82	82	
10	1439	56	81	85	88	
11	1440	71	78	856	79	1616
12	1440	87	177	73	1357	
13	1440	116	84	83	65	
14	1441	131	43	123	60	

Table A.6: The carbon levels and settlement times for all parallels from all analysed samples from experiment Si-C-2.

Sample #	T [°C]	t_s [min]	C content [ppm mass]			
1	1414	38	86	404	58	
2	1422	54	74	75	100	
3	1421	68	269	75	295	
4	1420	83	69	64	93	
5	1421	113	906	57	68	784
6	1419	143	63			
7	1419	158	47	82	60	
8	1426	23	94			
9	1426	38	60	54	69	

Table A.7: The carbon levels and settlement times for all parallels from all analysed samples from experiment Si-C-3.

Sample #	T [°C]	t_s [min]	C content [ppm mass]		
1	1428	39	90	74	82
2	1433	9	121	64	100
3	1433	40	93	55	47
4	1443	39	80	91	91
5	1559	18	203	220	184
6	1559	40	177	188	164

Table A.8: The carbon levels and settlement times for all parallels from all analysed samples from experiment Si-C-4.

Sample #	T [°C]	t_s [min]	C content [ppm mass]		
1	1423	7.57	83	70	90
2	1419	38	71	97	60
4	1428	40	66	76	63
6	1434	40	76	70	66
8	1444	39.95	82	68	76
9	1511	3	106	130	75
10	1510	40	122	101	251
11	1510	63	99	108	106
12	1520	93	124	100	93
13	1509	123	79	117	88

Table A.9: The carbon levels and settlement times for all parallels from all analysed samples from experiment Si-C-5.

Sample #	T [°C]	t_s [min]	C content [ppm mass]		
1	1456	2	65	99	85
2	1464	5	77	81	86
3	1485	6	79	99	91
4	1505	10	111	103	102
5	1525	5	74	93	100
			96	97	115
			179	187	144

A.3 Si–N-system

Table A.10: The nitrogen levels and settlement times for all parallels from all analysed samples from experiment Si-N-1.

Sample #	T [°C]	t_s [min]	N content [ppm mass]		
1	1436	4	60	46	
2	1437	19	40	48	
3	1437	34	45	48	43
4	1437	49	46		
5	1437	65	61		
6	1437	82	59	46	
7	1437	94	40	46	
8	1437	116	47		
9	1437	127	54	39	46
10	1446	4	65		
11	1447	12	58	73	
12	1447	40	54	47	45
13	1455	5	29	56	

Table A.11: The nitrogen levels and settlement times for all parallels from all analysed samples from experiment Si-N-2.

Sample #	T [°C]	t_s [min]	N content [ppm mass]		
1	1428	5.88	71	40	61
2	1428	53.88	49	48	50
3	1428	90.88	59	56	48
4	1428	121.88	84	56	110
5	1432	9.08	58	40	49
6	1432	20.92	44	60	27
7	1437	9.28	42	99	52
8	1437	18.28	167	68	58
9	1437	24.28	48	47	48
10	1438	33.36	49		
11	1448	9.77	57	56	63
12	1448	15.77	47	163	
13	1448	25.77	66	48	58
14	1458	4.87	58	47	48
15	1458	22.87	58	68	87

Table A.12: The nitrogen levels and settlement times for all parallels from all analysed samples from experiment Si-N-3.

Sample #	T [°C]	t_s [min]	N content [ppm mass]		
1	1428	4	41		
2	1428	19	50	47	
3	1454	2	92		
4	1457	14	54		
5	1457	33	58		
6	1457	37	57		
7	1475	3	68		
8	1476	8	74		
9	1476	13	57	71	62
10	1494	2	87	94	
11	1497	11	135	95	
12	1514	2	91	94	

Table A.13: The nitrogen levels and settlement times for all parallels from all analysed samples from experiment Si-N-4.

Sample #	T [°C]	t_s [min]	N content [ppm mass]		
1	1443	3	142	147	159
2	1443	14	276	625	254
3	1461	3	65	53	
4	1462	8	238	491	
5	1462	21	38	119	
6	1481	3	32	55	61
7	1483	10	203	149	

Table A.14: The nitrogen levels and settlement times for all parallels from all analysed samples from experiment Si-N-5.

Sample #	T [°C]	t_s [min]	N content [ppm mass]		
1	1477	5	65	70	48
2	1490	18	68	73	
3	1492	27	75	96	
4	1492	51	62	39	
5	1500	2	79	185	97
6	1501	6	90	89	66
7	1501	14	77	88	54
8	1510	3	93	69	79
9	1511	8	90	91	
10	1511	21	65	78	68
11	1511	27	97	89	95
12	1519	3	95	100	
13	1520	7	230	92	128
14	1520	16	114	634	84
15	1520	21	98	101	573
16	1528	2	2227	99	113
17	1529	5	104	101	
18	1530	9	112	115	207
19	1540	4	120	127	
20	1541	10	113	126	121
21	1542	15	114	138	129

A.4 Si–C–N-system

Table A.15: The carbon and nitrogen levels and settlement times for all parallels from all analysed samples from experiment Si-C-N-1.

Sample #	T [°C]	t_s [min]	C content [ppm mass]			N content [ppm mass]		
1	1423	32	150	61	98			
2	1443	6				65	69	59
3	1463	9	105	82	96			
4	1484	9				91	86	99
5	1505	14	115	119	117			
6	1525	12				102	138	118

Table A.16: The carbon and nitrogen levels and settlement times for all parallels from all analysed samples from experiment Si-C-N-2.

Sample #	T [°C]	t_s [min]	C content [ppm mass]			N content [ppm mass]		
1	1422	16	64	76	67			
2	1441	11				62	61	58
3	1462	16	90	59	73			
4	1481	17				90	95	78
5	1501	14	123	127	95			
6	1521	5				133	117	130

Table A.17: The carbon and nitrogen levels and settlement times for all parallels from all analysed samples from experiment Si-C-N-3.

Sample #	T [°C]	t_s [min]	C content [ppm mass]			N content [ppm mass]		
1	1422	23	73	69	86			
2	1483	14				90	77	103
3	1502	12	120	136	106			
4	1523	10				105	126	

Table A.18: The carbon and nitrogen levels and settlement times for all parallels from all analysed samples from experiment Si-C-N-4.

Sample #	T [°C]	t_s [min]	C content [ppm mass]			N content [ppm mass]		
1	1422	10	51	101	36			
2	1424	44				58	62	48
3	1441	11	78	108	80			
4	1462	30				60	80	78
5	1481	6	128	82	105			
6	1500	9				112	91	114

Table A.19: The carbon and nitrogen levels and settlement times for all parallels from all analysed samples from experiment Si-C-N-5.

Sample #	T [°C]	t_s [min]	C content [ppm mass]			N content [ppm mass]		
1	1439	24	64	71	102			
2	1462	12				80	73	77
3	1483	13	132	98	117			
4	1503	22				79	111	133
5	1518	8	142	140	109			
6	1428[1]	20				96	73	87

Table A.20: The carbon and nitrogen levels and settlement times for all parallels from all analysed samples from experiment Si-C-N-6.

Sample #	T [°C]	t_s [min]	C content [ppm mass]			N content [ppm mass]		
1	1424	4	87	125	87			
2	1441	13				72	58	58
3	1461	5	168	93	94			
4	1481	3				102	90	86
5	1501	12	105	98	103			
6	1521	5				124	138	124

[1]Extracted during cool-down.

A.5 Si–C–B-system

Table A.21: The carbon levels and settlement times for all parallels from all analysed samples from experiment Si-C-B-1.

Sample #	T [°C]	t_s [min]	C content [ppm mass]					B content mass%
1	1426	4	91	97	91	95		0.25
2	1426	10	457	91	218			0.25
3	1426	15	388	106	146			0.25
4	1453	2	88	446	99			0.25
5	1455	6	86	84	416			0.25
6	1455	10	83	95	88			0.25
7	1474	4	85	125	157	103	123	0.25
8	1475	11	158	141	143			0.25
9	1474	16	141	142				0.25
10	1494	2	117	131	153	264		0.25
11	1495	9	135	131				0.25
12	1498	1	132	132				0.25
13	1512	2	132	138	148			0.25
14	1513	5	151	136	149			0.25
15	1514	15	138	306	145	188		0.25
16	1514	22	146	119	163	118		0.25
17	1532	3	154	149	166			0.25
18	1533	11	158	131				0.25
19	1533	18	149	169	143			0.25
20	1533	24	157	209	138			0.25
21	1542	4	235	171	184	167		0.25

Table A.22: The carbon levels and settlement times for all parallels from all analysed samples from experiment Si-C-B-2.

Sample #	T [°C]	t_s [min]	C content [ppm mass]				B content mass%
1	1422	16	77	73	74	76	0.50
2	1422	40	81	193	79		0.50
3	1438	6	82	79	80		0.50
4	1438	15	77	89	90	85	0.50
5	1458	13	90	92	90		0.50
6	1458	16	93	88	94		0.50
7	1478	5	98	103	115		0.50
8	1478	8	108	106	109	113	0.50
9	1498	5	144	137	127		0.50
10	1498	8	138	117	112		0.50
11	1518	8	151	144			0.50
12	1518	12	127	133	126	158	0.50

Table A.23: The carbon levels and settlement times for all parallels from all analysed samples from experiment Si-C-B-3.

Sample #	T [°C]	t_s [min]	C content [ppm mass]				B content mass%
1	1422	6	95	92	130		1.00
2	1422	40	120	88	95	99	1.00
3	1430	5	99	106	105		1.00
4	1441	41	96	105	94		1.00
5	1460	5	124	125	125		1.00
6	1460	22	118	111	120		1.00
7	1479	5	127	135	143		1.00
8	1479	8	142	151	149	151	1.00
9	1499	6	150	129	157		1.00
10	1499	12	154	152	162		1.00
11	1518	5	179	184	177		1.00
12	1518	14	179	188	197		1.00

Table A.24: The carbon levels and settlement times for all parallels from all analysed samples from experiment Si-C-B-4.

Sample #	T [°C]	t_s [min]	C content [ppm mass]				B content mass%
1	1433	2	108	113			1.50
2	1433	16	119	106			1.50
3	1434	21	113	122			1.50
4	1445	1	133	138			1.50
5	1448	7	142	139			1.50
6	1448	16	133	148			1.50
7	1462	4	144	157	148		1.50
8	1462	6	132	150			1.50
9	1476	2	109	129	138		1.50
10	1477	12	136	114	153		1.50
11	1477	18	147	175	174	149	1.50
12	1491	8	173	168	156		1.50
13	1491	15	165	159	171		1.50
14	1491	23	160	157	205		1.50
15	1505	1	185				1.50

Table A.25: The carbon levels and settlement times for all parallels from all analysed samples from experiment Si-C-B-5.

Sample #	T [°C]	t_s [min]	C content [ppm mass]				B content mass%
1	1436	1	136	128	147		2.00
2	1436	20	124	138			2.00
3	1449	11	129	136			2.00
4	1464	9	136	141	150	152	2.00
5	1477	1	164	174	168		2.00
6	1492	1	163	180			2.00
7	1507	4	197	193	209		2.00

Table A.26: The carbon levels and settlement times for all parallels from all analysed samples from experiment Si-C-B-6.

Sample #	T [°C]	t_s [min]	C content [ppm mass]			B content mass%
1	1436	19	129	82	103	0.25
2	1444	10	88	86	85	0.25
3	1465	6	91	90	133	0.25
4	1485	16	113	109	128	0.25
5	1505	10	128	147	104	0.25
6	1524	9	183	131	145	0.25

Table A.27: The carbon levels and settlement times for all parallels from all analysed samples from experiment Si-C-B-7.

Sample #	T [°C]	t_s [min]	C content [ppm mass]			B content mass%
1	1435	12	103	94	73	0.5
2	1446	5	108	95	86	0.5
3	1466	12	108	101	101	0.5
4	1485	5	100	125	139	0.5
5	1506	13	133	136	136	0.5
6	1525	6	177	160	152	0.5

A.6 Si–B–N-system

Table A.28: The nitrogen levels and settlement times for all parallels from all analysed samples from experiment Si-N-B-1.

Sample #	T [°C]	t_s [min]	N content [ppm mass]			B content mass%
1	1432	5	39	45	30	0.1
2	1432	9	38	38	37	0.1
3	1446	5	43	47	48	0.1
4	1468	15	66	45	54	0.1
5	1488	17	63	67	60	0.1
6	1507	10	82	84	76	0.1
7	1527	24	106	95		0.1
8	1528	28	92	107	111	0.1

Table A.29: The nitrogen levels and settlement times for all parallels from all analysed samples from experiment Si-N-B-2.

Sample #	T [°C]	t_s [min]	N content [ppm mass]			B content mass%
1	1434	17	14	12	16	1.5
2	1444	6	14	26	16	1.5
3	1444	11	16	8	12	1.5
4	1464	17	10	9	12	1.5
5	1483	6	12	8	11	1.5
6	1503	5	11	11		1.5
7	1522	5	12	9	10	1.5
8	1522	18	15	41	15	1.5